# Measurement of Acoustic Attenuation in South Pole Ice with a Retrievable Transmitter

DISSERTATION

zur Erlangung des akademischen Grades
doctor rerum naturalium
(Dr. rer. nat.)
im Fach Physik

eingereicht an der
Mathematisch-Naturwissenschaftlichen
Fakultät I
Humboldt-Universität zu Berlin

von
Frau Dipl.-Phys. Delia Tosi
geboren am 22.05.1981 in Verona, Italien

Präsident der Humboldt-Universität zu Berlin:
Prof. Dr. Dr. h.c. Christoph Markschies

Dekan der Mathematisch-Naturwissenschaftlichen
Fakultät I:
Prof. Dr. Lutz-Helmut Schön

Gutachter:

1. Prof. Dr. Hermann Kolanoski
2. Prof. Dr. Allan Hallgren
3. Prof. Dr. P. Buford Price

eingereicht am: 29 Oktober 2009
Tag der mündlichen Prüfung: 15 Februar 2010

**Abstract**

The neutrino flux generated by the interaction of high energy cosmic rays with the cosmic microwave background is predicted to produce about 0.1 event per $km^3$ per year. The detection of a sufficient number of events in a few years requires to instrument a volume of at least 100 $km^3$. The biggest detectors nowadays in construction, covering a volume of about 1 $km^3$, utilize optical sensors to detect the light produced by neutrino interactions; to extend this instrumentation method by the two necessary orders of magnitude is cost-prohibitive. An alternative is to use the radio or the acoustic signal generated by the neutrino-induced particle cascade, or even better, to use both of them in a hybrid detector.

Ice is a promising medium since in principle all three signals can be detected simultaneously. The growing optical experiment IceCube, located at the geographic South Pole, could be complemented with radio and acoustic sensors. A pre-requisite to do so is to measure the acoustic properties of South Pole ice. The *South Pole Acoustic Test Setup* (SPATS) has been designed to measure background noise, sound speed profile, transient events rate and acoustic attenuation length at that location. The system is comprised of four strings of acoustic sensors and transmitters which are installed at depths between 80 and 500 m. In addition, a retrievable transmitter (called *pinger*) has been developed and used in several water-filled holes.

After almost three years of operation, good progress has been achieved for all the goals. In particular, the attenuation length, one of the most important parameters for determining neutrino detection feasibility, and for which only theoretical estimates were available previously, has now been measured *in situ* with high confidence to be $312^{+68}_{-47}$ m. In this work the hardware developed and the analysis performed to achieve this measurement are presented together with the final result.

**Keywords:**
Neutrino astronomy, GZK effect, South Pole, Acoustics, Acoustic attenuation

**Zusammenfassung**

Der Neutrinofluss der durch die Wechselwirkung hochenergetischer kosmischer Strahlung mit dem kosmischen Mikrowellenhintergrund entsteht, produziert etwa 0.1 Ereignis/km$^3$ und Jahr. Um in wenigen Jahren eine ausreichende Anzahl an Ereignissen zu selektieren, muss ein Volumen von mindestens 100 km$^3$ instrumentiert werden. Die größten aktuell im Bau befindlichen Detektoren, mit einem Volumen bis zu 1 km$^3$, benutzen optische Sensoren um das Licht zu detektieren, das durch die Neutrinowechselwirkungen produziert wird. Aus Kostengründen ist es nicht möglich mit dieser Technologie 100 mal größere Detektoren zu bauen. Eine Alternative besteht darin, die durch den bei der Neutrinowechselwirkung entstehenden Teilchenschauer hervorgerufenen akustischen Signale und Radiosignale oder deren Kombination nachzuweisen.

Eis ist dafür ein vielversprechenden Medium, weil es die Möglichkeit bietet alle drei Signal (optisch, akustisch, radio) nachzuweisen. Eine Grundvoraussetzung für die Entwicklung eines solchen Detektors ist die Bestimmung der akustischen Eigenschaften des Eises am Südpol. Das *South Pole Acoustic Test Setup* (SPATS) wurde mit dem Ziel gebaut, den Rauschuntergrund, die tiefenabhängige Schallgeschwindigkeit, die Untergrundereignisrate und die Schall-Abklinglänge zu messen. Der Detektor besteht aus 4 Trossen, bestückt mit akustischen Sensoren und Transmittern, die in Tiefen zwischen 80 und 500 m im Eis am Südpol installiert wurden. Zusätzlich wurde ein Transmitter (*Pinger*) entwickelt, der in mehreren wassergefüllten Bohrlöchern zum Einsatz kam.

Nach drei Jahren ist guter Fortschritt bei der Messung aller beschrieben Grössen erzielt worden. Insbesondere haben es der kombinierte Einsatz von SPATS und des Pingers ermöglicht, die erste *in situ* Messung der Abklinglänge zu $312^{+68}_{-47}$ m vorzunehmen. In dieser Arbeit werden die Entwicklung der Hardware, die Analyse und die Resultate dieser Messung vorgestellt.

**Schlagwörter:**
Neutrinoastronomie, GZK-Effekt, Südpol, Akustik, Schalldämpfung

# Widmung

The first time I heard the word "neutrino" I was about 12 years old. At that time my father had already told me a lot of stories about the immensity of the universe and the huge number of stars, galaxies and clusters of galaxies which surround our planet. My perception of this was nevertheless a bit distorted by my young age, and one of my biggest worries was that the Sun could blow up during my lifetime. A bit later, I was fascinated by the physics that one studies in books, which explains how nature works: that there are six leptons and six quarks, and all is combined perfectly to make what we can see, or what we can at least prove exists.

The same fascination was driving me when I decided to follow an alternative route after my engineering studies at the Politecnico of Milan. At that time I could not imagine that physics is much more complicated than what I believed. And I could not imagine that I would have entered a side of physics completely unknown to me: the side where the answers are not written in textbooks, the side of models, predictions, and such uncertainties, that no rational man would ever bet on making any meaningful measurement. But, as I learned during my Ph. D., sometimes a good team with some luck manages to add a small sand grain to the huge castle of knowledge which humans have been building forever. And amazingly, all the efforts done at that point make sense.

In the meantime, I keep being fascinated by this world: most things still hide a mystery, and it is so incredible that there are scientists working to find out things that common people do not even imagine (or understand). I cannot deny that I was myself amazed when I was told that there are people putting photo-multipliers down in the ice, over a 1 $km^3$ volume, to see neutrinos' light. And I still feel surprised when I hear that some others look at the moon waiting for a radio signal produced by the interaction of one of these tiny non-charged particles, or that there are kilotons of instrumented material sitting underground in some place waiting for the Earth to hit some dark matter particles. Or again, that someone is planning to put a telescope in space looking at the atmosphere from above to see the showers initiated by cosmic particles. I must admit that I still feel pretty much like Alice in Wonderland.

And now I am already at the end of this unlikely Ph. D., which I started by making a bet on myself: I was very naïvely following the dream I had since I was a kid, the dream to study, and maybe find, neutrinos. Of course life is a

composition of multiple choices, and none of them is right or wrong. But I believe that sometimes, to get the best, one has to take risks. And I am happy I took this one: I have met the best "crazy" people ever, I have learned a lot, and I have collected some dream-like experiences which I will bring with me in all the rest of my life, among which is the unforgettable minute in which I landed at the South Pole.

This is why I dedicate my thesis to all the people who made these three years so special, and among them, especially to all the people who take a chance.

# Contents

# List of Figures

# List of Tables

# Chapter 1

# Introduction

Every day the Earth is hit by charged particles whose energy is not reproducible in the laboratory. Where and how these cosmic rays are generated is one of the most exciting puzzles that astrophysics is trying to solve. It is still not clear how many of them are protons or nuclei and how the composition changes as a function of the energy. Several models have been developed to explain the possible acceleration mechanisms, and several experiments are trying to correlate the origin of these particles with known celestial objects.To date no convincing explanation seems to be able to build a coherent scientific frame.

One problem is that the flux is extremely low and steeply decreasing with the energy: the average rate per $km^2$ is 1 event per year at $10^{18}$ eV and drops to 1 event per century at $10^{20}$ eV [1]. To detect such a low flux requires a detector with a huge acceptance. Recently the measurement of 58 events above 55 EeV in 34 months of observation (with a total integrated exposure of 17040 $km^2$ sr yr ($\pm 3\%$)) has been published by the Pierre Auger Observatory [2].

Cosmic rays with an energy above $4 \cdot 10^{19}$ eV are predicted to interact with the cosmic microwave background radiation [1][3]; at this energy a sharp cut-off of the cosmic ray spectrum is therefore expected. The interaction would lead to the production of neutrinos at distances of less than about 50 Mpc from the source of the charged particles, and would therefore guarantee a flux of neutrinos coming to us straight from the powerful cosmic accelerators.

To detect neutrinos coming from these sources would not only improve our understanding nature and interaction of the ultra-high energy (UHE) cosmic rays, but would also imply enormous improvements in our physics knowledge. Neutrino astronomy would make possible the identification of the cosmic accelerators thanks to the transparency of the universe to these messengers, which can travel unaffected by magnetic fields and dust. In addition, the measurement of the flux would allow us to test particle physics extrapolations at energies which are not reachable in Earth-located accelerators. The center of mass energy for the Large Hadron Collider will not go beyond $14 \cdot 10^{12}$ eV which corresponds to a proton energy of $10^{17}$ eV, orders of magnitude lower than the energy of UHE cosmic rays. Moreover, non-standard models which predict different neutrino fluxes from the decay of

heavy exotic particles [4] could be tested and perhaps ruled out.

The detection of these neutrinos is challenging since their expected flux rate is extremely low: so low that, to get a few tens of events in a few years, a huge volume, on the order of 100 $km^3$, needs to be instrumented. However, the interaction probability increases at high energy: this plays in favor of detection but decreases the observable portion of the sky, since those UHE neutrinos passing through the Earth are absorbed. When a UHE neutrino interacts with the target material, it produces a shower of secondary particles, called a cascade, and a lepton, which can be charged (charged-current interactions) or neutral (neutral-current interactions) [5].

Nowadays, the largest neutrino telescopes built or in construction (Baikal, AMANDA, IceCube, ANTARES) utilize as detection channel the light emitted by the charged lepton and by the cascade produced in the interaction. These detectors have been optimized for discovery in the energy range between $10^{12}$ and $10^{17}$ eV, and cover a volume of about 1 $km^3$ [6]. To increase this volume by the necessary two orders of magnitude is prohibitive in cost; the use of alternative techniques has been therefore of increasing interest.

In principle, it is possible to collect complementary information from the cascade, using the radio and acoustic detection methods. Radio antennas can indeed detect the coherent superposition of the electric field induced by the excess of negative charge in the cascade [7], while acoustic sensors can sense the pressure wave generated by the energy deposition which heats up the target material in the shower volume [8]. Using the radio or the acoustic methods would make possible the deployment of cheaper instrumentation over larger distances, thanks to an attenuation length of the signal generally longer than that of light. The radio technique has been successfully used to set the lowest limit at UHE energies by experiments like RICE [9] [10] and ANITA [11]. The acoustic method, still at an earlier stage of development, is currently under study in several smaller experiments in various target media.

An even more powerful approach in the design of a 100 $km^3$ detector would be to combine both optical and radio and acoustic sensors. To be able to record at least two of the three signals simultaneously would indeed improve the capability of reconstructing energy and direction of the neutrino detected, and would allow for an efficient background rejection.

A 100 $km^3$ detector combining optical strings with radio and acoustic strings was simulated in 2005 and estimated the detection of about 20 GZK neutrinos per year, 40% of which as hybrid events detected by more than one technique [12]. Since no measurement of the acoustic properties of South Pole ice had been done before, a predicted acoustic ice model was included in the simulation: in particular, assumptions were made regarding noise level and attenuation length [12].

The *South Pole Acoustic Test Setup* (SPATS), an array of acoustic sensors and transmitters, was developed in order to study the feasibility of acoustic neutrino detection at the South Pole, *i.e.* to test the validity of the ice properties assumed

for the simulation. The main goals of the experiment were to measure *in situ* the noise level, the transients rate, the sound speed depth profile and the attenuation length.

I joined the SPATS project at the end of July 2006, about six months before the deployment of the system at the South Pole. At that time the whole instrumentation was located in DESY, and I had the privilege to work on the final preparation of the system, before the deployment of the first three strings which was successfully done in January 2007. In the following months, the analysis of the first data from SPATS made clear that understanding the performance of our system would have required quite some time, since the acoustic signals produced by the transmitters and recorded by the sensors were inexplicably lower than expected.

During the 2007 IceCube spring meeting in Madison, the Acoustic Neutrino Detection Working Group was formed, and the idea of a retrievable *pinger* started developing into a real project, together with the one to install a new improved string at a deeper level, with better transmitters and better sensors. I actively participated in the construction of the pinger and of the sensors and transmitters of the new string. The pinger idea was originally conceived by Allan Hallgren, and it was designed and built in DESY by Karl Heinz Sulanke, Reiner Heller, Rolf Nahnhauer and myself in the following months as a long-range portable and retrievable transmitter. The goal was to have a unique acoustic source, featuring the most isotropic angular behavior possible, to be deployed in multiple water-filled holes at different distances from the SPATS array. In this way each sensor could have been used independently for an attenuation length analysis, avoiding the necessity to combine multiple frozen-in sensors and transmitters and therefore reducing the uncertainties. Moreover, a calibration of the sensors deployed in the ice could have been attempted.

Between December 2007 and January 2008 the new string was deployed, and the pinger was run in six IceCube holes. After what we believed had been a very successful season, the analysis of the data collected showed that our pinger was far from being perfect for attenuation analysis, since the waveforms recorded by the same sensor for different distances of the pinger were completely different in shape, and not simply attenuated. A deep brainstorming led us to identify the major problem to be that the pinger was free to move and swing in the hole during operation: this affected the transmission of the waveform into the ice, resulting in an uncontrolled waveform shape, with the additional appearance of shear waves. In addition, the geometry of the holes made it necessary to combine data over a large azimuthal angle. The data collected were used anyway: the appearance of shear waves itself indeed made it possible to achieve the most precise sound speed measurement *in situ* for both pressure and shear waves in glacial ice down to 500 m depth [13].

In the following summer the pinger was improved by the addition of centralizers capable of centering the stage in the hole, in order to get an emitted pulse of constant amplitude. In addition, we increased the repetition rate at which the

pinger pulsed, thanks to the help of Leif Gustaffson from Uppsala. We also worked to change the data acquisition system in order to have three channels of the same sensor recording simultaneously each pulse, and all the sensors at the same depth recording together. In the same months, we also did some work on the SPATS DAQ to turn the system into a real detector recording events in triggered mode.

In the following season (austral summer 2008-2009) the new pinger was deployed in four IceCube holes. The holes were favorably aligned in direction of the SPATS array within 13 degrees, so that for each sensor the sensitivity variation on the azimuthal plane was minimized. The pinger was stopped between 190 m and 500 m depth at levels instrumented with SPATS sensors; at each depth the pinger was stopped twice (while lowering and rising the device) to check the stability of the pulse shape and achieve redundancy in the data. For each sensor we selected the data recorded when the pinger was at the same depth as the sensor; this minimized the polar variation of the sensor sensitivity. For every sensor the waveforms turned out to be very stable and consistent in shape from hole to hole, and each of the 49 channels could be used for an independent attenuation measurement.

In parallel with the work on the field, research has been conducted in the laboratory in order to resolve another issue. A fundamental problem concerning any experiment installed in South Pole ice is the difficulty of calibrating the sensors in similar conditions to the ones after installation, *i.e.* at high pressure, low temperature, and in ice contact. One possibility is to test the sensors in one condition at a time, and make assumptions on the combination outcome to estimate the sensitivity variation after installation. Laboratory tests have been performed at low temperature and high pressure and are part of the work presented here.

This thesis summarizes what I have done in the past three years within the study of feasibility of acoustic neutrino detection at the South Pole. In addition a parallel research on the acoustic properties of permafrost has been carried out, in the search of a material alternative to ice for a neutrino detector in the northern hemisphere. This work is not presented here and can be found in [14].

The thesis develops conceptually through four parts:

- Introduction: in the first section the motivation of the present research is given. This includes a summary regarding the physics of UHE neutrinos (Chapter 2) and an introduction to the neutrino hybrid detection concept (Chapter 3).

- Experimental activity at the South Pole: in this section the experiment realized at the South Pole is described. Chapter 4 illustrates the hardware used, including both the instrumentation permanently deployed in ice (the *South Pole Acoustic Test Setup*) and the acoustic retrievable transmitter (the *pinger*). Chapter 5 gives a comprehensive discussion about the data quality for the two pinger seasons and the analysis performed to determine the attenuation length. The result has been confirmed by independent analyses on different datasets, which are briefly presented.

- Experimental activity in the laboratory: in this section the previously cited calibration tests at high pressure and low temperature will be described (Chapter 6).
- Summary and outlook are given in Chapter 7.

# Chapter 2

# Physics of ultra-high energy neutrinos

## 2.1 Photon astronomy

Ever since humans have been observing the sky, they have constantly improved their techniques in order to acquire as much information as possible about the universe. For thousands of years visible light was the only means used, first by the eyes of the ancient astronomers in the early cultures and later by more sophisticated telescopes, developing the so called classical astronomy.

From the end of the $19^{\text{th}}$ century on, an enormous amount of discoveries opened new horizons to the field of observation. Spectroscopy of sunlight was used to infer the composition of the Sun, and the use of photography made possible the discovery of faint objects. Later the discovery of X-rays and radio waves suggested the existence of different bandwidths of radiation, which could be used to get more information about the universe. Radio astronomy developed quickly: the first extraterrestrial radio emission was measured in 1933 [15], followed in 1937 by the construction of the first radio telescope [16]. X-ray astronomy became possible from the mid fifties with the launch of balloons, rockets and satellites to observe X-rays before they are absorbed by the atmosphere [17]. Nowadays the high energy region is extended up to hundreds of GeV by space telescopes (such as *Fermi* [18]), and up to tens of TeV by arrays of Cherenkov telescopes (such as *H.E.S.S.* and *MAGIC*) and the water-pool detector *Milagro*. In the future, it will be extended up to hundreds of TeV by *AGIS* or *CTA*, and *HAWC* [19].

However, the portion of the universe which can be observed with photons is, at high energy, restricted. The propagation of UHE photons is indeed affected by interactions with the cosmic photon background which limit the largest distances that can be searched. The main interaction process is absorption by positron-electron production:

$$\gamma + \gamma_{bg} \rightarrow e^+ + e^-. \tag{2.1}$$

This happens above the threshold energy $E_\gamma^{th}$:

$$E_\gamma^{th} = \frac{m_e^2 c^4}{\epsilon} \simeq 2.6 \cdot 10^{11} \left(\frac{\epsilon}{\text{eV}}\right)^{-1} \text{ eV} \tag{2.2}$$

where $\epsilon$ is the energy of the background photon, $m_e$ is the electron mass and $c$ is the speed of light. The interaction length of a photon is determined both by the energy dependent cross section $\sigma_{\gamma\gamma}(E_\gamma)$ and by the density of background photons $n_{\gamma bg}$:

$$L_\gamma = \frac{1}{n_{\gamma bg}\sigma_{\gamma\gamma}(E_\gamma)} \tag{2.3}$$

In this calculation it is necessary to take into account both the density of the background photons and their energy. It turns out that the limit is set by the photons of the infrared background for energies up to $10^{14}$ eV, by the cosmic microwave background between $10^{14}$ eV and $10^{19}$ eV, and by the radio background above $10^{18}$ eV [20]. The variation of $L_\gamma$ as a function of the energy can be seen in Figure 2.1. $L_\gamma$ is about 100 Mpc for 10 TeV photons, and decreases for increasing photon energy in such a way that 1 PeV photons can travel only a few tens of kpc. At higher energies $L_\gamma$ increases again; however, no photons at these energies have been observed.

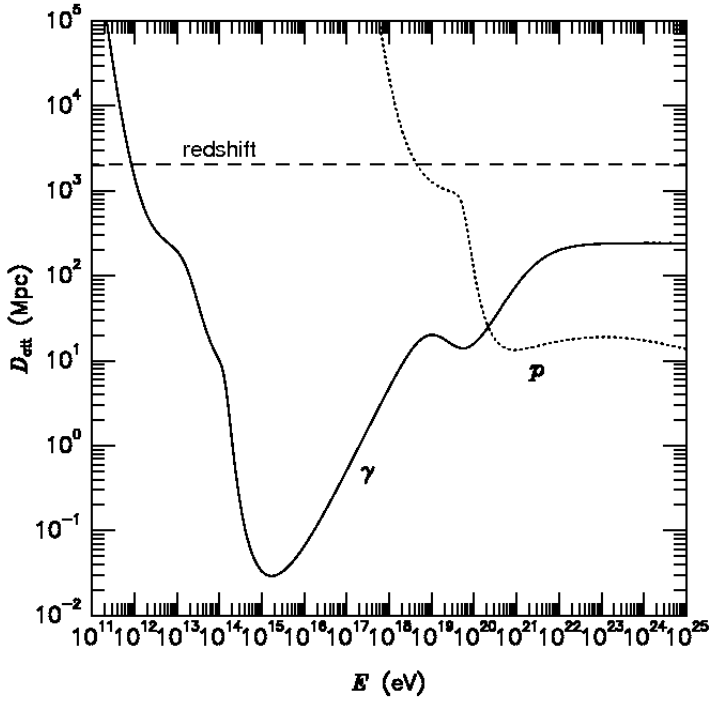


Figure 2.1: The attenuation length of photons, compared to the proton attenuation length. The dashed line labeled *redshift* indicates the size of the universe [21].

## 2.2 Proton astronomy

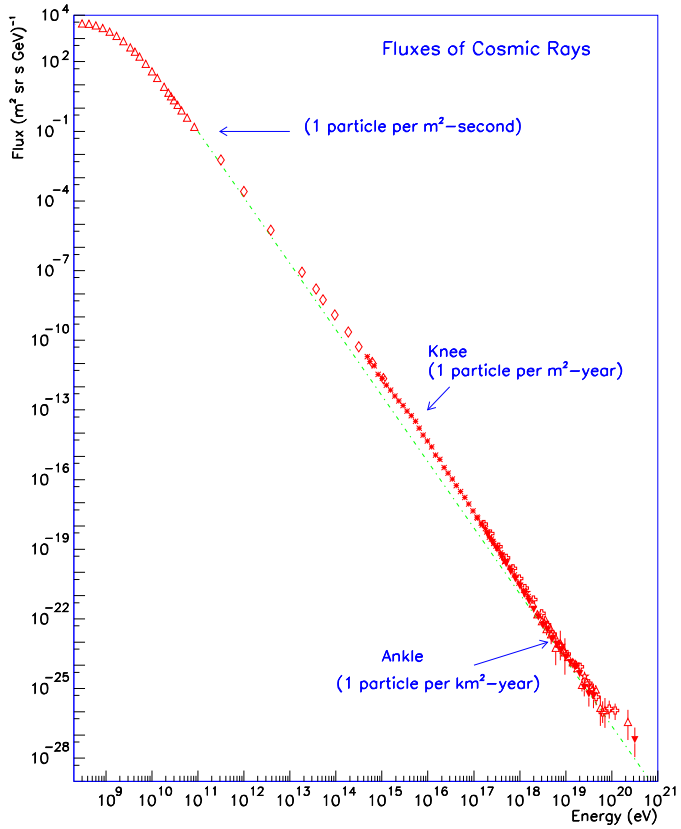


Figure 2.2: Cosmic ray spectrum observed by several experiments(from [1]).

At the beginning of the last century an information source different from photons was discovered by Victor Hess as penetrating radiation entering the atmosphere from above [22]. The radiation was found to be made of charged particles, thereafter called cosmic rays. These particles have been studied extensively during the last 100 years and their spectrum, spanning over 32 orders of magnitude in amplitude, has been measured over 12 orders of magnitude in energy. The measured flux, shown in Figure 2.2, exhibits several features which are not covered here; an exhaustive description is provided in [1] and [23].

Unfortunately, due to their charge, the cosmic rays are deflected in the galactic or (less strong) extra-galactic magnetic fields. The trajectory of a particle with charge $ze$ traveling in a magnetic field $B$ gets a curvature whose radius $r$ increases with the particle energy $pc$ and decreases with the strength of the field; the curvature depends also on the angle $\theta$ between particle and field direction, reaching a maximum if these are orthogonal and becoming zero if they are parallel. The

radius of curvature $r$ is defined as:

$$r[\mathrm{m}] \;=\; \frac{pc}{ze}\frac{\sin\theta}{Bc}. \tag{2.4}$$

Due to this effect, the direction of the charged particles impinging on Earth does not point back to the particle sources. Thus, even if it is reconstructed, no information can be gained regarding their origin. This does not hold in the very high energy range: particles whose trajectories have a radius of curvature larger than the galactic disk diameter ($r_g \sim 30$ kpc) will appear as traveling in a "quasi-straight" direction in our galaxy and will point back to their source. A useful parameter is the *rigidity* $R$, defined as the ratio between energy $pc$ and charge $ze$ of the particle:

$$R[\mathrm{V}] \;=\; \frac{pc}{ze}. \tag{2.5}$$

Particles with the same rigidity crossing a magnetic field with the same direction will be deviated with the same radius of curvature. Given the galactic disk diameter $r_g$, the lower limit of rigidity $R_{min}$ above which astronomy can be done using charged particles is determined, for a particle of charge $ze$, by the magnetic field ($B \approx 10^{-10}$ T) as:

$$\begin{aligned} r &> r_g \\ R_{min} &= r_g Bc = 10^{19}\ \mathrm{V}. \end{aligned} \tag{2.6}$$

where the case of orthogonality between particle trajectory and magnetic field is assumed ($\sin\theta = 1$). The intergalactic magnetic field is much less intense than the galactic one and it is chaotic, therefore only the value of the galactic field is taken into account [21]. To calculate the angular deviation for these particles is quite difficult, since the galactic magnetic field experienced by a charged particle traveling across the galaxy strongly depends on the direction of the particle. A value of 3 degrees is assumed to be a reasonable rough estimate [24]. The threshold value of rigidity calculated in equation 2.6 corresponds to a minimum energy of $10^{19}$ eV for a proton, and therefore limits proton astronomy to $E_p > 10^{19}$ eV. The existence of such high energy cosmic rays was proved by the Volcano Ranch experiment in 1963 [25].

Just above this energy threshold for proton astronomy another effect is predicted to happen, the so called GZK (Greisen, Zatsepin and Kuzmin) cut-off [3]. The flux of protons is expected to decrease due to interaction with the cosmic microwave background photons. The interaction produces photons and pions, and becomes resonant when a $\Delta^+$ is produced:

$$\begin{aligned} p + \gamma_{CMB} \rightarrow \Delta^+ \rightarrow \;& p + \pi^0 \\ & n + \pi^+. \end{aligned} \tag{2.7}$$

The energy threshold for the process is:

$$E_p^{th,CMB} = \frac{m_\pi c^4 (M_N + m_\pi/2)}{\epsilon_{CMB}} \approx 4 \cdot 10^{19} \text{ eV} \tag{2.8}$$

where $M_N$ is the mass of the nucleon, $m_\pi$ is the mass of the pion and $\epsilon_{CMB}$ is the energy of the cosmic microwave background photons (about $10^{-3}$ eV).

In addition, pair production can happen:

$$p + \gamma_{CMB} \rightarrow p + e^+ + e^- \tag{2.9}$$

and it is dominant at lower energies due to the lower energy threshold:

$$E_p^{th,pp} = \frac{M_e c^4 (m_N + m_e)}{\epsilon_{CMB}} \approx 5 \cdot 10^{17} \text{ eV}. \tag{2.10}$$

A heavier nucleus of energy $E$ and mass number $A$ can be treated as carrying an energy $E/A$ per nucleon, since in first approximation the binding energy can be neglected. The energy thresholds for both interactions scale therefore proportionally to $A$:

$$E_A^{th} = A \cdot E_p^{th}. \tag{2.11}$$

Pair production and photo-pion production combine to limit the interaction length of protons to:

$$L_p = \frac{1}{n_{\gamma,CMB}\ \sigma_{p\gamma}} \tag{2.12}$$

where $\sigma_{p\gamma}$ is the cross section of the interaction process between a proton and a photon.

The pair production process dominates at energies between $E_p^{th,pp}$ and $E_p^{th,CMB}$ and photo-pion production dominates at energies above $E_p^{th,CMB}$. Figure 2.1 illustrates the interaction length of protons compared to that of photons and with the actual size of the visible universe (indicated by the label *redshift*). For a proton of energy $E_p = 10^{20}$ eV, $L_p \sim 100$ Mpc; for $E_p > 10^{20}$ eV $L_p$ scales down to about 10 Mpc. As a result charged particles of about $10^{20}$ eV could come only from objects nearer than 100 Mpc; if produced at larger distances they would lose energy on their way.

Looking at Figure 2.1 it appears that the portion of the universe which is observable by detection of high energy photons and protons is smaller than its actual size; beyond the limits defined by the attenuation mechanisms, the universe is thus opaque to the passage of protons and photons.

The experimental verification of the predicted GZK cut-off in the charged cosmic ray spectrum has been debated for a long time. Two experiments indeed gave contradictory results:

- the *High Resolution Fly's Eye* (HiRes), a stereo fluorescent experiment with two observational sites in the Utah desert, observed a steepening of the spectrum above $10^{19.8}$ eV consistent with GZK cut-off [26].

- the *Akeno Giant Air Shower Array* (AGASA) experiment, consisting of 111 surface detectors and 27 underground muon detectors spread over an area of 100 km$^2$ in Japan, detected a significant excess of events above $10^{20}$ eV [27].

Recently, data collected from the Pierre Auger Observatory, consisting of an array of water Cherenkov detectors covering an area of over 3000 km$^2$ overseen by 4 atmospheric fluorescence detectors, show a steepening of the flux at 6 $\sigma$ level above $4 \cdot 10^{19}$ eV, which is exactly the threshold expected for the effect [28]. On the other hand, several aspects remain still unclear, such as the spectrum composition and the correlation of the extremely-high-energy cosmic rays detected with potentially known accelerator objects; more statistics, to come with longer data taking, will probably help in clarifying the situation.

## 2.3 Neutrino astronomy

In addition to protons and photons, another possible source of information about processes in the universe is neutrinos. Neutrinos are the only known particles which interact only weakly with matter. This makes them an ideal messenger of information even from the deep interior of massive objects like the sun. Indeed solar neutrinos have been observed already, as well as the ones from a supernova explosion in the closest galaxy [29].

A source of neutrinos at very high energies is connected with the GZK cut-off predicted for charged cosmic rays described in the previous section. These neutrinos were predicted for the first time in 1969 by Berezinsky and Zatsepin [30]. Looking at equation 2.7 one can see that both branches of the process produce pions. The pions decay with production of neutrinos and photons:

$$\begin{aligned} \pi^0 &\rightarrow \gamma + \gamma \\ \pi^+ \rightarrow \mu^+ + \nu_\mu &\rightarrow e^+ + \nu_e + \bar{\nu_\mu} + \nu_\mu \end{aligned} \tag{2.13}$$

Figure 2.3 illustrates the whole interaction mechanism described by equation 2.7 and 2.13.

In addition to the neutrino produced by pion decay, other neutrinos at lower energy are produced by the neutron $\beta$-decay:

$$n \rightarrow p + e^- + \bar{\nu}_e \tag{2.14}$$

The neutron decay rate in the laboratory frame

$$\Gamma_N = \frac{m_N\, c^2}{\tau_n E_N} \tag{2.15}$$

depends on the mass $m_N$ and the energy $E_N$ of the neutrons and on the lifetime $\tau_n$, which is $\tau_n \approx 885.7 \pm 0.8$ s [31]. This translates into a range of propagation of:

$$R_N \approx \tau_n\, c \cdot \frac{E_N}{m_N\, c^2} \simeq 0.9 \left( \frac{E_N}{10^{20}\ \text{eV}} \right)\ \text{Mpc} \tag{2.16}$$

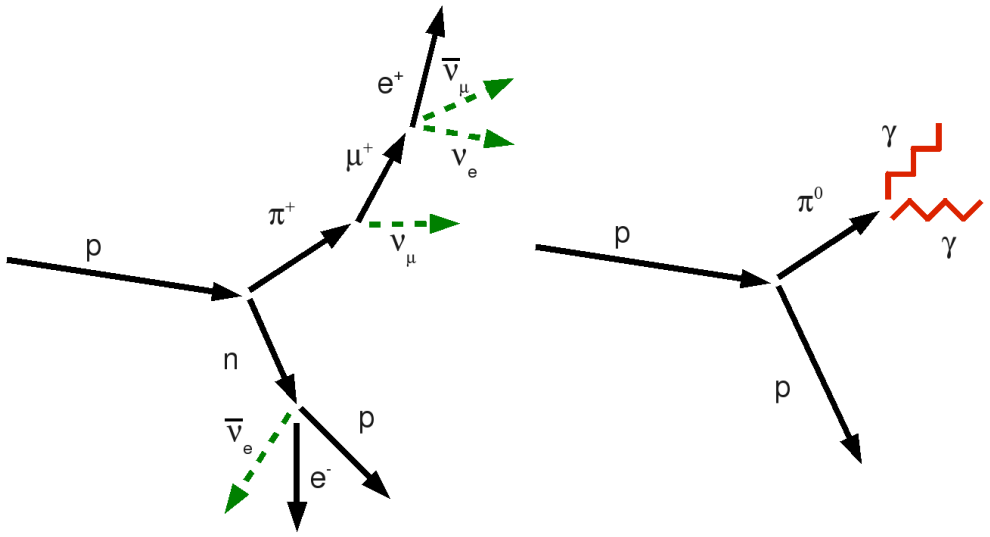


Figure 2.3: Photo-pion production mechanism.

so that basically all the UHE neutrons decay to protons within a few Mpc [1].

If the number of neutrinos is calculated integrating over all the energy range, the ratio between the sum of neutrinos and anti-neutrinos for each flavor at the origin is $\phi(\nu_e + \bar{\nu}_e) : \phi(\nu_\mu + \bar{\nu}_\mu) : \phi(\nu_\tau + \bar{\nu}_\tau) = 1 : 1 : 0$ (see equations 2.13 and 2.14). If only high energy neutrinos are considered, the ratio between flavors of neutrinos and anti-neutrinos is $1 : 2 : 0$ (equation 2.13); due to oscillation during propagation, upon arrival at Earth the ratio is expected to be $1 : 1 : 1$ as explained in [32] and [33]. The neutrino flux predicted as a function of the energy can be seen in Figure 2.4 for different proton propagation lengths as derived in the Engel-Seckel-Stanev (ESS) model [32].

Only a fraction of the primary proton energy is transferred to neutrinos [32], which is independent of the energy of the proton: in the interaction described by equation 2.7 the pion takes on average 20% of the energy of the primary proton. This energy is then equally distributed to the pion decay products, so that in the end $E_{\nu,e} \sim 0.05\ E_p$. This effect shifts the peak in the GZK neutrino spectrum to between $10^{17}$ and $10^{18}$ eV, a lower energy compared to the GZK cut-off energy.

In the ESS model the normalization of the flux is derived from the observed cosmic ray flux. Since neutrinos get a fixed percentage of the proton energy, the flux from a single emitting source follows the proton spectrum (see Figure 2.4):

$$\frac{dN}{dE} \propto E^{-\alpha} \exp(-E/E_c) \tag{2.17}$$

where $\alpha$ is the spectral index and $E_c$ is the energy cut-off. In the ESS flux calculation, the following assumptions are made:

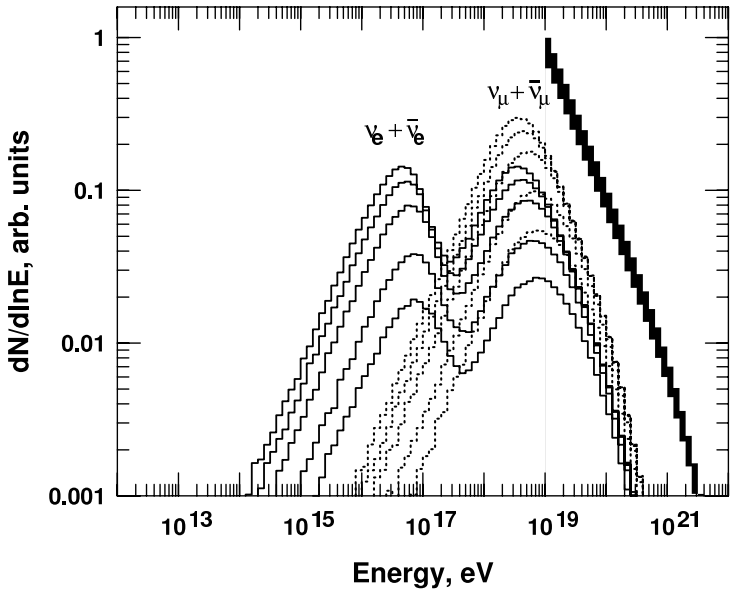


Figure 2.4: Neutrino flux predicted by the Engel-Seckel-Stanev model (from [32]). The different lines (from bottom up) show the flux produced by the propagation of protons over 10, 20, 50, 100, and 200 Mpc. The thick line shows the proton injection spectrum.

- A uniform distribution of sources is assumed, featured by a power law cosmic ray injection spectrum with $\alpha$ between 1.8 and 2.7 and a cut-off energy $E_c = 10^{21.5}$ eV.
- The energy scaling due to redshift is taken into account: if a neutrino is observed at present ($z = 0$) with energy $E_0$, the energy at the emission $E_z$, for a source at redshift $z$ is:

$$E_z = E_0(1+z). \tag{2.18}$$

- The expansion of the universe is inserted in the model as a factor reducing the density of the observable sources from $n_z$ to $n_0$, parametrized with a time-dependent power law:

$$\begin{aligned} n_z &= n_0(1+z)^m \qquad \text{for } z < z_{max} \\ n_z &= n_0(1+z_{max})^m \qquad \text{for } z \geq z_{max} \end{aligned} \tag{2.19}$$

  $m$ depends on the redshift $z$ since the universe acceleration changes with time, with the assumption of a precise cosmological evolution model for the cosmic ray sources. The parameter $z_{max}$ defines the limit redshift beyond which the contribution of sources of constant density is not significant; this contribution can be eventually damped by a falling exponential inserted as a multiplication factor in the density for $z > z_{max}$ [32].

The total GKZ neutrino flux is calculated folding the neutrino spectrum of all the sources with the assumptions made above. It must be noticed that many uncertainties enter in the calculation, such as cosmological parameters, normalization choice, assumed chemical composition of the primaries (protons or heavier nuclei) and a fixed neutrino energy yield; just recently the original computation for the ESS flux has been going under a review process [34].

The GZK flux expectation and the limits set from the most recent experiments are shown in Figure 2.5. The value of the flux at the peak value is $\Phi(E_\nu = 10^{17}\,\mathrm{eV}) \approx 1\,\mathrm{km}^{-2}\,\mathrm{yr}^{-1}\,\mathrm{sr}^{-1}$. The current global uncertainty, shaded in the Figure, is about one order of magnitude. The limits set by different experiments are shown: it is worth noticing that the experiments closer to the expected flux are those based on radio detection, in the Antarctic ice (RICE [10], ANITA-light, ANITA [11]) or in Greenland (FORTE) [35]. As it will be explained in the following chapters, the use of the radio signal allows for a higher exposure than other methods such as shower measurement (used by the Pierre Auger Observatory) and optical detection (used by AMANDA).

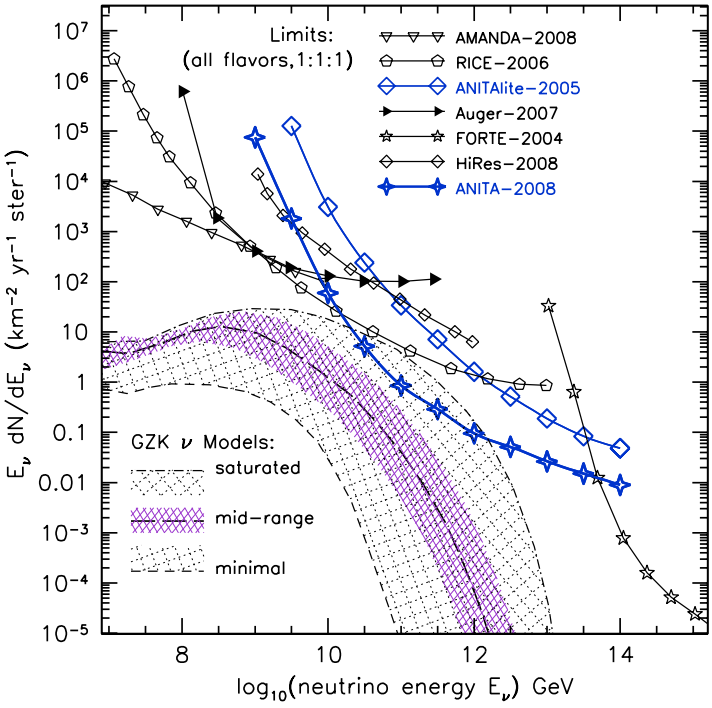


Figure 2.5: Neutrino flux expected from GZK cut-off and most recent limits set from different experiments (from [11]).

The GZK flux predicted by the Engel-Seckel-Stanev model belongs to the category of models called “bottom-up”, where a flux of neutrinos is expected to accompany the flux of UHE cosmic rays as a result of the interaction of accelerated

hadrons. In the GZK flux prediction, neutrinos are produced happens along the paths of cosmic rays. Other models, different from GZK, assume neutrinos being produced at the acceleration site (for example in AGNs), and calculate the expected neutrino flux making hypotheses on the sources features and distribution.

Two commonly quoted calculations are the ones done by Waxman and Bahcall in 1999 and by Mannheim, Protheroe and Rachen in 1998. These two models make some optimistic assumptions and simplifications both on the source distribution and emission spectrum and on the neutrino production. The outcome of the calculations are considered upper bounds to the neutrino flux produced in sources, a few times higher than the most probable one. The two limits are usually used as a conservative reference to be compared with detector sensitivities.

The Waxman-Bahcall limit uses a fixed value of $\alpha = 2$ for the cosmic ray spectrum (true above the ankle at about $2 \cdot 10^{18}$ eV, see Figure 2.2), and assumes (unrealistically) that all the energy from the primary proton is transferred to the neutrino. The sources are isotropically distributed and are all optically thin, so all the neutrons escape and decay to protons [36]. From the detected flux of cosmic rays, the number of protons and neutrinos at the source can be calculated; from this the number of expected neutrinos at Earth is obtained.

In the Mannheim-Protheroe-Rachen limit, the power law coefficient is estimated from fitting the cosmic ray flux between $10^{17.6} - 10^{20}$ eV, assuming that in this range of energy all the cosmic rays have extragalactic origin and are produced by the neutron decay (equation 2.14). Thick sources are included as a function of the redshift. This results in an enhancement of the neutrino limit compared to the one proposed by Waxman-Bahcall [37], since for these sources the number of protons and neutrinos produced at the source would be bigger than the one assumed from the measured cosmic ray flux.

In addition to the previously cited "bottom-up" models, there is also another category of models generally called "top-down": a neutrino flux is predicted from the decay of existing heavy exotic particles whose rest mass energy is converted into protons, photons and neutrinos. One of the most popular candidates is the topological defects model [38]: different kinds of defects and anti-defects, generated at the GUT scale (monopoles, for example) with mass on the order of $10^{15}$ GeV, would annihilate into leptons and quark pairs which would then produce neutrinos, protons and gamma rays above the GZK-cutoff energy.

Another popular model is the Z-burst [39]: background relic neutrinos are predicted by the standard model of evolution of the universe to have a temperature of 1.9 K and a density of 56 cm$^{-3}$. High energy neutrinos would interact with them and produce $Z$ bosons:

$$\nu + \bar{\nu} \rightarrow Z \tag{2.20}$$

at a resonant energy, for $m_\nu \gg k_B T$, of:

$$E_{res} = \frac{m_Z^2 c^4}{2 m_\nu}. \tag{2.21}$$

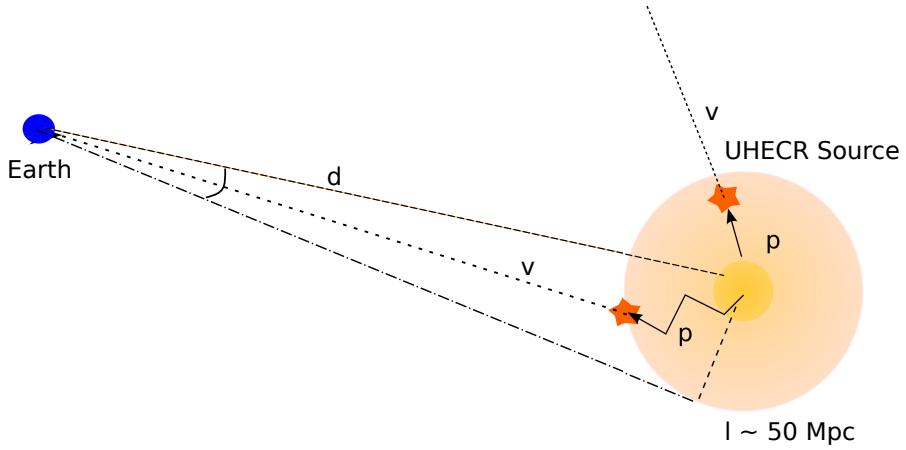


Figure 2.6: Neutrino pointing resolution: neutrinos can point back to their sources with a precision of less than 3 degrees for a source at a distance of about 1 Gpc.

With the current estimates on the neutrino mass, the resonance would happen at $E_\nu > 10^{21}$ eV; the decay of $Z$ bosons would produce a flux of protons, photons and neutrinos at very high energy.

Both the topological defects and the Z-burst models are disfavored by the present observations.

If the GZK effect existed, it would be a guaranteed source of high energy neutrinos. Once their flux has been measured by detecting a significant number of such neutrinos, important questions of astrophysics, cosmology and particle physics could be answered [4].

- Neutrino astronomy would become a real tool for getting knowledge of the universe. Since neutrinos are weakly interacting particles, they can travel straight across the universe, being unaffected by dust and magnetic fields. Moreover, neutrinos produced by a source at a distance $d$ would be generated within a GZK length $l_{GZK} \leq 50$ Mpc from the hadronic acceleration source; if $d \gg l_{GZK}$ they would therefore point back directly to that source, within a very small angle

$$\theta < \tan\left(\frac{l_{GZK}}{d}\right)|_{d=1\ \mathrm{Gpc}} < 3^\circ, \tag{2.22}$$

  which would be additionally restricted by kinematics (see sketch in Figure 2.6).

- From the astrophysics point of view, the measurement of the predicted flux and the identification of point sources would allow us to study the acceleration mechanism, and would test the assumed models in terms of cosmological evolution of the cosmic ray sources.

- In particle physics, since the neutrino-initiated event rate is proportional in the most general case to the integrated flux times cross section

$$R \propto \int dE_\nu \Phi_\nu(E_\nu) \sigma_{\nu N}(E_\nu), \tag{2.23}$$

the measure of the rate of neutrinos as a function of the zenith angle would make it possible to constrain experimentally the neutrino-nucleon cross section $\sigma_{\nu N}$. At present the values used for the ultra-high energy regime are extrapolated from low energy experimental data using a certain parton distribution model [40] [5]. A consistent experimental measurement would validate the model used, in a range of energy which is not possible to test in Earth-bound accelerators. Moreover, a constraint on the cross section would rule out alternative scenarios of highly-interacting neutrinos in which the cross section is predicted to be orders of magnitude higher than the one calculated in the standard model (where $\sigma_{\nu N} \sim 10^{-5} - 10^{-4}$ mb for $E_\nu = 10^8 - 10^{12}$ GeV) [41].

# Chapter 3

# Neutrino detection in South Pole ice

## 3.1 Ultra-high energy neutrino interactions

The interaction of a neutrino or an anti-neutrino with nucleons in a medium can happen through two different channels:

- neutral current interaction: the neutrino scatters on a nucleus, with exchange of a $Z$ boson and the production of a hadronic cascade:

$$\nu_l + N \rightarrow X + \nu_l \tag{3.1}$$

- charged current interaction: a neutrino interacts with a nucleon producing a cascade and a charged lepton, with exchange of a $W^{\pm}$ boson:

$$\nu_l + N \rightarrow X + l \tag{3.2}$$

The interaction probability depends on the cross sections of the two processes which are shown in Figure 3.1 for both neutrinos and anti-neutrinos. The neutral current cross section is labeled "NC" while the charged current cross section is labeled "CC". In the Figure a peak is visible for the electron anti-neutrino cross section. This peak derives from the resonance reaction (Glashow resonance [42][5]) of a $\bar{\nu}_e$ with an electron:

$$\bar{\nu}_e + e^- \rightarrow W^- \rightarrow \text{anything} \tag{3.3}$$

which happens at an energy for $\bar{\nu}_e$ equal to:

$$E_{res} = \frac{m_W^2}{2m_e} = 6.3 \cdot 10^6 \text{ GeV}. \tag{3.4}$$

The number of events for $\bar{\nu}_e$ is expected to be considerably enhanced at the Glashow resonance energy [33].

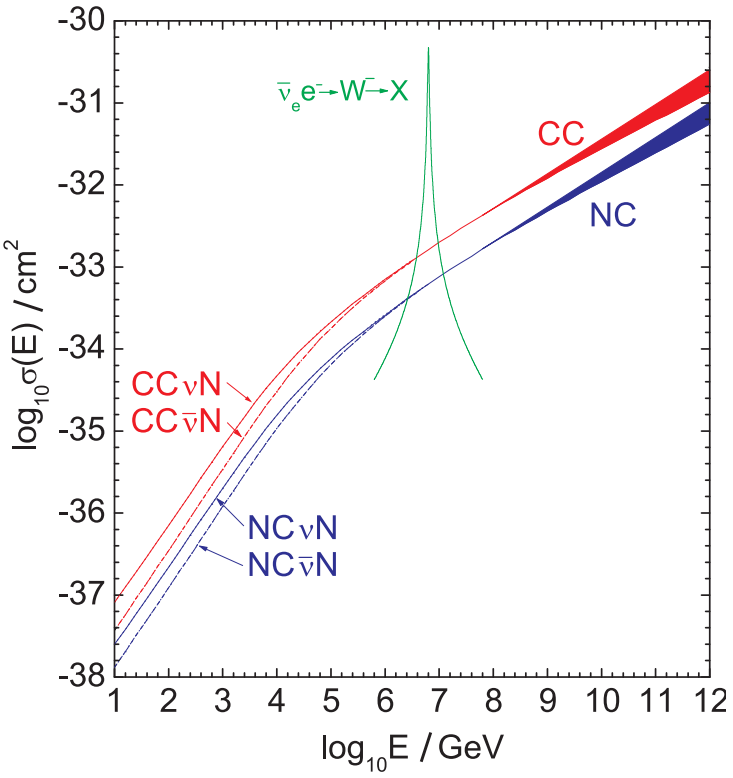


Figure 3.1: Cross sections for $\nu_l N$ and $\bar{\nu}_l N$ interactions, elaborated from [5].

It should be pointed out that for a neutrino with $E_\nu = 10^{18}$ eV which interacts with a nucleon with mass $m_N$, the center of mass energy is on the order of many tens of TeV:

$$\sqrt{s} = \sqrt{2 m_N E_\nu} \approx 45 \text{ TeV} \sqrt{\frac{E_\nu}{10^{18} \text{ eV}}} \tag{3.5}$$

The cross section at such high energies has never been measured but it is extrapolated from measurements at energies up to hundreds of GeV. The thick colored bands in Figure 3.1 indicate the uncertainties arising at high energy from different extrapolations.

A higher cross section leads to a shorter interaction length:

$$L \text{ [cm]} = \frac{1}{N_A \ \rho \ \sigma_{\nu N}(E_\nu)} \tag{3.6}$$

where $N_A = 6.022 \cdot 10^{23}$ mol$^{-1}$ is the Avogadro number and $\rho$ is the density of the Earth (in [mol]). In terms of water-equivalent density, the previous quantity can be expressed as:

$$L \text{ [cm}_{\text{we}}\text{]} = \frac{1}{N_{A,we} \ \sigma_{\nu N}(E_\nu)} \tag{3.7}$$

where $N_{A,we}$= 6.022·$10^{23}$ cm$^{-3}$ water-equivalent.

Thus, whereas the expected flux decreases with increasing energy, the fewer neutrinos will interact more often and therefore the number of registered interactions will not fall as steeply as the flux.

The interaction lengths for charged current, neutral current and the total are shown in Figure 3.2 for collisions of both anti-neutrinos and neutrinos with a target nucleon. The values overlap above $10^5$ GeV, while at lower energy the interaction length for anti-neutrinos is slightly higher due to their lower cross sections. In the case of the interaction $\bar{\nu}_e + e$, the Glashow resonance produces a dip in the $L_{int}$ (not shown in the Figure, see [5]).

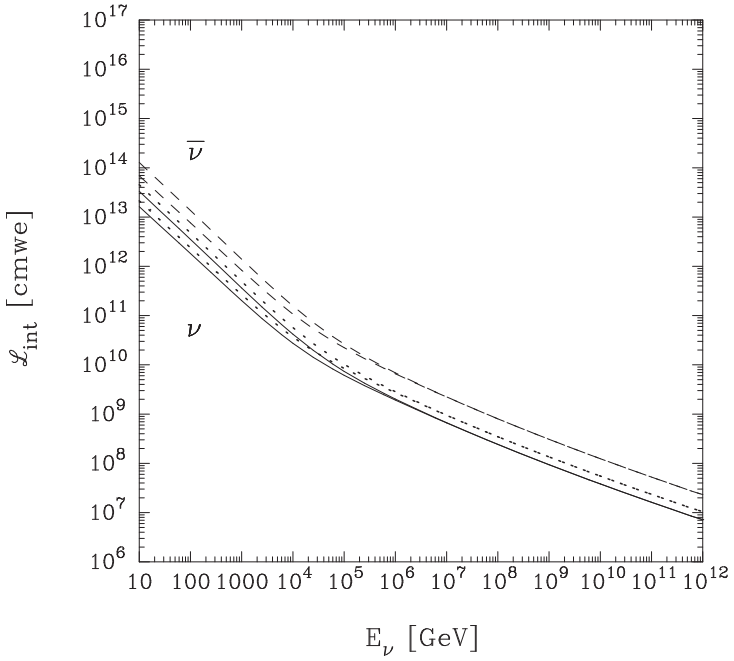


Figure 3.2: Water equivalent interaction length for both $\nu_l$ and $\bar{\nu}_l$ as a function of the energy. The dotted lines represent the charged current interaction length; the dashed lines represent the neutral current interaction length; the solid lines show the total interaction length (from [5]).

The Earth column density changes as a function of the nadir angle, therefore a (anti-)neutrino traveling through our planet encounters a certain amount of matter depending on the direction. The corresponding water-equivalent is shown in Figure 3.3 for angles between 0 and 90 degrees from the nadir direction (defined as shown in the sketch in the same Figure); the effect of the core is visible at about 0.2 $\pi$. The Earth's diameter (corresponding to the column depth at nadir angle equal to 0 degrees) has a column density corresponding to the interaction length of a neutrino with energy $E_\nu \approx 50$ TeV. Neutrinos with such or higher energy will thus be absorbed crossing the Earth. The effect is smooth and acts as

a filter, decreasing the field of view of any detector as a function of the energy: for example, the maximum angle at which a neutrino with $E_\nu \approx 10^{16}$ eV will be seen is only about 10 degrees below the horizon.

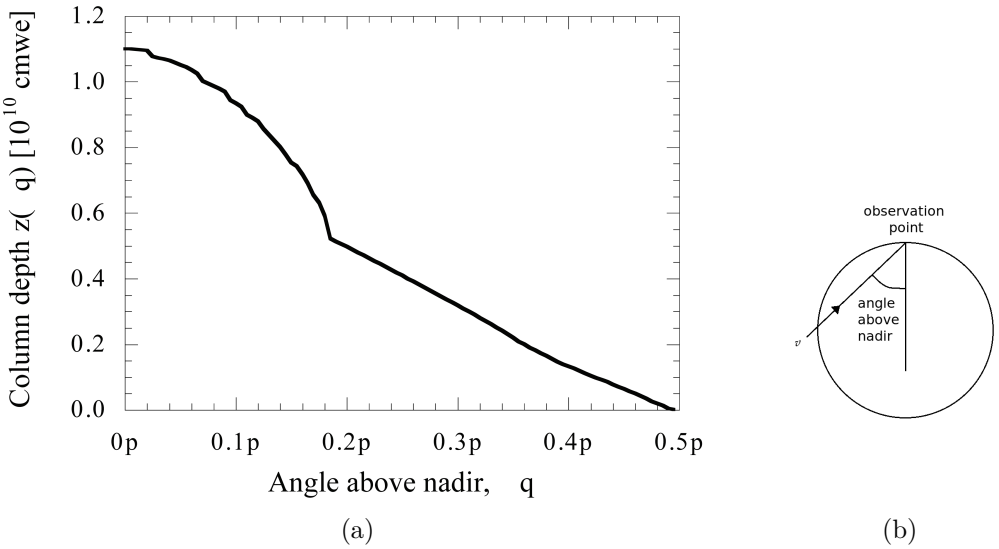


(a) (b)

Figure 3.3: Earth column density (water-equivalent) as a function of the nadir angle (from [5]).

The products of a charged current interaction are a hadronic cascade and a charged lepton:

- In the case of a $\nu_\mu$, the produced lepton is a muon, which travels a long distance before decaying;
- In the case of a $\nu_e$, the lepton is an electron which after a short path initiates an electromagnetic cascade.
- In the case of a $\nu_\tau$, the outgoing lepton is a tau. The life time of a $\tau$ is very short, but it is elongated by its relativistic speed so that the particle can travel a long distance before decaying too. The leptonic decay branching ratios for the $\tau$ have been measured by many experiments [31]:

$$\begin{aligned} \tau &\rightarrow \nu_\tau + \mu^- + \bar{\nu}_\mu \qquad b.r.\ 17.4\% \\ \tau &\rightarrow \nu_\tau + e^- + \bar{\nu}_e \qquad b.r.\ 17.8\% \\ \tau &\rightarrow \nu_\tau + \text{hadrons} \qquad b.r.\ 64.8\% \end{aligned} \tag{3.8}$$

  In all cases, the $\tau$ decays to a $\nu_\tau$, which has less energy than the original neutrino, so that the probability of interaction gets lower. This process is called $\nu_\tau$ regeneration. Charged current interactions of $\nu_\tau$ produce events

with particular signatures, called "double bang", which are characterized by the appearance of two particle cascades in a time interval on the order of the $\tau$ relativistically extended mean lifetime.

The energy from the primary neutrino is shared between the products of the interaction; the ratio between the energy of the hadronic cascade and the energy of the primary neutrino is described by the Bjorken variable $y$:

$$y = \frac{E_{had}}{E_\nu} \tag{3.9}$$

whose distribution depends on the energy of the neutrino or anti-neutrino and on the type of interaction. The mean value of this variable is 0.2 at high energies: 80% of the neutrino energy thus goes on average to the lepton, and 20% goes to the hadronic cascade. More than 70% of the energy of the hadronic cascade is converted into electromagnetic radiation, while the rest is converted into ionization and into particles which escape (like neutrons) or stop in the medium (like charged pions). Due to the many interaction steps and the different scattering angles, the hadronic cascades are wider than the purely electromagnetic cascades initiated by an electron neutrino.

## 3.2 Hybrid detection at the South Pole

There are three detectable signals associated with UHE neutrino interactions in a dense medium: optical, radio and acoustic.

When a rapidly moving charged particle travels in a material, the atoms of the medium are excited by the electric and magnetic fields associated with the particle motion. The atoms quickly return to their ground state emitting radiation. If the speed of the particle is higher than the speed of light in the medium, part of the radiation emitted by the atoms in the depolarization process builds a coherent wave front at a fixed angle with respect to the trajectory of the charged particle, dependent on the refraction index. This process happens both for a single moving charged particle and in a cascade, where a high number of charged particles is released in a contained volume. In the first case, the electromagnetic radiation builds up coherently in the optical and UV range. In the second case, the phase of the electromagnetic radiation emitted by each track is random, therefore the interference between the radiation of the multiple tracks happens decoherently in the optical bandwidth, but coherently at wavelengths larger than the shower transverse size ($10 - 30$ cm). Since an excess of negative charges is produced, a net signal in the radio bandwidth is originated for frequencies between $0.1 - 1$ GHz. More details of the physics of this process will be given in the following sections.

The number of photons emitted falls with the inverse of the wavelength squared, but it increases with the square of the total charge of the track. The optical radiation comes from a single-charged particle, and the highest signal is found

| signal type | typical spacing | energy range |
|---|---|---|
| optical | 100 m | 1 TeV-1 PeV |
| radio | 1 km | $>$ 100 PeV |
| acoustic | unknown before this study | $>$ 10 EeV |

Table 3.1: Typical energy range for a typical detector design.

to be at short wavelengths, in the UV-window. The radio signal derives from a high number of charges, proportional to the energy of the incoming neutrino; this and the coherence effect enhance the signal for UHE neutrinos in spite of the long wavelengths. The frequency of the signal affects also the propagation in the medium. Ice seems to be a quite transparent medium for both the ranges, with an attenuation length on the order of about 100 m in the optical and about 1 km in the radio bandwidth [43] [44].

The acoustic signal generation is related to a completely different mechanism: the energy deposited by a cascade heats the medium which expands, producing a pressure wave. This mechanism, called thermo-acoustic effect, has been studied and verified in the laboratory with proton and photon beams [8] [45] and it is currently under study in experiments in water or ice [46]. Before the experiment described in this work, no extensive measurements of the acoustic ice properties had ever been done *in situ*; a theoretical prediction gave an attenuation length in ice equal to a few km [47].

The attenuation length of the signal affects the optimal distance between sensors in the design of a detector. The chosen spacing influences the energy threshold of the detector itself, which depends also on the physics mechanism of production of the signal and on its propagation. An example of standard parameters for a typical detector design is presented in Table 3.1.

Since the predicted fluxes are extremely low as discussed in the previous chapter, the volume which is necessary to detect a few GZK-$\nu$ events per year is on the order of 100 km$^3$. To combine more than one technique could help on one side to extend the instrumentable volume, on the other side to better identify the events. Of course, a fundamental point is to select a material in which the different signals can be detected. Several media are being investigated as suitable target materials for neutrino detection. Water and ice are or will be the location of detectors on the order of about 1 km$^3$ now under construction and are presently under discussion for arrays on the order of 100 km$^3$, together with salt domes. Recently, permafrost has been proposed as worthy to be investigated [14].

Ice is the only medium where it is possible to detect simultaneously all the three types of signal. A suitably large volume is available, for example, in the Antarctic ice cap. The optical properties of South Pole ice are very well known and exploited, both from a theoretical and an experimental point of view; the radio properties are basically known and the acoustic ones are currently under study.

In the following sections a brief summary regarding the physics of the signal production, propagation and detection in ice is presented for each of these three detection methods, focusing on the acoustic one which is the object of study of the present work.

### 3.2.1 Optical detection

#### Signal production mechanism

The main optical detection channel of a neutrino interaction is the muon: the lepton, which travels almost in the same direction as the incident neutrino, moves at higher speed than the speed of light in the medium and therefore emits Cherenkov radiation at an angle which is defined as:

$$\cos\theta_c = \frac{1}{n\beta} \tag{3.10}$$

where $\beta = v/c$ and $n$ is the refraction index of the medium, which in ice is in the optical range $n_{ice}^{opt} \approx 1.31$. The Cherenkov emission appears for $v > c/n$; for $\beta = 1$ the angle of emission is:

$$\theta_{max} = \cos^{-1}\frac{1}{n_{ice}^{opt}} \approx 40.2^\circ. \tag{3.11}$$

The concept of the Cherenkov emission is illustrated in Figure 3.4.

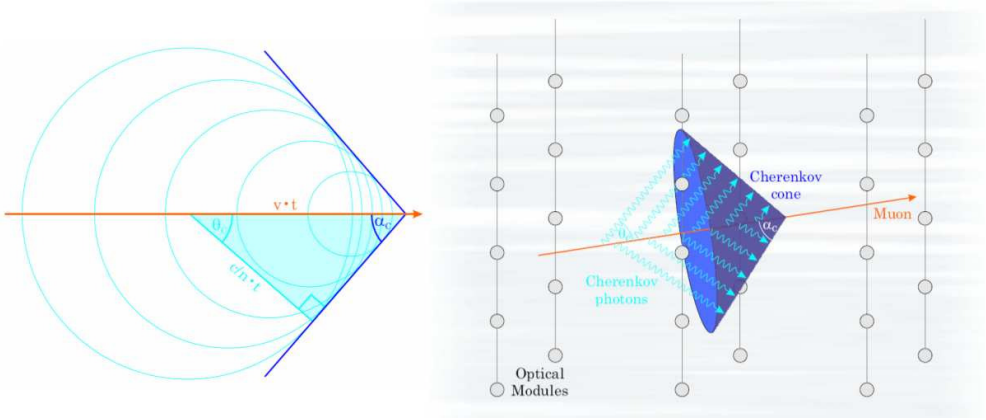


Figure 3.4: Illustration of the Cherenkov emission.

The amount of energy $dE$ emitted per unit of track-length $dx$ and unit frequency $d\omega$ by a muon moving at super-luminal velocity is given by the Frank-Tamm formula [48]:

$$\frac{dE}{d\omega dx} = \frac{\alpha\hbar z^2}{c}\omega\left(1 - \frac{1}{\beta^2 n(\omega)^2}\right) \tag{3.12}$$

where $\alpha = \frac{e^2/\hbar c}{4\pi\epsilon_0}$ is the fine structure constant, $\beta = v/c$ and $n(\omega)$ is the frequency dependent index of refraction.

Using the relations $\omega = \frac{2\pi c}{\lambda}$ and $dE = dN\hbar\omega$ it is possible to obtain the number of photons emitted by the Cherenkov effect per unit of wavelength and unit of distance traveled:

$$\frac{dN}{d\lambda dx} = \frac{2\pi\alpha}{\lambda^2} z^2 \left(1 - \frac{1}{\beta^2 n(\lambda)^2}\right) \tag{3.13}$$

for a particle of charge $z$. The number of photons is inversely proportional to $\lambda^2$ and decreases for lower values of the refraction index. Within the optical range, the refraction index does not change significantly, and the dominant effect is given by the variation of $\lambda$: the spectrum has therefore its maximum in the ultra-violet region. In addition to the light produced by the lepton, additional photons are emitted by the secondary showers created along the muon track, which are also detected in a neutrino telescope.

The detection in the UV-optical wavelength is done with photo-multiplier-tubes (PMTs) by counting the photons and it is a very well established method. Directionality of the muon is well reconstructed thanks to the long muon tracks and to the small angle between incoming and outgoing muon. The electromagnetic and hadronic showers can be detected as a short range cascade which allows only for a low-resolution directional reconstruction.

### Signal propagation in ice

The optical signal in ice (from ultra-violet region to visible) undergoes scattering and absorption [43]. Light scattering from bubbles is the dominant attenuation mechanism from the surface to about 1400 m depth. Below this depth the pressure is high enough that most of the air bubbles are converted into clathrate crystals. Clathrate crystals have almost exactly the same refraction index as ice, therefore the scattering diminishes. Only sub-millimeter bubbles and dust grains of micrometer size remain; these act as independent scattering centers since the average distance between them is larger than the photon wavelengths.

The other mechanism of attenuation of an optical signal is absorption, which depends both on the presence of impurities in the ice (like dust) and on the pure ice absorption properties ($H_2O$ modes of molecular stretching, vibration and bending, absorption of photons with energy above the band-gap energy).

Both absorption and scattering contribute to limiting the propagation of a photon in a three-dimensional propagation model. Calling $\lambda_s$ the scattering length and $\lambda_a$ the absorption length, in the approximation of large distances from a point or a linear source, the mean propagation length is [43]:

$$\lambda_p = \sqrt{\frac{\lambda_a \lambda_s}{3}} \tag{3.14}$$

where $\lambda_a$ and $\lambda_s$ are both wavelength dependent.

### Status of optical experiments

Nowadays the optical Cherenkov detection method is the best-established and known, thanks to multi-decade dedicated studies and experiments, in water and in ice. The Baikal *Neutrino Telescope* (NT-200), located in the Siberian lake Baikal at 1 km depth and built from 1993 to 1998, was the first experiment to detect atmospheric neutrinos in the TeV energy range. Nowadays other experiments such as the *Neutrino Extended Submarine Telescope with Oceanographic Research* (NESTOR), the *Astronomy with a Neutrino Telescope and Abyss environmental RESearch* (ANTARES) and the *Neutrino Ettore Majorana Observatory* (NEMO), located in the Mediterranean sea, are joining in the KM3NeT effort which aims to the construction of a 1 $km^3$-volume detector in water.

In ice, a volume of about 1 $km^3$ will be instrumented at the time of completion of IceCube, foreseen in 2011. The experiment has been developed based on the experience of the forerunner experiment *Antarctic Muon And Neutrino Detector Array* (AMANDA). Several *in situ* measurements done by AMANDA, using light sources at multiple wavelengths and depths, have brought a deep understanding of how the two attenuation mechanisms (scattering and absorption) combine, in dependence on the depth (temperature, dust concentration) and on the wavelength. The results are shown in Figure 3.5 (from [43]).

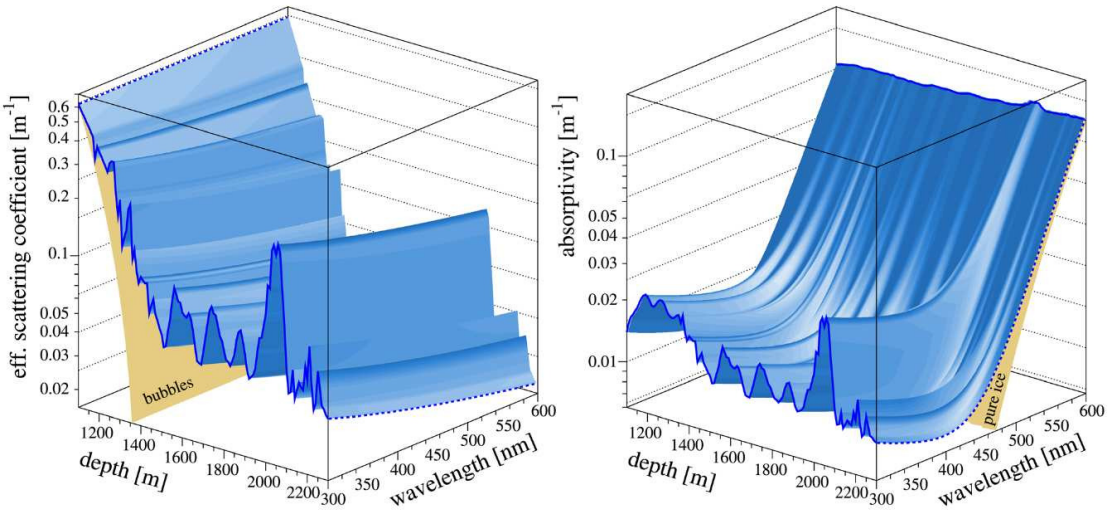


Figure 3.5: Map of scattering and absorption coefficients in South Pole ice as a function of depth and wavelength (from [43]).

AMANDA has searched for atmospheric neutrinos, point sources and diffuse fluxes at high energies. In the latter case, after five years of data taking, a flux limit of $E^2\,\Phi_{90\%\mathrm{CL}} \leq 2.7 \cdot 10^{-7}\,\mathrm{GeV\,cm^{-2}\,s^{-1}\,sr^{-1}}$ was derived for the energy region between $2 \cdot 10^5$ GeV and $10^9$ GeV with a $E^{-2}$ spectrum [49].

The IceCube design was optimized to work at energies up to 100 TeV; however, a study of the sensitivity at very high energy is currently ongoing in the energy range between $10^{7.5}$ and $10^{10.6}$ GeV. The current limit, set for the one-year data of IceCube running with only 22 of its final 86 strings, is at 90% confidence level $E^2\,\Phi_{90\%\mathrm{CL}} \leq 5.6 \cdot 10^{-7}\,\mathrm{GeV\,cm^{-2}\,s^{-1}\,sr^{-1}}$ [50].

### 3.2.2 Radio detection

#### Signal production mechanism

An illustration of the mechanism of production of the radio signal is shown in Figure 3.6.

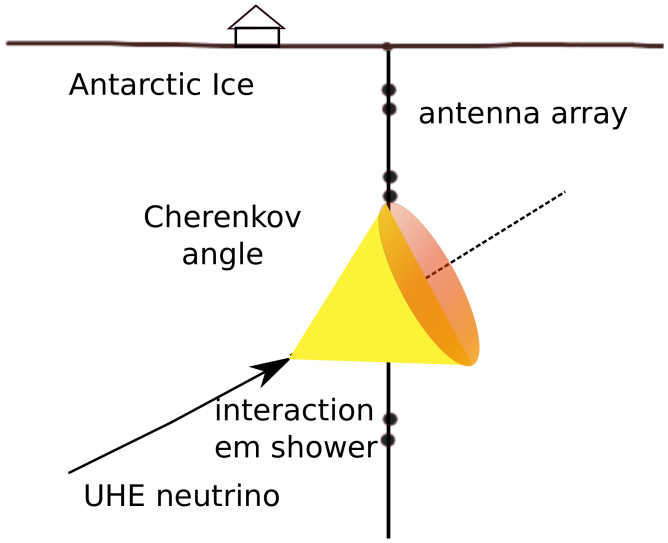


Figure 3.6: Illustration of the radio Cherenkov emission in ice by Askaryan effect.

As it has been already mentioned above, a ultra-high energy neutrino interaction generates in a medium a number of electrons and positrons which is proportional to the energy of the incoming neutrino. For a neutrino energy above 10 PeV, 90% of the pairs produced are confined in a cylindrical volume whose radius can be as large as 30 cm. Initially their speed is high ($\beta \approx 1$) but later they slow down until they stop.

Cherenkov radiation is emitted as long as $\beta > 1/n$. For particles which are produced in a small volume and in a time scale shorter than the field propagation time through the generation volume, the phase of emission is the same, and the electric field for each charge type sums coherently. This happens for wavelengths larger than the transverse size of the shower.

The effect of the two induced electric fields would cancel out if the number of particles produced for each charged type was the same. Askaryan predicted in

1961 that the number of electrons would be superior to the number of positrons by about 20%, thanks on one side to positron annihilations and on the other side to electron Compton scattering by photons [7]. Both processes play in favor of an excess negative charge.

The asymmetry of the charge results in an unbalanced electric field. Figure 3.7 shows the profile of the electric field as a function of the polar emission angle for different frequencies. The interference pattern appears as a peak in proximity of the Cherenkov angle. In the ice, where the index of refraction at a frequency of about 1 GHz is $n_{ice}^{radio} \approx 1.78$, the peak angle for the radio Cherenkov emission is $\theta_c \approx 56^\circ$ (assuming relativistic speed of the particle $\beta = 1$) [51].

The maximum appears at a frequency which is defined by the lateral distribution of the shower. The transverse size of the charge generation volume is approximately $r \approx 10 - 30$ cm. The coherence effect happens for wavelengths longer than the transverse size of the cascade. This corresponds to frequencies $f$:

$$f < \frac{c}{r\, n_{ice}^{radio}} \approx 1 \text{ GHz}. \tag{3.15}$$

The width of the peak is inversely proportional to the longitudinal depth of the shower. The excess of negative charge is always about 20% of the total charge of the shower, which is proportional to the energy. The projected track length associated with the excess charge, which is therefore about 1/5 of the total track length, is approximately proportional to 1000 m $\cdot$ ($E_0$/1 TeV). The total shower longitudinal length increases, while the coherent peak width decreases as the shower energy $E_0$ increases [52] [51].

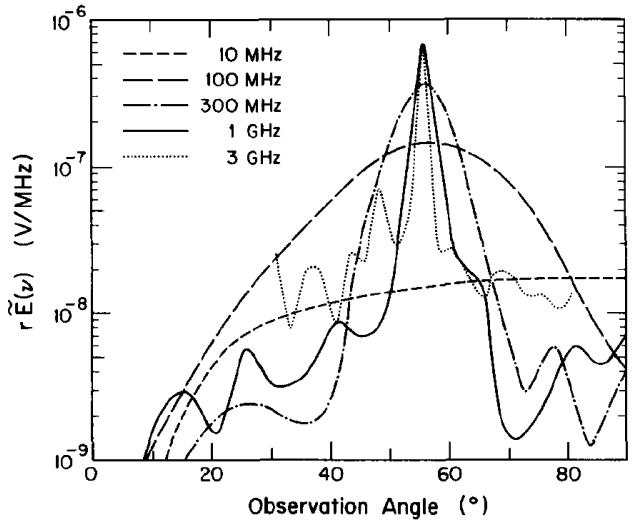


Figure 3.7: From [51]: distribution of the electric field times distance generated by a 10 TeV electron as a function of the observation angle, *i.e.* the polar angle of the radiation with respect to the shower axis.

Zas et al. in 1991 [51] calculated the total power $W$ irradiated by the cascade induced by a neutrino of energy $E_0$ [51], integrating the Frank Tamm formula (equation 3.12) over the effective longitudinal length $l$ of the cascade and assuming a net charge $ze$:

$$dE = \frac{(ze)^2}{c^2} \cdot \omega \left(1 - \frac{1}{\beta^2 n^2}\right) l \Delta\omega \tag{3.16}$$

In spite of a disadvantageous dependence on the frequency, thanks to the coherence of the radiation the signal strength depends on the excess charge $(ze)^2$; since $ze$ is proportional to the incident neutrino energy, the signal is proportional to the square of the energy of the neutrino.

### Signal propagation in ice

Once produced, the radio signal in ice undergoes geometrical scaling in amplitude $1/r$ and attenuation $e^{-d/\delta}$ where $\delta$ is the attenuation length for radio signal in ice. The electromagnetic response of a certain medium is given by the complex dielectric permittivity $\epsilon = \epsilon'(\omega,\hat{\mathrm{n}}) + i\epsilon''(\omega,\hat{\mathrm{n}})$, where $\omega$ is the angular frequency and $\hat{\mathrm{n}}$ is the polarization vector [53]. The real part of this quantity is related to the refraction index and the speed of propagation of the wave ($v = c/\sqrt{|\epsilon'|}$) and enters in the mechanism of generation of the radio signal (see equation 3.16). In ice the refraction constant in the radio frequency range is higher than in the optical (1.78 vs. 1.31), which leads the signal to be enhanced of a factor of about 2 (see equation 3.16 and 3.13). The imaginary part of the dielectric permittivity is related to the absorption. The absorption in ice at about 1 GHz seems to be very low: the attenuation length in the radio bandwidths has been estimated from depth-integral measurements to range from 250 to 1000 m [44]. This would make ice a natural material to exploit this detection technique.

The Antarctic ice cap is the biggest and macroscopically most homogeneous volume of ice in the world. However to build a reliable model to be applied in the reconstruction of neutrino interactions requires a deep understanding of the dielectric permittivity. This is quite difficult since the ice cap has very different features of the temperature profile and ice density, which are strictly correlated with the attenuation length. An extensive effort is currently underway to understand in detail the radio ice properties [44] [53]. The shallower region is believed to be the most interesting for radio detection since at deeper depths the increase of temperature and conductivity decreases the attenuation length. Nevertheless a direct and exact measurement in the firn range is quite difficult due to the rapid variation of the refraction index profile.

### Status of radio experiments

Nowadays the radio method has been exploited by the *Radio Ice Cerenkov Experiment* (RICE), a radio array deployed at the South Pole [9] [10] and by the *ANtartic*

*Impulse Transient Array* (ANITA), a NASA long-duration balloon payload which observes radio emission from the Antarctic ice surface [11]. Similar concepts for large collecting power have been used by the *Fast On-orbit Recording of Transient Events* (FORTE), observing the Greenland ice cap [35]. A good overview of the experiments currently in operation or planned is given in [54]. The limit set by the latest ANITA flight is of $E^2\,\Phi_{90\%\mathrm{CL}} \leq 2 \cdot 10^{-7}\,\mathrm{GeV\,cm^{-2}\,sr^{-1}}$ for a $E^{-2}$ spectrum in the energy region $10^{18.5} \leq E \leq 10^{23.5}$ eV [11].

### 3.2.3 Acoustic detection

#### Signal production mechanism

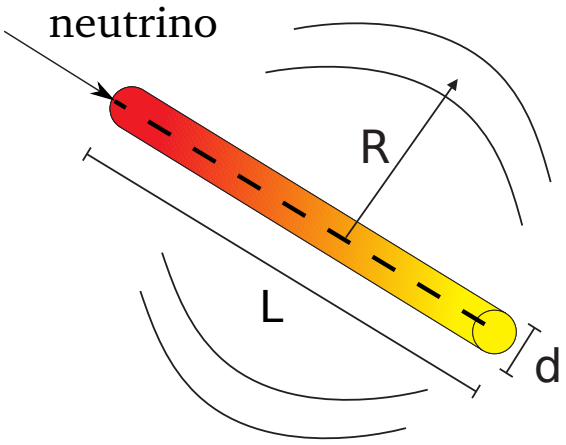


Figure 3.8: Scheme of principle of acoustic emission.

The production of an acoustic signal which follows the energy deposition in a medium is described by the thermo-acoustic model and it is pictured in the drawing represented in Figure 3.8. The model was developed by G. A. Askaryan et al. for high energy particle showers in water [8]. In 1979, L. Sulak, J. Learned et al. verified experimentally the model using proton beams from an accelerator [45].

For liquids, the model is quite simple. The deposit of a certain energy $E$ in a volume $V$ causes in the medium a local increase of temperature $\Delta T$ determined by:

$$\Delta T = \frac{E}{\rho C_p V} \tag{3.17}$$

where $\rho$ is the density of the material and $C_p$ is the heat capacitance (*e.g.* in units [J kg$^{-1}$ K$^{-1}$]). The increase of the temperature causes the expansion of the volume of the amount:

$$\Delta V = \alpha V \Delta T = \frac{\alpha}{\rho C_p} E \tag{3.18}$$

or, equivalently

$$\frac{\Delta V}{V} = \frac{\alpha}{\rho C_p}\varepsilon \tag{3.19}$$

which are simply gotten from the definition of the thermal expansion coefficient $\alpha = 1/V(\partial V/\partial T)$ (in units *e.g.*: [$K^{-1}$]) and defining the energy density $\varepsilon = E/V$ [*e.g.* J/$cm^3$].

When a certain energy density $\varepsilon(\vec{r}, t)$ is deposited in the medium, the evolution in time and space of the pressure density $p(\vec{r}, t)$ is described by the inhomogeneous wave equation:

$$\nabla^2 p(\vec{r}, t) - \frac{1}{v_l^2}\frac{\partial^2 p(\vec{r}, t)}{\partial t^2} = -\frac{\alpha}{\rho C_p}\frac{\partial^2 \varepsilon(\vec{r}, t)}{\partial t^2} \tag{3.20}$$

where $v_l$ is the longitudinal speed of sound in the medium, and where the source or forcing term on the right side comes from the previous equation 3.19.

The solution of equation 3.20 is the Kirchoff integral [8], which describes how the pressure at a certain coordinate and time $p(\vec{r}, t)$ depends on the energy density at a distance and time $(\vec{r}', t')$ where $t' = |\vec{r} - \vec{r}'|/v_l$:

$$p(\vec{r}, t) = \frac{\alpha}{4\pi\rho C_p}\int \frac{\partial V}{|\vec{r} - \vec{r}'|}\frac{\partial^2}{\partial t^2}\varepsilon\left(\vec{r}', t - \frac{|\vec{r} - \vec{r}'|}{v_l}\right) \tag{3.21}$$

in which the integration extends over the energy deposition volume.

A neutrino-induced particle cascade releases energy in the medium in a much shorter time than the characteristic time scales for heat dissipation in the medium. In a very simplified model, the energy distribution in space can be approximated as a cylinder, with thickness diameter $d$ and length $L$. If these two assumptions are made, the solution of equation 3.21 leads to the result that, in the plane perpendicular to the cascade at a distance $R$ (such that $L \ll R \ll L^2\pi/2d$), the pressure amplitude $p$ will decrease proportionally to $\sqrt{R}$:

$$p(R) \propto f_{peak}^2 \frac{\alpha}{\rho C_p}\frac{E}{\sqrt{R}} \tag{3.22}$$

where the frequency $f_{peak} = v_l/2d$ is the main component of the spectral content of the signal.

In time, for a fixed location, the pressure evolution generates a bipolar pulse. Figure 3.9 shows the pressure amplitude as a function of the time in a plane perpendicular to the cascade axis, at a position corresponding to the maximum of the shower, for three different assumptions on the energy distribution (see [55]).

The description of the acoustic pulse generation given up to here holds for liquid media. In solids, the deposition of energy excites the generation of both transverse and longitudinal modes, which propagate each at their specific speeds. It can be therefore assumed that at least two equations will be needed to describe the energy propagation. The propagation of waves depends on the elastic properties of the medium, so that to find an analogous relation, one has to deal with the movement

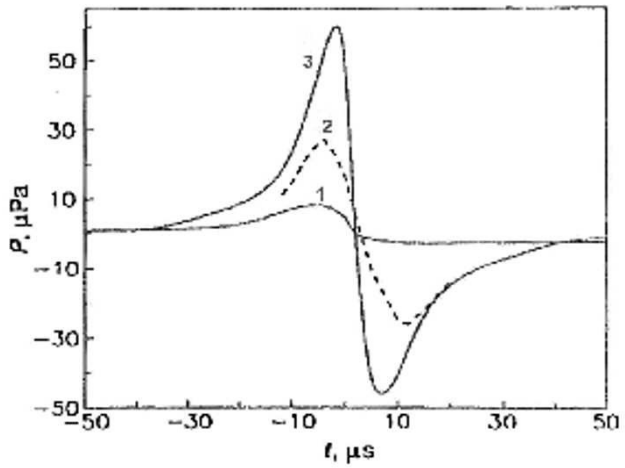


Figure 3.9: Bipolar pulse produced according to three different models of the thermo-acoustic effect (from [55]).

of atoms from their nominal location. The topic has been treated in many solid state physics books, for example in [56]. A force inducing a displacement $\vec{u}(\vec{r},t)$ in the material, can be expressed, in each of its components, in terms of the stress tensor. Each of the components of the stress tensor is related to the deformation of the medium in each possible direction by the elastic constants. In the case of an isotropic body, the problem is greatly simplified since an applied force will give the same displacements (relative to the direction of the force) no matter the direction in which the force is applied. The number of elastic constants drops to two, one for the transverse modes and one for the longitudinal modes. These two constants can be expressed using the so called *Lamé* parameters $\lambda$ and $\mu$. Now, if the displacement $\vec{u}$ is expressed in terms of a scalar and a vector component as:

$$\vec{u} = \nabla\phi + \nabla \times \vec{\psi} \tag{3.23}$$

it is possible to obtain, from the Hooke's law for solids, two equations similar to equation 3.22, one describing the propagation of longitudinal waves (called pressure or $P$-waves) and the other describing the propagation of transverse waves (called shear or $S$-waves):

$$\begin{aligned} \frac{\partial^2\phi}{\partial t^2} - v_l^2\nabla^2\phi &= v_l^2\frac{\alpha}{\rho C_p}\varepsilon(\vec{r},t) \\ \frac{\partial^2\vec{\psi}}{\partial t^2} - v_t^2\nabla^2\vec{\psi} &= 0 \end{aligned} \tag{3.24}$$

where

$$v_l = \sqrt{\frac{\lambda+2\mu}{\rho}} \tag{3.25}$$

$$v_t = \sqrt{\frac{\mu}{\rho}}$$

are the speeds of longitudinal and transverse waves in the medium in terms of the *Lamé* parameters. The equations 3.24 hold for homogeneous isotropic solids and correspond to equation 3.22 for liquids. In nature no crystal is perfectly isotropic as far as elastic properties are concerned: given a certain volume of material, if crystals are aligned in a particular orientation, there will be equations equivalent to 3.24 for every direction corresponding to a specific crystal axis; if crystals are randomly aligned, equivalent parameters will be defined as result of the integration along a specific direction and path.

Notably, from the comparison of equation 3.24 and 3.22 it is easy to see that both in liquids and in water the strength of the signal is proportional to the so called *Grüneisen* parameter:

$$\gamma_G = \langle v_l \rangle^2 \frac{\alpha}{C_p}. \tag{3.26}$$

This dimensionless factor expresses how efficient the conversion between heat and elastic energy is for a certain medium and allows for the comparison of media with different physical properties. The values for different media are shown in Table 3.2 from [47] [57].

| **parameter** | | **units** | **ocean** | **ice** | **rock salt** |
|---|---|---|---|---|---|
| temperature | T | [°C] | 15 | -51 | 30 |
| density | $\rho$ | $\left[\frac{\text{g}}{\text{cm}^3}\right]$ | 1 | 0.92 | 2.16 |
| longitudinal speed of sound | $\langle v_l \rangle$ | [m/s] | 1530 | 3920 | 4560 |
| thermal expansion coefficient | $\alpha$ | $[\text{K}^{-1}]$ | $25.5{\cdot}10^{-5}$ | $12.5 \cdot 10^{-5}$ | $11.6 \cdot 10^{-5}$ |
| heat capacitance | $C_p$ | $\left[\frac{\text{J}}{\text{kg}\cdot\text{K}}\right]$ | 3900 | 1720 | 839 |
| peak frequency | $f_{peak}$ | [kHz] | 7.7 | 20 | 42 |
| Grüneisen parameter | $\gamma_G$ | | 0.15 | 1.12 | 2.87 |

Table 3.2: Parameters for the conversion of heat into acoustic energy in different media (from [57] [47]).

From the comparison of the data collected in Table 3.2 it can be seen that the acoustic signal produced by a certain energy deposition in ice is 7.3 times higher than the signal produced by the same energy deposited in sea water. The pressure wave scales again in the near field approximation as in equation 3.22; in ice the spectrum of the signal generated by a neutrino-induced cascade is expected to exhibit a dominant component around 20 kHz.

### Signal propagation in ice

The expectations regarding the acoustic attenuation properties are based on the theory developed in [47]. The model assumes that there are two different mecha-

nisms of attenuation of the acoustic waves in ice: scattering and absorption.

Scattering occurs when the incoming pressure wave is deviated from a straight trajectory due to non-homogeneity in the medium. This can happen with or without loss of energy. In ice, the two main sources of scattering are bubbles and ice crystals. As said on page 26, below 1400 m depth most of the bubbles have been converted into clathrate crystals; the density of these crystals is similar to ice, so the effect on a traveling acoustic wave is expected to be negligible. At shallower depths, bubbles are assumed to act as independent scattering centers, since the mean distance is larger than their linear dimension. The scattering coefficient follows the Rayleigh law and it is proportional to [47]:

$$b_{bubble}[\mathrm{m}^{-1}] = 2.68 \cdot 10^{-10} (n_b/200\ \mathrm{cm}^{-3})(d_b/0.02\ \mathrm{cm})^6 (f/10\ \mathrm{kHz})^4 \tag{3.27}$$

where $n_b$ is the density of bubbles, $d_b$ is the bubble diameter and $f$ is the frequency. Studies of samples from an ice core from Byrd Station have revealed a density of bubbles of about 200 $\mathrm{cm}^{-3}$ down to a depth of 800 m, below which the density decreases monotonically; also the mean bubble diameter was found to decrease from about 0.1 cm at the surface down to about 0.016 cm at 1 km depth [58].

The other possible source for scattering is the boundaries of the crystal grains. The grain size increases with depth under the effect of an increasing pressure; from measurements done in Greenland and in Antarctica, it is believed that the mean grain diameter is less than 0.2 cm in the top 600 m, reaching a value of 0.4 cm at 1500 m depth. For the range of frequencies in which we are interested (few kHz to 100 kHz) the acoustic wavelength $\lambda$ is on the order of a few tens of centimeters to a few centimeters: this means that it is generally much larger than the diameter of the grain $d_g$ so that the Rayleigh regime ($\lambda > 2\pi d$) applies. The scattering coefficient is different for longitudinal and transverse waves, and it depends on $d_g^3 f^4$ and on a combination of the wave speeds. The normalization parameters have been calculated in [47] assuming that all grains have the same diameter $d_g$. For longitudinal waves, the scattering coefficient was found to be:

$$b_{g,l}[\mathrm{km}^{-1}] = 5 \cdot 10^{-4} (d_g/0.2\ \mathrm{cm})^3 (f/10\ \mathrm{kHz})^4. \tag{3.28}$$

The second mechanism of attenuation is absorption. An acoustic wave penetrating into the ice lattice produces a conspicuous number of interactions within and between grains. Part of the energy of the pressure wave is lost due to internal friction, which converts part of the pressure wave energy into internal energy. These interactions are related to several phenomena in addition to the standard excitation of phonons and thermo-elastic modes of the lattice. Until recently, the dominant effect had been assumed to be connected to changes of the orientations of the dipole moments of $H_2O$ molecules and to movements of protons from one bond site to another in response to the acoustic wave. The internal friction induced by this process is featured by a particular relaxation time

$$\tau_m = \tau_0 \exp(U/k_B T) \tag{3.29}$$

where $U$ is the activation energy for this process, $U \approx 0.6$ eV, $T$ is the temperature and $k_B$ is the Boltzmann constant. The loss of energy is a resonant phenomenon which is a function of frequency and has a maximum at $f = 1/2\pi\tau_m$. The absorption coefficient was calculated in [47] by multiplying the energy loss $\delta$ by the frequency $f$ and by the inverse of the sound speed $v_l$, with the following result:

$$a_L[\mathrm{m}^{-1}] = \frac{f}{v_l}\delta = \frac{1}{v_l}\frac{\delta_{max} 4\pi f^2 \tau_m}{1 + 4\pi^2 f^2 \tau_m^2} \tag{3.30}$$

which increases with frequency up to $f_s = 1/2\pi\tau_m$, while for $f > f_s$ it is independent of frequency. $\delta_{max}$ is a constant, independent of frequency, with an experimentally determined value that depends on the wave mode and the direction of propagation. An average value for $\delta_{max}$ has been found to be approximately 0.008, while the relaxation constant $\tau_0 \approx 3 \cdot 10^{-16}$ s. The equation 3.30 depends also on the temperature, in the way that the value at which saturation occurs moves to higher frequencies for higher temperature. Figure 3.10 shows the agreement between the theory prediction and two experimental points obtained in West Antarctica and in Greenland with seismic techniques.

A plot summarizing the expectation from the three mechanisms above is shown in Figure 3.11 for a reasonable choice of values of temperature, grain and bubble diameter. From the previous calculations, the absorption mechanism turned out to be more important than scattering from grain boundaries and bubbles in the frequency range between 10-100 kHz. At larger depths, the absorption is expected to increase due to temperature dependence; taking this into account, the acoustic attenuation length was predicted to range from 8.6 km at the surface to 4.8 km at 1 km depth to 0.2 km at 2 km depth.

### Status of acoustic experiments

Several experiments around the world investigate the applicability of the acoustic method:

- ONDE (*Ocean Noise Detection Experiment*), built within the NEMO project, is located in the Mediterranean sea near Catania. It has operated with four broadband hydrophones in 2005-2006 and it is going be developed with the addition of eight hydrophones in 2010 [59];

- AMADEUS *Antares Modules for Acoustic DEtection Under the Sea* within the optical neutrino observatory ANTARES, with 36 acoustic sensors deployed near the Marseille coast [60];

- ACORNE (*Acoustic COsmic Ray Neutrino Experiment*) which uses a military array in Scotland with eight hydrophones, in operation since December 2005 [61];

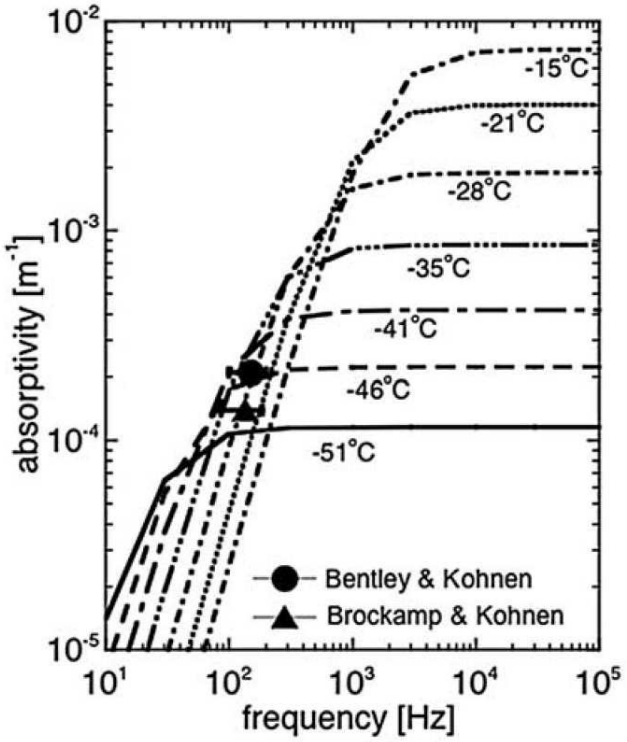


Figure 3.10: Theoretical temperature and frequency dependence of acoustic absorption in South Pole ice. Two experimental points obtained are shown (from [47]).

- SAUND (*Study of Acoustic Ultra-high energy Neutrino Detection*) uses a military hydrophone array set in Bahamas. The experiment had a first phase with seven hydrophones in 2004-2005, and set the only existing acoustic neutrino detection limit, even if still not competitive with the limits set by radio experiments. Since July 2006 the experiment, developed into a second phase with 49 hydrophones, has taken data which is now under analysis [62].

Only one experiment is running in ice, namely the SPATS experiment which is the subject of this thesis and will be discussed in detail in the following chapters.

## 3.3 Advantages of hybrid detection

The state of the art for the three detection channels is quite different. The generation of an optical Cherenkov signal is a well known phenomenon for neutrinos from the MeV range (solar and supernova neutrinos) up to multi-GeV (atmospheric neutrinos produced by the interaction of cosmic rays with the atmosphere nuclei). The most current optical experiments searching for a UHE neutrino signature can

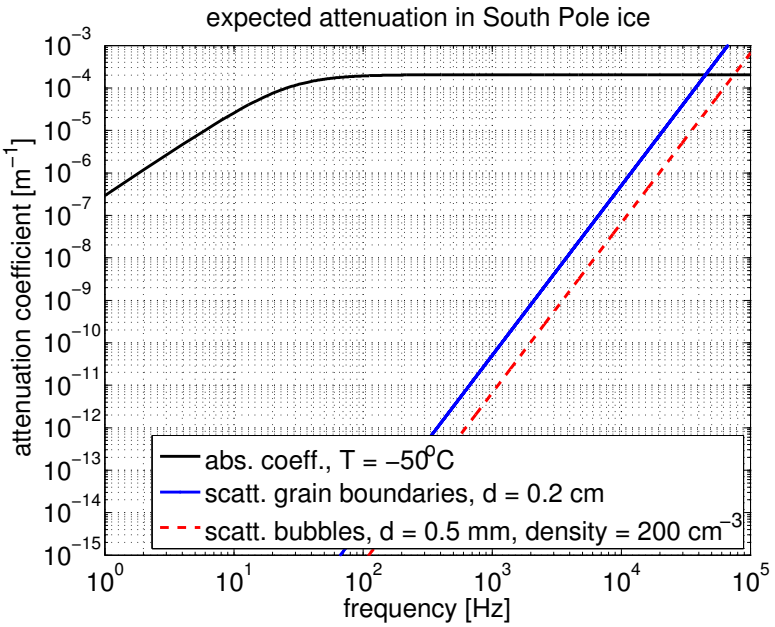


Figure 3.11: Combination of different attenuation mechanisms as a function of the frequency as expected in South Pole ice for a temperature of $-50\,^{\circ}\mathrm{C}$, grain diameter 0.2 cm and bubbles with diameter 0.5 mm and density 200 cm$^{-3}$ (data from [47]).

take advantage of the atmospheric neutrino background in the lower energy range as a calibration tool. At present, no UHE neutrino has ever been detected.

The mechanism of production of the radio and the acoustic signals has been verified experimentally with lasers and proton accelerators in many laboratories in hadronic interactions, but never directly in a neutrino interaction. The radio and the acoustic signal are expected to appear only at very high energies, where hadronic interaction models are known to have large systematic uncertainties. Moreover, such high-energy neutrinos are not reproducible in the laboratory; therefore no obvious equivalent calibration signal exists, at high or at low energy.

All experiments or R&D projects use only one single detection method: either optical, or radio, or acoustic. The radio and the acoustic method offer the advantage of an attenuation length generally much longer than that of light; they could therefore be used to instrument a larger volume, extending the sensitivity range of a detector to higher energies. With a sufficiently large detector, in ice it would be possible in principle to observe simultaneously the three different signals generated by a neutrino interaction. To identify hybrid events, detected by more than one technique, would be of great advantage:

- the detection of coincident events with the optical method and the radio or the acoustic methods would allow for the calibration of these “new methods”

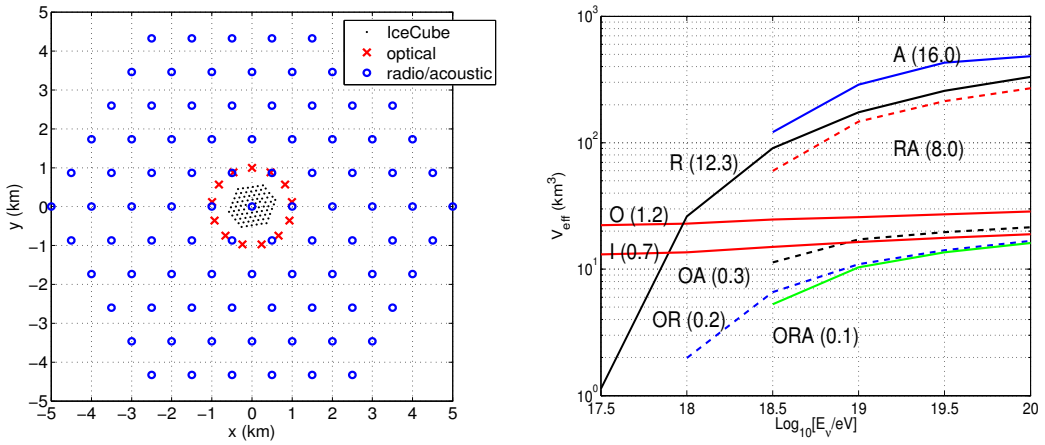


(a) (b)

Figure 3.12: (a): Geometry of a 100 km$^3$ detector simulated in [12]. (b): Effective volumes for each combination of detection methods. The numbers on the lines indicate the number of GZK events expected in one year from the ESS model as detected by the optical (O), radio (R), acoustic (A) methods and by any of their combinations.

with a well known one;

- events detected both by the radio and by the acoustic techniques would allow for a reciprocal calibration of these methods at higher energy where there is no overlap with the optical method;
- the identification of events with more than one channel would strengthen the credibility of the discovery, enhancing the background rejection by the use of multiple channels of detection;
- to combine the information from the muon track (optical channel) with the information from the hadronic cascade would improve the energy and the direction reconstruction.

Some simulations have been performed to verify the potential of hybrid detection at the South Pole. These and the corresponding results are summarized in the following sections.

## 3.4 Simulations

### 3.4.1 Simulation of a hybrid 100 km$^3$ detector

In order to study the detection capabilities in the ultra-high energy range of a large volume detector combining optical, radio and acoustic sensors, a 100 km$^3$

hybrid detector was simulated in 2005 [12]. The geometry of the detector is shown in Figure 3.12(a).

The detector was simulated as built around the optical neutrino observatory IceCube, at the geographic South Pole. Thirteen optical IceCube-like strings were simulated at a radial distance of 1 km, around the perimeter of IceCube. Each had 60 optical modules per string, spaced every 17 m between 1.4 and 2.4 km depth [63]. 91 radio/acoustic strings were surrounding the optical array: each string was equipped with five radio receivers (every 100 m between 200 m and 600 m depth) and with 300 acoustic sensors (every 5 m, at depths from 5 m to 1500 m).

The effective volumes were calculated for each method independently as a function of the energy and overlapping the detection channels. The results are shown in Figure 3.12(b). The event rate was obtained folding the effective volumes with the predicted neutrino flux (following the model of Engel-Seckel-Stanev). This highlighted the possibility to detect about 20 GZK neutrinos per year, 40% of which were in the form of hybrid events detected by more than one technique.

As far as the acoustic signal propagation is concerned, some assumptions were made to run the simulation. For the attenuation length the ice model from [47] was assumed. To validate this model, the South Pole Acoustic Setup was built and installed, with the goal of measuring *in situ* the ice properties. While the experiment was taking data, some effort was taken in order to study the advantages of an intermediate step towards a big detector.

### 3.4.2 Simulation of an UHE extension to IceCube

A hybrid extension to IceCube, combining optical, radio and acoustic instrumentation, was simulated in order to evaluate the improvement of the detector sensitivity at high energy in case of a redesign and relocation of the last IceCube strings with the addition of acoustic and radio sensors. In the geometry simulated, twelve of the foreseen 80 strings of IceCube were rearranged at 1 km radial distance; half of these strings, plus one at the center of the array, were equipped additionally with hybrid technology: five radio receivers between 200 and 600 m depth and 60 acoustic sensors every 15 m between 250 and 1100 m were included in each string in the simulation. A scheme of the strings can be seen together with the geometry in Figure 3.13; it should be noticed that the scale is very different compared to 100 $km^3$ detector shown in Figure 3.12(a) and the hybrid extension simulated is much smaller.

Details regarding the simulation are discussed in [64]; the effective volumes resulting for the three detection techniques are shown in Figure 3.14. Folding the effective volumes with the ESS expected flux gave a number of GZK events per year of about twice the one obtained by IceCube alone. The complete list of events separated method by method is listed in Table 3.3.

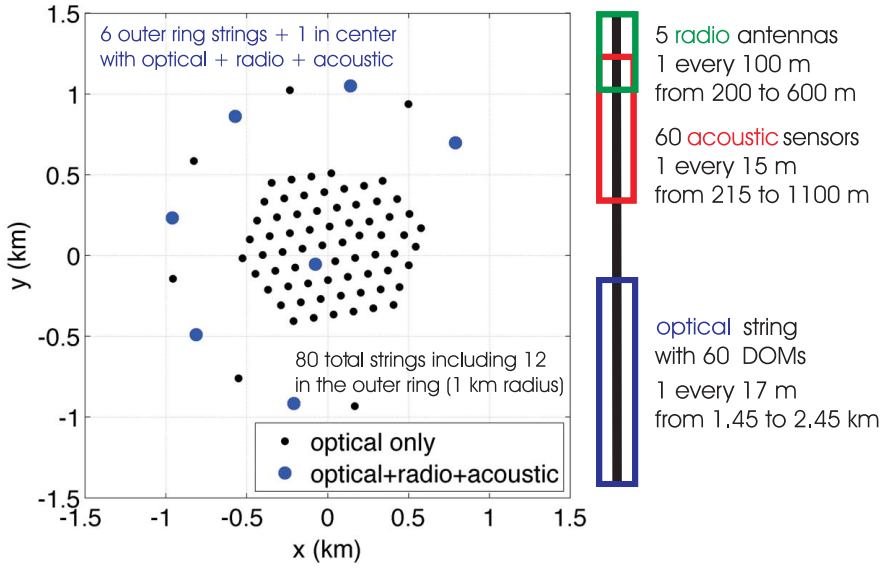


Figure 3.13: Geometry considered for the UHE extension to the IceCube detector. Simulated instrumentation, as a function of the depth along a single string, is schematically indicated on the right.

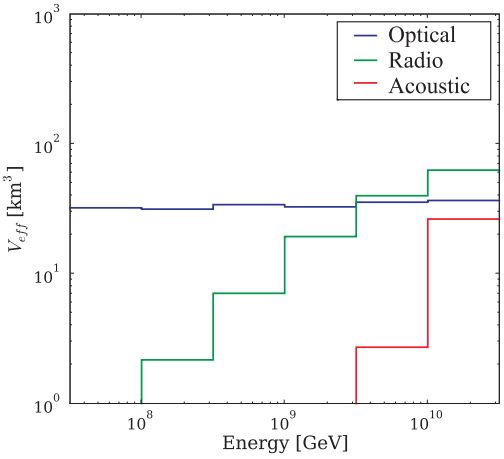


Figure 3.14: Effective volume calculated for the UHE extension to IceCube for the optical, the radio and the acoustic detection method in the energy range of the simulated neutrino sample.

| **Detection option** | **GZK events per year** |
|---|---|
| IceCube | 1.78 |
| Optical | 3.09 |
| Radio | 1.31 |
| Acoustic | 0.16 |
| Optical + Radio | 0.15 |
| Optical + Acoustic | 0.03 |
| Radio + Acoustic | 0.08 |
| Optical + Radio + Acoustic | 0.01 |
| **Total** | 4.32 |

Table 3.3: GZK rates per year from the simulated geometry. "Optical" refers to IceCube plus the optical channel of the extension.

# Chapter 4

# The South Pole Acoustic Test Setup and the Pinger

## 4.1 SPATS

The *South Pole Acoustic Test Setup* was designed to measure the acoustic properties of the ice at the South Pole, in order to investigate the feasibility of acoustic neutrino detection. The goals are to determine the noise floor, the sound speed profile (as function of the depth), the rate and features of the background transient events, and the acoustic attenuation length.

The detector consists of four strings, which were deployed in 2007 in the upper level of IceCube holes after the installation of the optical string. The horizontal baselines of the SPATS array are AB = 125 m, AC = 421 m, AD = 249 m, BC = 302 m, BD = 330 m, and CD = 543 m. A schematic view of the detector is shown in Figure 4.1. Every acoustic string has seven modules, each with a transmitter and a sensor, which are installed at depths between 80 and 500 m.

The modules of each string are connected via a copper cable to a PC located inside a robust aluminum box. The four PCs communicate via DSL connection with a central computer, located in the *IceCube Counting Laboratory* (ICL).

In addition to the instrumentation deployed in the ice, a retrievable transmitter, called *pinger*, has been developed to be used in water-filled holes just before the installation of the IceCube string. Until now the pinger was in operation for two seasons. An aerial view of the South Pole, showing the location of the SPATS strings within the IceCube experiment, is presented in Figure 4.2. The holes where the pinger was run are highlighted in two colors which differentiate the seasons.

### 4.1.1 In-ice components

The three strings named A, B and C, were installed in January 2007; the instrumented depths are 80, 100, 140, 190, 250, 320 and 400 m. The fourth string, called D, was installed in December 2007 and is equipped with instrumentation at the

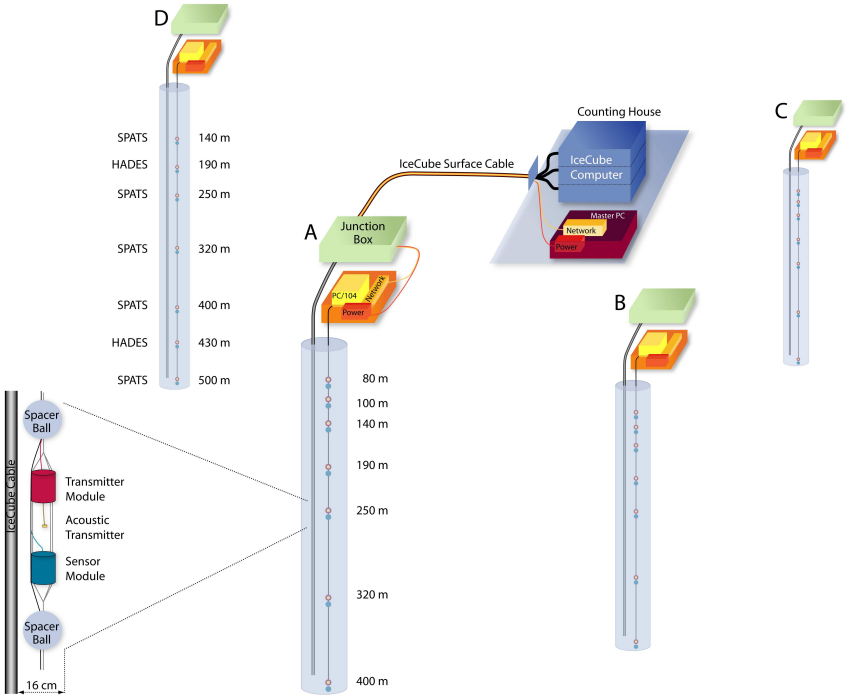


Figure 4.1: Schematical view of the SPATS array.

depths of 140, 190, 250, 320, 400 and 500 m. The unequal spacing was chosen to properly investigate the acoustic properties which are expected to change more rapidly in the upper level of the ice cap. Each of the transmitters and sensors is named with the abbreviation "X S/T level": *X* is the letter indicating the string (*A*, *B*, *C* or *D*); *S/T* stays for "sensor" or "transmitter"; *level* is a number between 1 and 7 and refers to the installation level (with different meaning in terms of depth, as explained before). For example, AS6 is the name of the sensor of String A deployed at level 6 (320 m depth).

For the strings A, B and C all the acoustic stages are equal: a SPATS transmitter and a SPATS sensor, as pictured in Figure 4.3. The final design of the stage was the result of a long development phase, which has been described in detail in [65]; here only a summary of the operational features is given.

The principle of sound production and detection is the piezoelectric effect: both transmitters and sensors use piezoelectric ceramics which are read out or pulsed respectively to sense or emit a pressure wave. In both cases, the material of the piezoelectric elements, produced by *PI-ceramic*, is lead zirconate titanate (PZT), but the geometrical shape and features are different.

Each transmitter module consists of a ring-shaped piezoelectric ceramic and of a high-voltage pulser board which is located in a pressure housing. The piezoelectric ceramic has an external radius of 20 mm, an internal radius of 18 mm and it

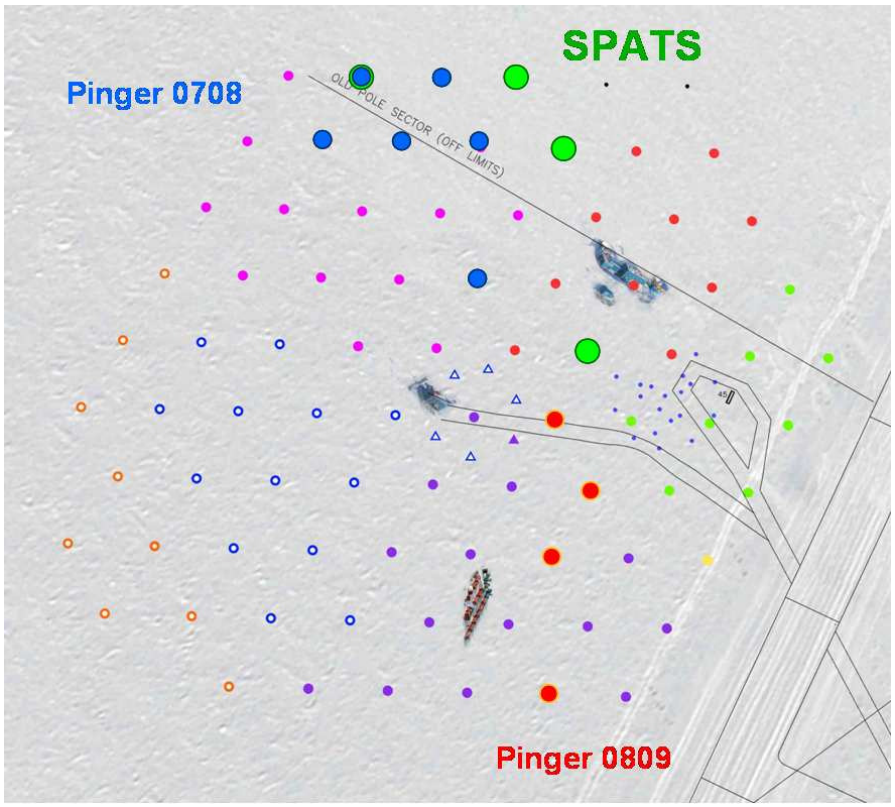


Figure 4.2: Aerial view of IceCube (holes are colored differently for different seasons), SPATS and the pinger holes.

is 5 mm long. The outer side of the ring, which is located outside the housing, contacts the ice; epoxy molding the ring guarantees isolation between the two electrodes. This kind of piezoelectric element was chosen because of a transmission response on the azimuthal angle more homogeneous than other prototypes tested [65]. The angular response on the polar angle presented however a variation of the pulse strength of about 200%. It cannot be excluded that during the freeze-in process the transmitters are tilted by forces exerted from the surrounding ice, so it is difficult to predict the emission pattern in the ice.

In each string, the six shallower transmitter housings contain also a *PT1000* sensor to measure the temperature; in the deepest stage a pressure sensor *CTE8060* by *SensorTechnics* is installed to monitor the depth of the string during deployment.

Each sensor module is composed of three cylindrical piezoelectric ceramics, of 10 mm diameter and 5 mm height, which are pressed against the pressure steel housing by a pre-load screw in a central post; a plastic ring helps hold the active elements in position during the mounting phase. The three piezoelectric ceramics are placed in the housing with a relative angle of 120 degrees to ensure a good

angular coverage. The three channels are numbered 0, 1, 2; we refer to a particular channel of a sensor adding the channel number to the sensor name (for example: BS6-2 is Channel 2 of sensor BS6).

One face of each PZT element touches the housing, which is the virtual ground; the other face contacts the input of a three-stage preamplifier chain. The pre-amplifier board has a pass-bandwidth filter between few kHz and about 100 kHz, with a central gain of $10^4$ in the region of 10 kHz. The last stage of the board converts the original analog signal into a differential one so that it can travel along the cables being less affected by eventual disturbances. A voltage regulator board, used to provide stable voltages needed for the power of the preamplifiers, is also located in the housing.

All 63 piezoelectric elements come from the same set of 100 ceramics for each of which the piezoelectric constant $d_{33}$ was measured. This constant measures the charge density developed [C/m$^2$] per given stress [N/m$^2$]. All of the examples chosen had a value of $d_{33} = 500 \pm 24$ [pC/N]. After being mounted, all the sensors were calibrated in a cold water tank with the reciprocity method [66] [67] using a calibrated hydrophone. For one of these sensors the angular dependence of the sensitivity was measured in water; from this measurement, it is known that the response as a function of the angle is quite complex, with variations up to 40% on the azimuthal angle and up to 200% on the polar angle [65].

Figure 4.3: View of an acoustic SPATS stage.

String D was improved in the design thanks to the knowledge gained after the analysis of the data collected with the first three strings. The high-voltage board used to pulse the transmitter was completely changed, in order to optimize the conversion from the absorbed electrical power and the high-voltage pulse discharged onto the piezoelectric load. One thicker ring-shaped piezoelectric ceramic, with an inner diameter of 20 mm, an outer diameter of 24 mm and a length of 15 mm, was installed at 250 m. No calibration was done for any transmitters.

The sensor design also changed: a detailed study of the pre-amplifier board was done with *P-SPICE* to optimize both the flatness of the gain in the bandwidth of interest and the noise at low temperature; this resulted in the change of some

(a) SPATS sensor II generation: picture.

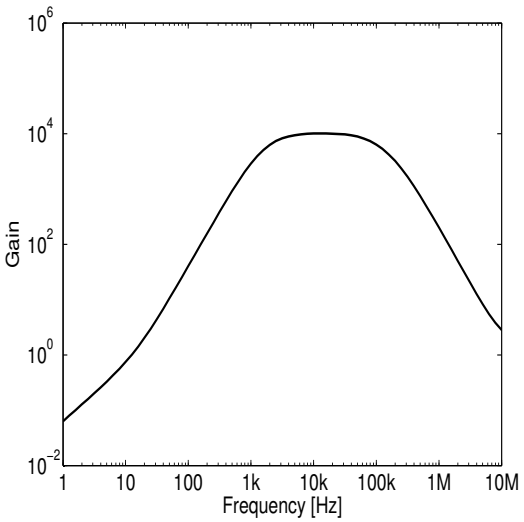


(b) SPATS sensor: gain vs. frequency.

Figure 4.4: SPATS sensor of II-generation and Bode diagram of the gain.

passive elements on the board. The Bode diagram of the gain obtained for the new sensor is shown in Figure 4.4(b). The central post and the plastic ring were abandoned in favor of a more stable mechanical mounting obtained by screwing the amplifier boards together with the piezoelectric ceramics on a steel ring pressed against the housing. A picture of an opened second generation SPATS sensor is shown in Figure 4.4(a). For none of the piezoelectric elements was the $d_{33}$ constant measured, since after the calibration of the previous sensors it became clear that the variation of the sensitivity over the angle, after mounting, counts more than the intrinsic sensitivity of the PZT element.

In addition to SPATS sensors, an alternative sensor design called "HADES" was installed at 190 m and 430 m depth [68]: this features a complementary dynamic range and a different matching of the impedance between the coating of the piezoelectric ceramic (polyurethane) and the ice.

All the modules were closed with O-rings with low internal pressure. Each component was designed to be fully operational at temperatures as low as $-60\,^{\circ}\mathrm{C}$ and was tested in a freezer before the deployment.

### 4.1.2 On-ice components

The string instrumentation is connected to a shielded multi-sheet copper cable assembly made of 14 separate cables. Each cable is four twisted-pairs with a global shield. At each instrumented depth, a breakout provides the connection of one of the 14 cables to one acoustic module, which is done via a 10-pin waterproof connector. The 14 cables are connected on the other side through as many connectors

to an aluminum box, called *Acoustic Junction Box* (AJB). The AJB contains a rugged embedded computer (*String PC*) which controls each of the seven transmitters and seven sensors deployed in the ice.

Beyond power and ground, which are common for both of the two module types, the other three twisted pairs are used differently for transmitters and sensors. In each transmitter two pairs are used for the steering voltage and for the trigger (which both modify the length and the height of the pulse transferred to the emitter); two pairs are dedicated to read back differentially the high-voltage pulse; two other pairs are devoted to the functioning of temperature or the pressure sensor. The shield of the cable is connected to the housing itself. As far as the sensor is concerned, the three twisted pairs are used to read out the differential signal of the three channels.

The AJB is located about 10 m away from the hole, and lies a couple of meters beneath the snow. Patch cables connect the acoustic system to the *IceCube Junction Box*; two previously unused quads in the IceCube cable are used to set a communication between the acoustic system and the *Master PC* which is located indoor in the ICL. A quad consists of two twisted pairs. Two pairs (one in each quad) are used to deliver power (96 $V_{DC}$) and GND. One other pair is used to provide the *Inter-Range Instrumentation Group* IRIG-B signal (see more details in the following section). The last pair is used as DSL communication line to transfer data and to control the String PC.

Each String PC is an assembled stack of three "fast" ADC/DAC, each featuring a nominal maximum sampling frequency of 1.25 MHz, a relay board with 16 relays able to switch the power on and off to each of the modules, and a "slow" ADC/DAC with a nominal maximum sampling frequency of 500 kHz. Each board has eight differential channels; seven of them are used to read out the differential output of the seven sensors, in the way that each of the three channels of a single sensor is read out by a different board, in order to make synchronization possible. Additional analog lines are used to fix the steering voltage; the digital output lines are used for the trigger signal. The slow board channels are used to read back the high-voltage pulse. The current from the pressure/temperature sensors is also read out by the fast ADCs.

### 4.1.3 Data acquisition

The String PCs and the Master run two different Linux distributions (RHEL ES rel. 3 on the Master PC and RedHat 7.3 on the String PCs). The software has been written on purpose entirely by the people involved in the construction of the project and in the analysis of the data. Each part has therefore been developed in strong connection with the operative goals and with a great knowledge of the hardware features and problems. The system presently coexists with unexpected limitation from the hardware: the ADC boards are indeed far from being used for long time at the nominal maximum sampling frequency due to a driver problem,

unresolved even by experts in the field. Nevertheless the maximum stable sampling frequency per channel is 200 kHz, which is enough to sample the acoustic signal. The waveforms recorded from each sensor are transferred as analog signals from the sensor to the String PC. Here they are digitized and get an absolute time-stamp, which is created using the IRIG-B signal. This is a time code which is generated by a GPS receiver located in the Master PC (Meinberg model *GPS169PCI*), using the GPS satellite time. The signal is distributed to the String PCs and is recorded synchronously with each sensor channel recording. The waveforms together with the information regarding their generation are stored as binary files in a RAM disk installed locally, and are next transferred to the Master PC. The Master PC, which provides the central control for the power, the communication, and the timing of the four strings governs the transfer of the data. Every day we can transfer up to 150 MB to a data-storage located in the Northern hemisphere, using satellite connection. In special occasion we can ask for a larger bandwidth; in other cases the excess of data is written to tape.

### 4.1.4 Performance

Every string was commissioned within 24 hours after deployment. The four strings are operational since the installation time, and the whole system has proved to be quite robust, standing also cold-rebooting after 48 hours due to sporadic power outages. Overall, 93% of sensor channels are healthy; the others are dead or in steady oscillation due to suspected lost ground contact. The number of working channels is 18 of 21 on String A, 21 of 21 on String B, 18 of 21 on String C, and 17 of 17 on String D. As far as the transmitters are concerned, the first generation ones seem to have changed behavior soon after deployment. The causes are still unknown, but the high-voltage recorded by an apposite circuit (see description in paragraph 4.2.2) shows unlikely pulse shape and amplitude. Nevertheless, the deficiency seems to be constant in time, therefore they can still be used as sound sources of unknown power. Second generation transmitters are instead working properly. For more details regarding the status of the transmitters, see [69].

Currently the South Pole Acoustic Test System is taking the following kinds of data:

- **Noise measurements**: the noise is measured for 0.1 s every hour by direct sampling at 200 kHz, for each channel in each sensor. In addition, since it has been demonstrated that the distribution of the noise samples has a Gaussian shape in amplitude, a histogram is calculated directly on the String PC at the South Pole; the bins of the fitting Gaussian are printed in a text file and transferred. A specific value of $\sigma_{noise}$ is measured for each of the channel, and results to be very stable in time after the complete freeze-in of the string.

- **Triggered events**: since August 2008, this is the job accomplished by the detector for most of the time (45 minutes per hour). Three channels at

three different depths (one in each of three sensor modules) in each string "listen" simultaneously. Until February 2009 the active channels were those installed between 190 m and 320 m, with the only exception of String B, where two channels of the same sensor (at 320 m) were taking data and none at 190 m. Since February 2009 the channels which are actively used in this data taking mode are those located in the four strings between 250 m and 400 m. If a sample passes a bipolar threshold of $\pm 5.2\sigma_{noise}$, a single-channel event consisting in samples preceding and following the triggering sample is recorded. The binary files containing the single-channel events are transferred to the Northern hemisphere. An off-line coincidence algorithm selects, from the four string data, those events which happen within the same 200 ms time-window (corresponding to the time needed for a sound wave to cross the whole array) and rejects noise hits. This procedure identifies clusters of events; another algorithm calculates the vertex of origin of the cluster. For more details see [69]. These data were also used for an attenuation analysis, which will be summarized in section 5.9.1.

- **Temperature and pressure monitor**: temperature in each module in the ice is monitored every hour.

In addition to the listed kinds of data, there are other types which are taken during special campaigns:

- **Intra-string runs**: each (or a selected) frozen-in transmitter is pulsed while the sensor in the same stage "listens". This kind of data was used to verify the conditions of the transmitters and sensors after deployment.

- **Inter-string runs**: each (or a selected) frozen-in transmitter is pulsed at high repetition rate (35-55 Hz) while the sensors distributed on all the strings "listen". The high repetition rate allows for the average of many different pulses, which improves the signal-to-noise ratio. The data collected were used to perform an independent attenuation analysis (see section 5.9.2).

- **Pinger data taking**: a special data taking scheme has been implemented to take data when the pinger (see below) is in operation. This was different in the two pinger seasons. More detail regarding this kind of data will be given in Chapter 5.

Every day two monitoring mails are sent to the acoustic group mailing list with the list of transferred files and additional information regarding the status of the system (disk space on all the PCs, temperature of the String PCs, speed of communication). Overall the system has been able to achieve good progress regarding the noise floor measurement [70], and the study of rate and nature of background transients [69]. To establish the sound speed profile and the attenuation length, the SPATS array was used in combination with the *pinger* which is described below. The sound speed profile measurement is presented in [13] and [69]. The attenuation length measurement is described here and in [71].

## 4.2 Pinger

The simplest way to measure the attenuation length is to record the signal emitted by one transmitter with a single sensor, and repeat the measurement a few times after moving one or the other to different distances. With the SPATS array, the method cannot be applied directly since all transmitters and sensors are frozen in the ice, therefore their location cannot be changed. In addition each sensor/transmitter has a different sensitivity/transmittivity, depending on both the azimuthal angle and the polar angle. Each module can rotate during the freeze-in of the hole, so nothing is known about the orientation of the sensors/transmitters after deployment. Nevertheless, the attenuation length of the acoustic signal can in principle be determined combining data from multiple transmitters and sensors and applying the "ratio method" [65]: however this method requires that the signal is visible on many more combinations than the ones recorded in the data taken during the first months of operation. For this reason, a retrievable transmitter to be used in multiple water-filled holes, prior to IceCube deployment, appeared to be a good solution both to calibrate the frozen sensors, using the same source, and to try an attenuation length measurement minimizing the systematic uncertainties.

The main requirements to be met were high portability, low power consumption, time synchronization with the SPATS array (*i.e.* with GPS time). Two options were available regarding the usage of cables and winches. One was to employ the winch TU-15 used for the SPATS deployment, with a suitable four twisted pair cable, 800 m long, custom produced by Ericcson. The second was to use the so called Robertson winch, already utilized at the South Pole for other "special devices" like the dust logger. At the beginning, the project was developed in order to be compatible with both the options, but in the end the Robertson winch was chosen. This mounts to a $\sim$2700 m, four-wire armored cable. The length of the cable and the number of wires available imposed a strong bound on the project development.

During 2008 such a pinger was designed and built. The system is an autonomous transportable device consisting of the stage itself (high-voltage pulser and emitter), to be lowered in water, and an on-ice box providing the power and the trigger signal, called *Acoustic Pinger Box* (APB). The two parts are connected through the cable which is spooled on the winch used to lower and raise the stage. In the next section a description of the system is given.

### 4.2.1 Design of the acoustic stage

The design of the high-voltage pulser was mainly done before the choice of an emitter; some adjustments were done afterward. The choice of the emitter followed a test phase of possible candidates. Below a description of the high-voltage pulser and of the candidate emitters and their tests are presented.

### 4.2.2 High-voltage pulser

The high-voltage pulser was designed modifying the schematic of second generation transmitters (the ones installed in String D). The main requirement was related to the number of wires connecting the stage to the surface through the Robertson winch. The four available wires were used to deliver power, ground, trigger and current readout from a pressure sensor installed in the stage to monitor the depth.

The schematic of the circuit is presented in Figure 4.5. A GPS receiver, connected to the APB on the surface, provides a *Pulse-Per-Second* (PPS) which is used to generate the trigger signal. To prevent losses along the multi-km cable, a current-driven signal is used rather than a voltage signal. How this is produced will be explained in the section concerning the APB. At the stage, the signal is regenerated by an optocouple (stage *U4* in the schematic) and feeds a monostable ($U7$) whose output goes high for a certain time $t_{high}$.

A steering current $i_{steer}$ is used together with the time $t_{high}$ to define the power of the pulse produced by the circuit. The current is generated from an "equivalent steering voltage" determined by a resistance partition on a fixed voltage, which can be changed by exchanging the resistors on the board. Therefore it is not a variable parameter once the stage is closed. We often refer to "equivalent steering voltage" since this is a parameter used to steer the power of SPATS transmitters.

When the output of the monostable goes in high state, $i_{steer}$ ramps up through *R4-R8* and *C15*, at the input of *U2* (pin 3). The op-amp stage *U2*, *T3* and *T2* act as a current source: *U2* drives the injection of current from *T2* into the base of the hybrid emitter bipolar transistor *T3*. This transistor is active only on trigger level *high* since its gate is connected to the monostable output.

When switched on, *T3* drives current through the 5.4 mH inductance *L1*. However, the current in the inductance cannot change suddenly, but takes about 2 ms to reach the maximum value. The passive network on the monostable output has been therefore designed so that $t_{high}$ is of the same order of magnitude; the actual duration of the time was measured in the laboratory to be $1.9 \pm 0.05$ ms, including in this error the dependence of the electronics on the temperature (between room temperature and water at about 0 °C).

In quiet conditions, with power on and no trigger signal, the point marked as *HV pulse* is connected to the power-net because in bias point analysis (at frequency $f = 0$) the inductance behaves as a short circuit. On the rising edge of the current step, due to the parasitic capacitance between gate and emitter of *T3*, the point suddenly experiences a small fall in voltage, which translates into a $\Delta V$ across the piezoelectric ceramic. This produces a small pre-pulse which is visible in the waveforms recorded (see for example Figure 5.9).

The power $W$ and the final energy $U$ accumulated by the inductance are:

$$W = VI = -L\frac{dI(t)}{dt}I(t) = -\frac{d}{dt}\left(\frac{1}{2}LI(t)^2\right) \tag{4.1}$$

$$U = \frac{1}{2}LI^2 \tag{4.2}$$

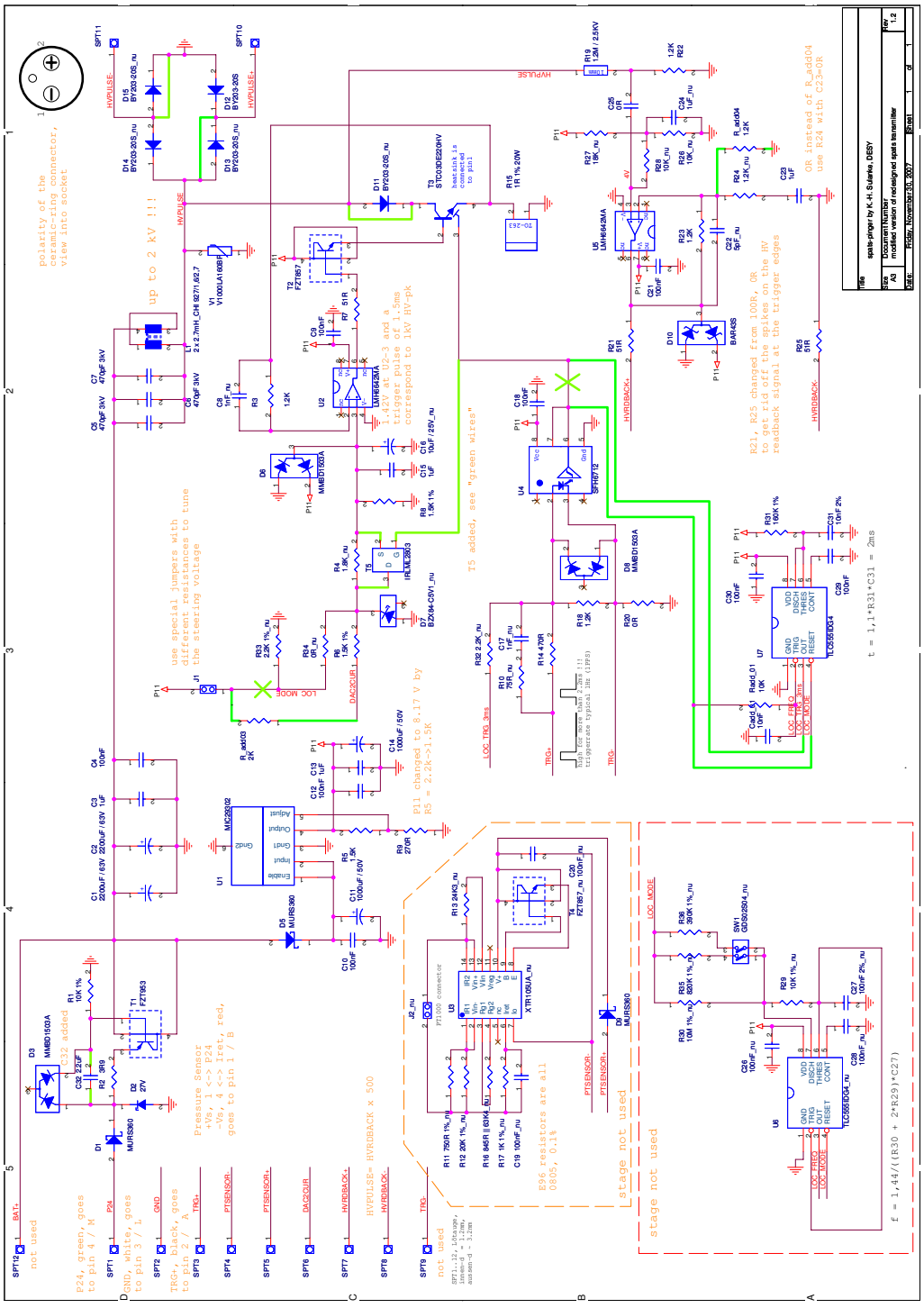

Figure 4.5: Schematic of the high-voltage pulser for the pinger.

where the minus indicates that the power is absorbed.

At the end of the time $t_{high}$ (*i. e.* on the falling edge of the trigger signal), the voltage at *HV pulse* undergoes a strong bipolar spike in voltage. The negative part of the pulse is suppressed by the diodes *D14* and *D12*. The *HV pulse* terminal is connected to the piezoelectric element to which the accumulated energy is transferred:

$$U = \frac{1}{2}CV^2. \tag{4.3}$$

Taking into account the small capacitors *C5*, *C6*, *C7* which are in parallel with the piezoelectric element and the capacitance of this, the voltage across the load is:

$$V = \sqrt{\frac{L}{C_{piezo} + C_5 + C_6 + C_7}}I. \tag{4.4}$$

The piezoelectric ceramic therefore experiences a difference in voltage inversely proportional to the square root of its own capacitance. The high-voltage pulse can be sampled on the board thanks to a circuitry (*U5*) which acts as a divider (by a factor 500) and transforms the signal in a differential one. This is called "high-voltage read-back" signal. The dynamic of the pulse can be seen looking at the high-voltage read-back plot shown in Figure 4.12 at the end of the section.

The generated electric field $E$ develops into strain $S$ according to the value of the strain-coefficient $d_{ij}$ (ratio between strain developed in the direction of the axis $i$ [m/m] per electric field applied on the axis $j$ [V/m]):

$$S = d_{33} \cdot E \tag{4.5}$$

$$E = V/d \tag{4.6}$$

$$V = Q/C_{piezo} \tag{4.7}$$

where $(i, j) = (33)$ indicates the direction perpendicular to the piezoelectric ceramic surface and $d$ is the thickness of the piezoelectric ceramic. From the previous equations $S$ can be re-written as:

$$S = d_{33}\frac{Q}{d\ C_{piezo}}. \tag{4.8}$$

The previous equations provide the relation between the geometrical, electrical and material properties of the piezoelectric ceramic, the voltage applied and the strain produced.

During operation, the high-voltage pulser is located in a steel housing 15 cm long and 10 cm wide. The connection to the piezoelectric ceramic, which is outside the housing, is realized by a *Subconn* waterproof connector; the stage is closed under vacuum conditions of about 0.3 atm using a proper *O-ring* and a cap with penetrator which fits the cable installed on the Robertson winch. This was installed and only used at the Pole. During the test phase, another cap equipped with a connector analogous to a SPATS transmitter was used. A complete set of adapters was developed to be used both at the South Pole and in the preparation phase in the Northern hemisphere.

### 4.2.3 Emitter choice

(a) SPATS emitter (b) SQ09 (c) ITC-1001

Figure 4.6: Candidate emitters: SPATS-like emitter, SQ09 by *Sensor Technology* and ITC-1001 by *ITC-transducers*.

The emitter was chosen after the test of several candidates. Naturally the first was the same ring-shaped piezoelectric ceramic which is used in SPATS transmitters. Additional available candidates were the commercial SQ09 by *Sensor Technology*, used for lab tests, and the ITC-1001 by *International Transducer Corporation*. A picture of each emitter is shown in Figure 4.6.

- The **SPATS emitter** is, as already said, a ring-shaped piezoelectric ceramic with inner diameter equal to 18 mm, outer diameter equal to 20 mm, and length of 5 mm. The material, whose name is $PIC151$, is a modified lead zirconate/lead titanate piezoelectric ceramic with high permittivity, high coupling factor and high piezoelectric charge constant. The capacitance is about 6 nF. The transmittivity was proved to be quite isotropic on the azimuthal plane, with a spectrum predominantly peaked between 10 and 60 kHz [65]. SPATS emitters survived a pressure of at least 120 bar in tests.

- The **SQ09** is a commercial multi-purpose transducer produced by *Sensor Technology*. The shape is cylindrical, with a diameter of 50.8 mm and a length of 63.5 mm. Interesting features of this transducer are the possibility to be used in water down to 2500 m depth and the maximum drive voltage which is 1000 V. The frequency response is specified by the company to be flat between 3 Hz to 20 kHz, with a resonance frequency at 24 kHz. The so called *Transmitting Voltage Response* will be shown in Chapter 6 in Figure 6.4. The nominal capacitance is 10 nF at 20 °C; the company specifies a decrease of 0.33% per Celsius degree increase; in addition, a 7% loss is expected at 1000 m depth.

- The **ITC-1001** by *International Transducer Corporation* is a transducer made of two hemispheres in high precision Channelite-5400 lead zirconate titanate ceramic. The spherical beam is very isotropic in emission both on the polar and the azimuthal plane. The corresponding *Transmitting Voltage*

*Response* will be shown in Chapter 5, see Figure 5.32(a). The specified working depth reaches 1250 m. The bandwidth is between 10 Hz - 25 kHz, with a resonance frequency at 16.5 kHz; the transmittivity at the resonant frequency is 149 dB/$\mu$Pa/V at 1 m distance.

It should be noticed that for our measurements, we do not need to choose an emitter whose emission profile is similar to the expected profile emission of the cascade. An emitter with a spherical beam gives the advantage of an isotropic emission, and it is a reasonable choice in our case.

### Laboratory test

During the test of the different piezoelectric ceramics, an intermediate value for the steering voltage was chosen, somewhat arbitrarily. This was done since the specifications of the companies on each transducer are expressed in very different terms (maximum input power, maximum voltage, maximum electric field) which it is not easy to translate for the specific short pulse generated by the high-voltage pulser. The different ceramics could in principle be represented with different equivalent electronic circuits, but these are difficult to determine and to compare.

In addition, two aspects must be considered: on the one side, the amplitude of the high-voltage pulse depends on the load and not only on the steering voltage; on the other side the amount of sound which is produced depends on the characteristics of the piezoelectric ceramic, and not only on the amplitude of the pulse. Thus the relation between amplitude of the electrical pulse and sound produced is not a linear one.

It is appropriate also to underline here that our requirements were not to build the most powerful pinger possible, but one suitable to be used with SPATS at the South Pole. In particular the specification was to fit in the dynamical range of our sensors in a way that they would not be saturated at near distances and could still hear a signal above noise at larger distances. In order to predict the suitable signal power it was necessary to take into account the transmission coefficient from water to ice and the propagation at the distances foreseen to be between pinger and SPATS array. As a consequence, the attempt was to select the most versatile piezoelectric ceramic, which was performing better with the developed high-voltage pulser. Some variation of the setup could have been done after the first pinger run, by opening the stage and increasing or decreasing the equivalent "steering voltage" with the exchange of one resistor on the board.

The first test was done in air: each piezoelectric ceramic was set at a fixed distance (50 cm) from the same sensor and the recorded sound was compared. The sensor chosen was the *iron ball*, of which information is found in [65].

Each emitter was connected to the high-voltage pulser. This was attached to the Acoustic Pinger Box (see below) using a 400 m cable to simulate a more similar cable to the one to be used.

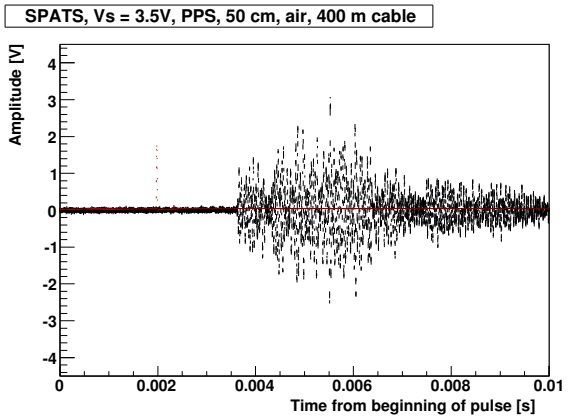


(a) SPATS emitter

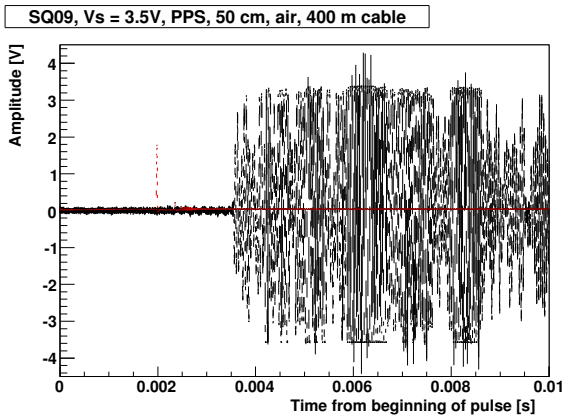


(b) SQ09 emitter

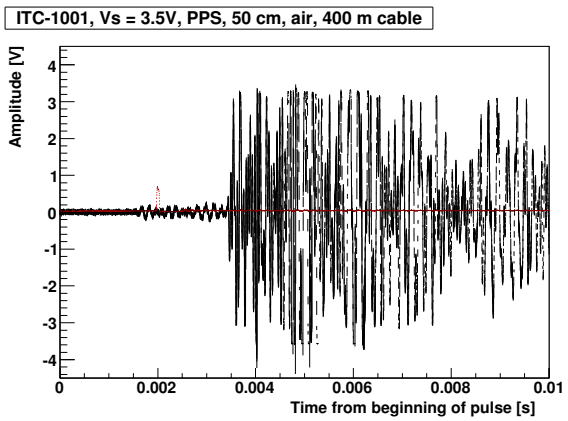


(c) ITC-1001 emitter

Figure 4.7: Test of the emitters at a short distance (about 50 cm) in the laboratory with low steering voltage. The red line is the high-voltage read-back signal.

To compare safely the SQ09, the ITC-1001 and the SPATS transmitter a common intermediate value of the "steering voltage" was chosen. The waveforms sensed by the *iron ball* are shown in Figure 4.7.

The data was read out with the data-acquisition card *NiDAQ-PAD 6070E* produced by *National Instruments*, connected to a laptop to monitor the signal on-line. For each emitter the high-voltage read-back from the pulser board was sampled together with the recorded signal from the sensor. Ten events sampled for 200 ms at a frequency of 500 kHz were recorded and then averaged together. In the figure, the signal is visible in black, while the high-voltage read-back appears in red. The delay of the signal corresponds to the time of propagation of the signal in air from the emission time. It is clear that in spite of a smaller high-voltage pulse, the sound emitted by the ITC-1001 is the strongest.

### Lake test


Figure 4.8: Aerial map of the location where the lake test took place (from GoogleMaps).

In order to verify the performance of the emitters over a long range, a test was done in the nearest available big volume of water: the lake of Zeuthen. A map of the location can be found in Figure 4.8.

The high-voltage pulser, this time connected to a shorter cable, equivalent to 30 m, was hanging from the tip of a canoe, inside which the Acoustic Pinger Box was placed. The canoe was moving in the lake, "stopping" when the measurement was done. Next, the canoe was driven back, the emitter was changed and the test was repeated.

The data collection was done from the shore, where the *iron ball* sensor was hanging from the wharf in front of the DESY institute. Power was provided by standard laboratory power supplies moved to the wharf; the data was read out by the *NiDAQ-PAD6070E* and a laptop. Both the emission and the data taking were triggered by the GPS signal, received both by the pinger and on the shore with two different systems. A picture of the setup is shown in Figure 4.9.

Figure 4.9: Lake test: picture of the setup for the data taking on shore.

Data were collected for different distances from a few hundred meters up to about 1 km. At these distances it is difficult to compare the strength of the signal due to the short duration of the pulse and the high noise level related to the transit of boats and ducks and many other transients events. Also, since the canoe was drifting, it is not easy to collect and average many events. Nevertheless, if the recording time is kept long, it is in principle possible to locate the pulse, as the only sound repeating at the same delay from the beginning of the second (coincident with the pulse emission within a few milliseconds). This was successful for the ITC-1001 and the SQ09, which were confirmed as the most powerful emitters. The waveform recorded for the SQ09 is shown in slices of one second in Figure 4.10. From the delay of the

pulse compared to the start of the second it is possible to reconstruct the distance of the canoe. A test from a larger distance was done hanging the ITC-1001 from the location marked with a $X$ on the map of Figure 4.8, where a boat wharf is available. The waveform recorded in this configuration is shown in Figure 4.11.

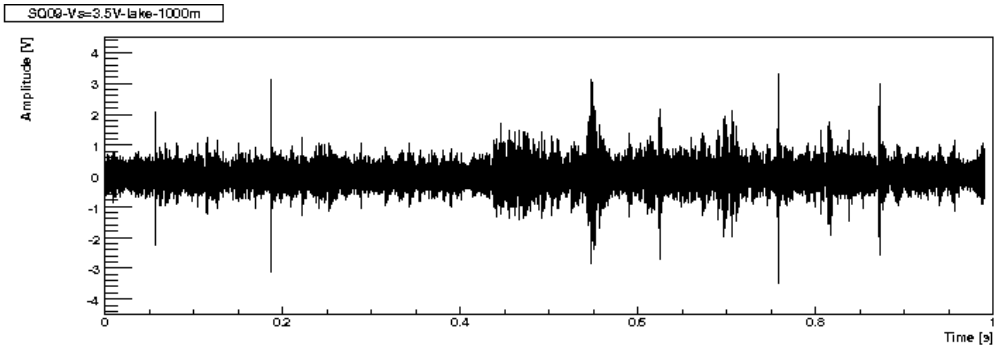


(a)

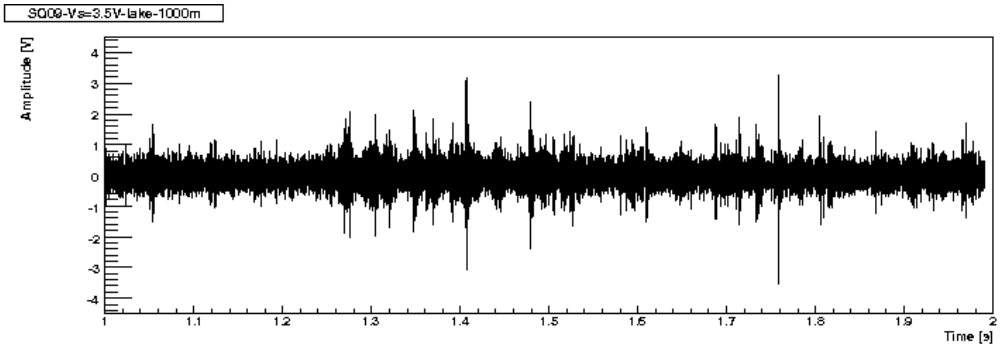


(b)

Figure 4.10: Test of the SQ09 in the lake at about 1.0 km distance. The signal is visible as pulse at about 0.765 s in (a) and 1.765 s in (b).

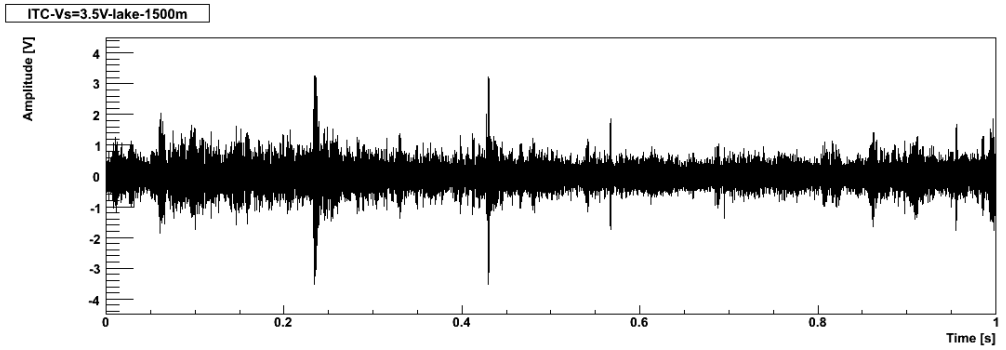


(a)

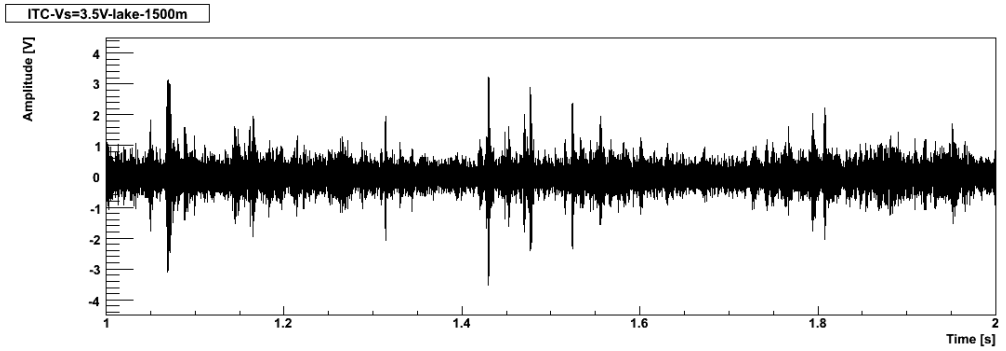


(b)

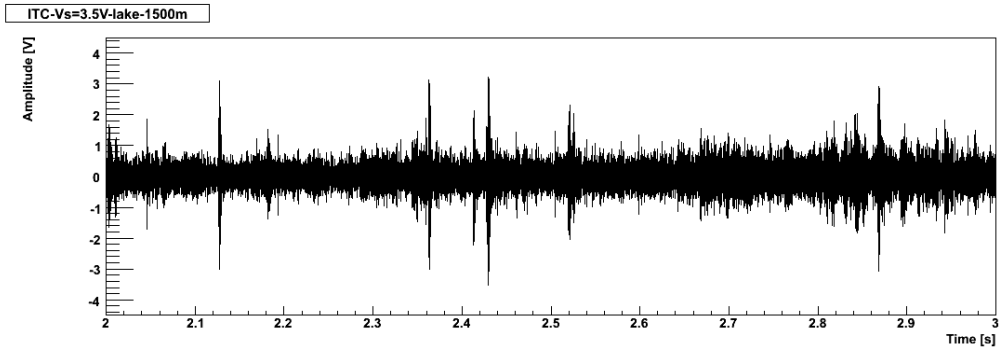


(c)

Figure 4.11: Test of the ITC-1001 in the lake at about 1.5 km distance. The signal is visible as pulse at about 0.43 s (a), 1.43 s in (b) and 2.43 s in (c).

### The final pinger acoustic stage

At the final development step, the acoustic stage consisted of the high-voltage pulser, inserted in its steel housing, with the emitter ITC-1001 attached through a 2 m long cable.

Two distinct emitters of the same model were used in the two pinger operating seasons. For the one used in the first season, the resonance frequency was measured to be $f_{res} = 17.680$ kHz. The impedance value at this frequency was $C_{res} = 58$ nF, $Z_{res} = 1.7$ Ohm. For the one used in the second season, the resonance frequency was measured to be $f_{res} = 17.710$ kHz; the impedance value was found to be $C_{res} = 60$ nF with $Z_{res} = 6.2$ Ohm. Both measurements revealed a resonance frequency slightly higher than that specified by the company.

Using equation 4.4 the resulting voltage across the piezoelectric load is:

$$< V >= \sqrt{\frac{L}{C_{piezo} + C_5 + C_6 + C_7}}\, I \sim 300\ V. \tag{4.9}$$

Of course this value must be taken as a rough calculation given the simplicity of the model used; however it turns out to be quite near to reality. A picture of the high-voltage read-back with the selected load can be found in Figure 4.12. The two plots in the Figure show the pulse on two different scales, on a time axis which starts at the beginning of the rising edge of the trigger pulse $t_{high}$: the small fall in voltage at $t = 0$ is hardly visible (since a DC/AC filter is present between the pulse and the high-voltage read-back). The falling edge of $t_{high}$ coincides with the pulse. It is visible that the piezoelectric ceramic is brought to oscillation and rings for some time after the main pulse. The real electrical pulse exciting the load is about 300 V high and 30 $\mu$s long. Due to the shortness of the exciting pulse, the signal emitted by the piezoelectric ceramic is broadband, with a predominance in the 10-30 kHz range as specified by the *Transmitting Voltage Response* provided by the company as calibration data.

## 4.2.4 Acoustic Pinger Box

The box has a weight of about 10 kg and contains a 24 V sealed lead acid rechargeable battery pack (by *Hawker-Cyclon*) specified to work at temperatures as low as $-65\,^{\circ}$C.

A GPS clock (model GPS 18 LVC by *Garmin*), is used to generate a PPS signal in TTL logic with 10% duty cycle. In the first pinger season, the GPS receiver was directly connected to the APB, and the PPS itself was used as trigger signal at 1 Hz. In the second pinger season, a frequency multiplier device (see details in the following section) was added between the *Garmin* GPS and the APB to multiply the trigger signal in frequency from 1 Hz to higher frequency (up to 40 Hz), keeping synchronization with the GPS time. Actually during the operations a trigger rate not higher than 10 Hz was used. Some details about this addition will be explained in section 4.2.5. The TTL trigger pulse is converted

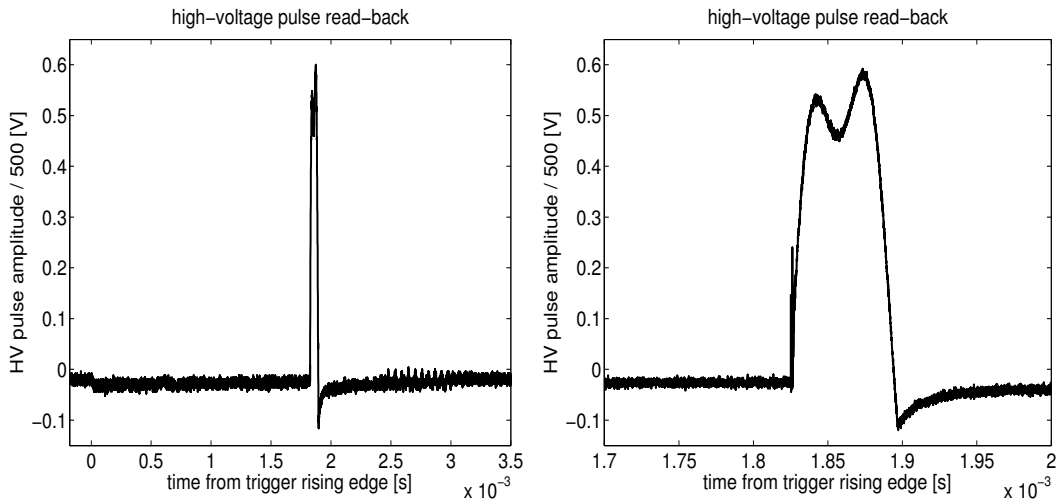


(a) (b)

Figure 4.12: High-voltage pulse recorded through the high-voltage pulse read-back circuit for the pinger in the final configuration with the ITC-1001 as emitter on two different time-scales.

into a current signal by a circuit, located in the APB (marked as *Q2-Q3* in the schematic of Figure 4.13) and it is next driven though the cable to the HV pulser.

Other circuitry present in the Acoustic Pinger Box includes DC/DC converters to provide stable voltages for powering the stage and the GPS receiver. In the original design also an external display was foreseen to read out the current from the pressure sensor installed in the acoustic stage.

### 4.2.5 Improvements between the seasons 2007-2008 and 2008-2009

The pinger used in the season 2007-2008 is shown in Figure 4.14. With the experience gained after the first year of operation, the pinger was upgraded for the following season. The improvements are presented below.

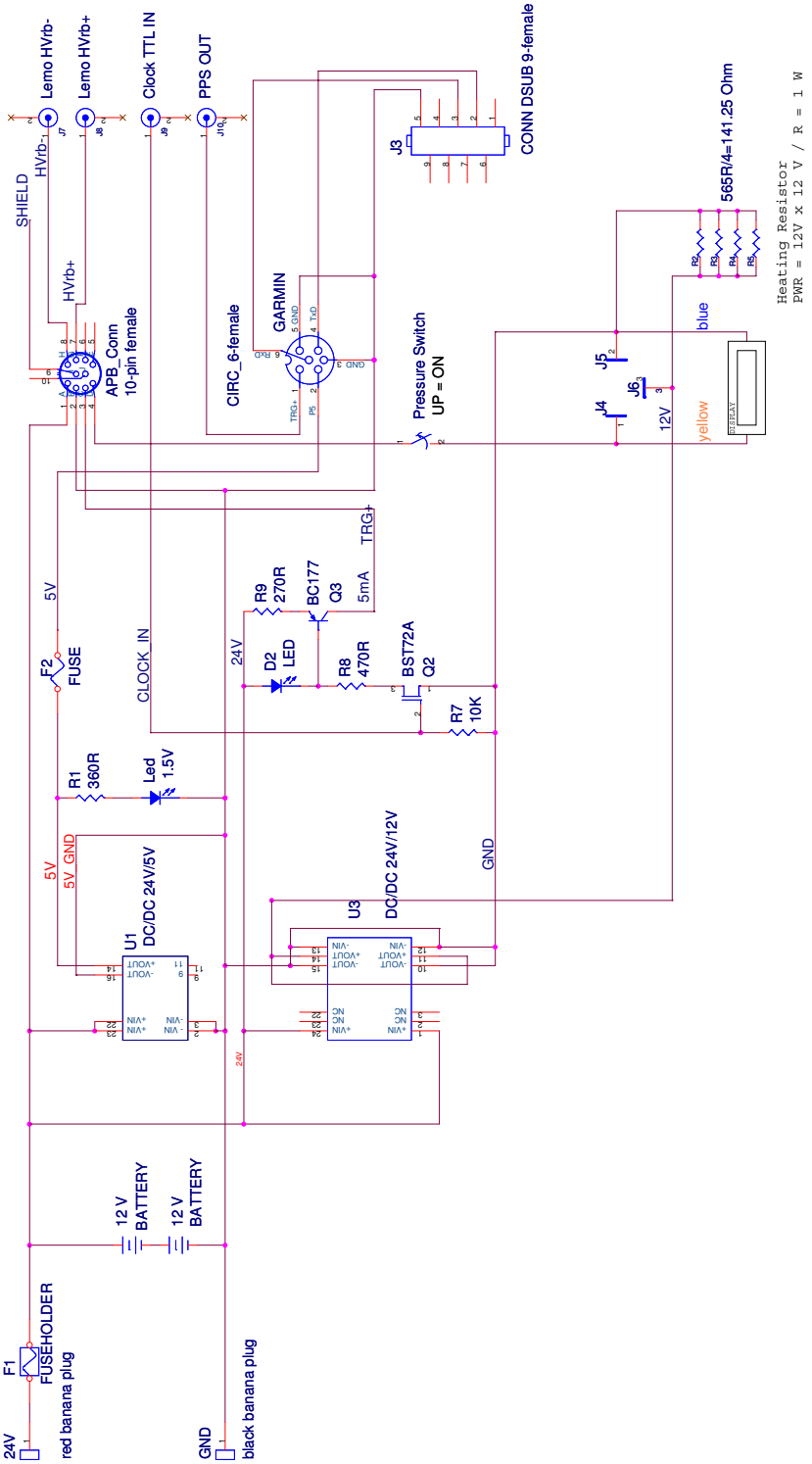


Figure 4.13: Schematic of the Acoustic Pinger Box.

(a)

(b)

Figure 4.14: Pinger operating in the austral summer season 2007-2008, during preparation in the laboratory (a) and while lowered into an IceCube hole (b).

### 1. Centralizers

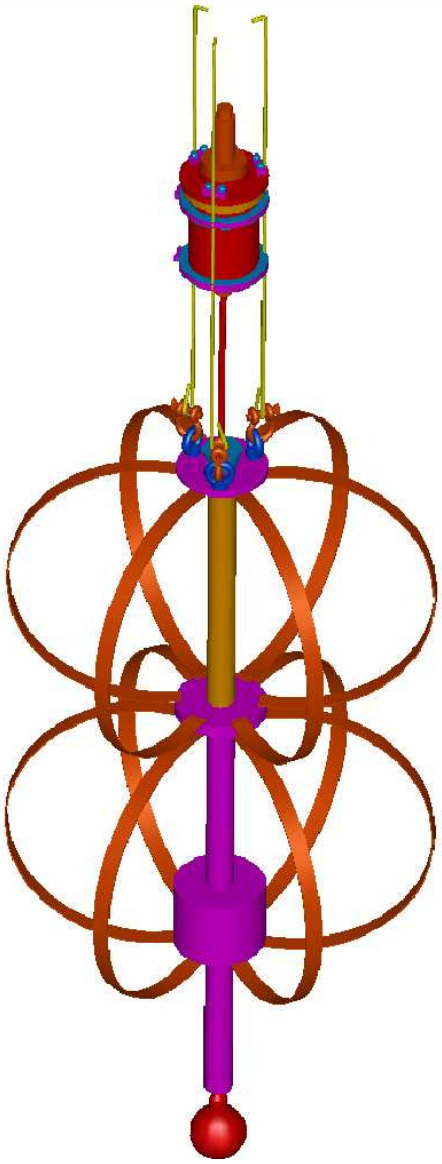

Figure 4.15: Mechanical drawing of the pinger with "centralizers".

One of the most serious problems which became clear analyzing the data collected during the first season was the fact that the pinger was free to swing and to assume any position in the hole. This resulted in the waveforms being unstable in shape from stop level to stop level and from hole to hole, and made difficult the use of the data for an attenuation length analysis. More details about these problematic effects are discussed in Chapter 5.

In preparation for the second season, the mechanical construction of the acoustic stage was partially changed: a centralizer system, made of two spherical sections, was added between the high-voltage pulser and the emitter, in order to keep the ITC-1001 at the center of the hole in a fixed position and to prevent the whole system from swinging. The technical drawing illustrating the modified acoustic stage is shown in Figure 4.15. Each of the two centralizing structures has a maximum width of about 600 mm and a length of about 400 mm. The material used for the ribs (708.5 mm long, 25 mm wide and 1 mm thick) is phosphorous bronze; to prevent any electro-chemical reaction with the almost ions-free water, the flexible structures were encapsulated in plastic envelopes.

The distance of the emitter from the HV module was also decreased from about 1.7 m to 1.45 m, suitable to get a sufficient distance from the centralizer and avoid reflections from them. A long stiff pipe in stainless steel, divided in two parts, holds the emitter and serves as support for the mounting of the centralizers; it terminates in a steel weight of 1 kg. The whole stage has a weight of about 20 kg.

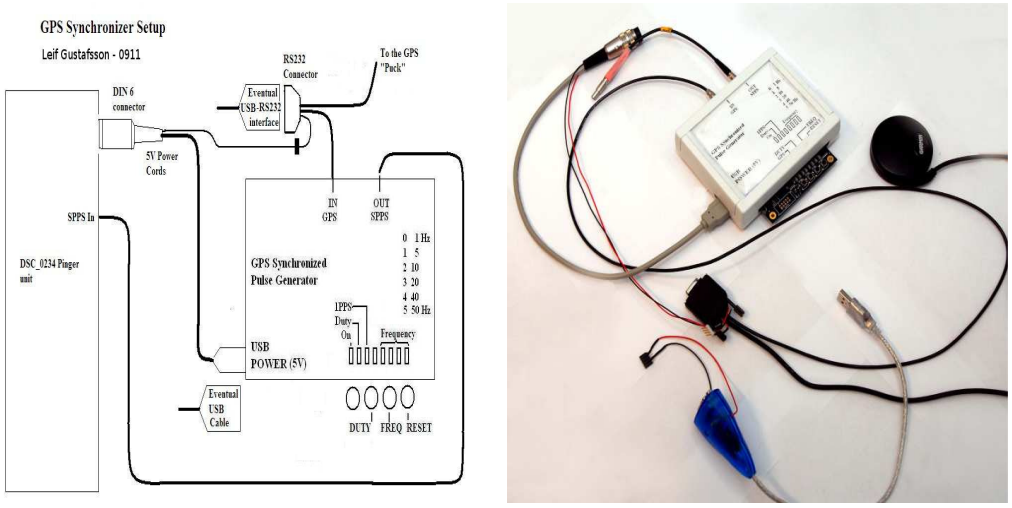


(a) (b)

Figure 4.16: GPS synchronizer: scheme of principle in (a) and picture in (b).

### 2. Frequency multiplier

A frequency multiplier, called also GPS synchronizer, designed by L. Gustaffson and P. Marciniewski from Uppsala University, was added between the GPS system and the trigger input of the Acoustic Pinger Box. This stage and the scheme are pictured in Figure 4.16. The GPS synchronizer contains an oscillator (running at 50 MHz with a frequency stability of $\pm 50$ ppm) and a Complex Programmable Logic Device (CPLD); the input used is the Pulse-Per-Second which is provided by the GPS receiver. The CPLD is programmed so that the number of oscillations of the oscillator are counted from the beginning of the PPS, and a synchronized train of rectangular pulses equi-spaced in time is produced as output. This train of pulses, in TTL logic, is used as input clock of the APB to trigger the sound emission of the pinger (as described in the section 4.2.2). The frequency of the train of pulses can be chosen within a set of possible values using a switch. The CPLD can be also re-programmed to provide a different set of values.

One of the problems of any frequency-multiplication device is that the internal oscillator used to generate the clock is affected by drift and jitter. Both these effects lower, more or less significantly, the time precision of the generated train and consequently the time precision of the acoustic pulses emitted by the pinger. To measure the effect over the interesting time duration (*e.g.* a time similar to the one in which data are taken), it is important to rely on the correct emission time of each pulse (for example, in order to compute correctly the average of the pulses). The accuracy of the division for a generated 10 Hz train was measured in the laboratory by observing the drift over a 18 s time intervals, which corresponds to the time used to record data for a single sensor channel during the operations at the South Pole (see more details in Chapter 5, section 5.2.2). Figure 4.17 shows

the result of the measurement: each of the 10 pulses present in 1 second is colored differently, and it is plotted in the time scale of the GPS-PPS signal to verify the jitter or delay. This is repeated for all the 18 s, so that the total number of pulses shown is 180. The diagram shows that all the pulses appear with a constant offset (about 10 $\mu$s after the PPS start), within $\pm 5$ $\mu$s. This is the total drift, visible as spread of the pulses; over the time of interest this value is stable. No jitter, which would appear as pulses of different color exchanging appearance order randomly, is visible within the precision of the measurement.

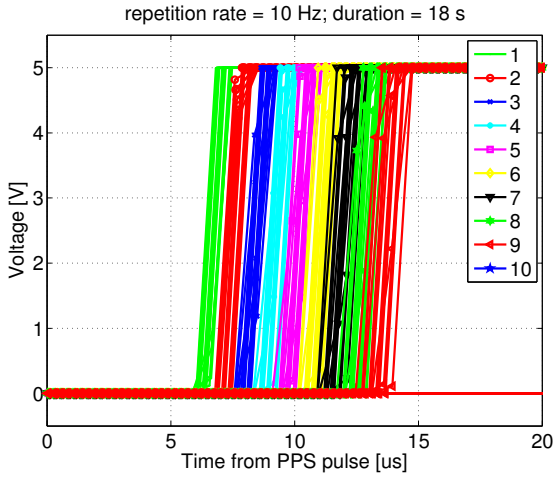


Figure 4.17: Drift of the pulses in the frequency multiplier stage operating at 10 Hz. All the 10 pulses of each of the 18 seconds (as long as the time used to record each waveform) are wrapped over 100 ms and stacked. Each pulse $i$ ($i$ =1..10) in the train of 10 is colored according to the legend. The diagram shows that all the pulses appear with a constant offset (about 10 $\mu$s after the PPS start), within $\pm 5$ $\mu$s.

### 3. Data acquisition

In preparation for the data taking during the second season, the data acquisition system of SPATS was also upgraded. In the first season channels in the same sensor were taking data one at a time only for 9 seconds, and only one sensor at a time was active. The data taking between different strings was started manually and was completely asynchronous. For the second season, we achieved the simultaneous recording of the three channels of the same sensors, and we increased the recording time to 18 seconds. In addition, the data were taken synchronously between the four strings, so that sensors at the same depth were recording at the same time. More details about the data taking will be described in the following chapter, since they are specifically connected to the analysis.

The pinger in the improved version is shown, hanging in the ICL in Figure 4.18.

Figure 4.18: Improved version of the pinger in the IceCube Laboratory soon before the deployment in the season 2008-2009.

# Chapter 5

# Pinger data analysis

The pinger was used in two austral summer seasons: 2007-2008 and 2008-2009. The data collected during the first season were found to be affected by many unforeseen effects, in such a way that the recorded waveforms were so unstable in amplitude that they could not be used to measure the attenuation length. The study of these data allowed for a better understanding of the systematics related to the pinger operation. In the following sections, a detailed discussion about the data and the relevant systematic effects will be presented.

In the second season the pinger was improved as described in section 4.2.5 and was then run again in IceCube holes. The modifications implemented in the hardware (electronics and mechanics) resulted in a high stability of the waveforms and in an overall improvement of the signal-to-noise ratio, and allowed for the measurement of the acoustic attenuation length. The analysis of this data and the results will be presented below.

## 5.1 Pinger data from 2007-2008

### 5.1.1 Geometry

In the austral season 2007-2008 the pinger was run in IceCube Holes 55, 70, 71, 77, 76, 69 (see map in Figure 5.1). The distance from the SPATS strings ranged from 125 m to 330 m. The azimuthal range was quite large, reaching a maximum value of 90 degrees (angle between Hole 55 and Hole 77 as seen from String B); the most aligned combination was given by the three Holes 69, 70, 71, for which the angle seen by B was less than 1 degree while the one seen by A was 41 degrees. Also Holes 76 and 77 were aligned in direction of String A. Only one of the Holes (69) followed the deployment and the complete freezing of String D (in Hole 76). A list of all the distances is presented in Table 5.1.

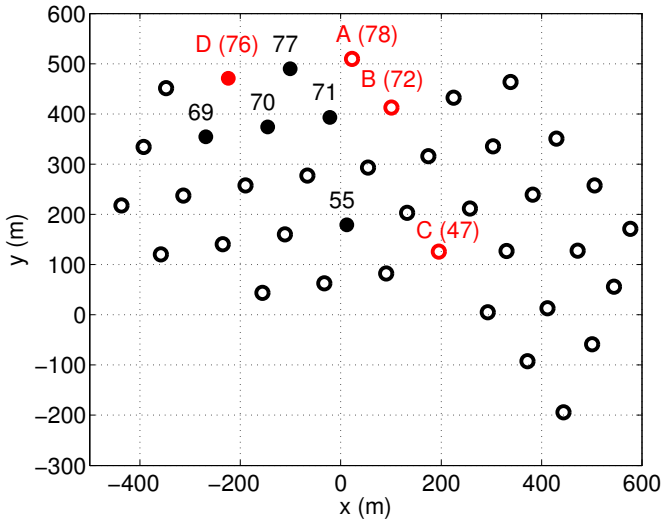


Figure 5.1: Geometry of IceCube-40 with the SPATS array (in red, labeled with letters and numbers) and the holes in which the pinger was run in the season 2007-2008 (filled circles, labeled with numbers).

| Pinger Hole | A | B | C | D |
|---|---|---|---|---|
| 55 | 330.5 m | 250.0 m | 190.8 m | - |
| 70 | 215.3 m | 249.5 m | 421.6 m | - |
| 71 | 124.3 m | 124.5 m | 344.6 m | - |
| 77 | 124.7 m | 216.4 m | 469.7 m | - |
| 76 | 249.2 m | 330.3 m | 543.0 m | - |
| 69 | 329.8 m | 374.5 m | 517.2 m | 124.9 m |

Table 5.1: Distances between the SPATS array and the pinger holes in 2007-2008.

### 5.1.2 Data acquisition

In the first pinger season all the instrumented depths were investigated. Therefore the pinger was lowered down and stopped at 80, 100, 140, 190, 250, 320, 400, 500 m and then it was raised up. The three channels of all the sensors present in each string were recording one at a time for 9 seconds each. The pinger was pulsed at 1 Hz repetition rate, so 9 pulses were recorded in each waveform.

The script looped continuously over the channels and sensors, in each string independently. To complete a "recording loop" at one stop-level over all the seven sensors (*i.e.* taking data with the 3×7 channels in sequence) took a time of about 4 minutes. A time of 4-5 minutes was therefore established to be the minimum stopping time of the pinger at each selected depth, in order to get at least a waveform recorded for each channel during the stop of the pinger at each level.

### 5.1.3 Data quality: expected signal

In the most naive model, if the sensors had a flat response, not dependent on the polar angle, the signal amplitude received by a certain channel would be a smooth function of the pinger depth, with a maximum corresponding to the minimum distance between source and sensor. This condition would be verified when the emitter is located at the same depth as the sensor. The expected signal can be deduced in first approximation using a simple model, taking into account the geometry, the Snell law and the transmission coefficient, angle dependent, between water and ice.

When an acoustic wave propagating in a medium crosses a discontinuity (in our case, the interface water-ice at the edge of the hole's wall), it is partially reflected and partially transmitted. The reflection coefficient is [65]:

$$R = \frac{Z_{ice}\cos(\theta_{ice}) - Z_{water}\cos(\theta_{water})}{Z_{ice}\cos(\theta_{ice}) + Z_{water}\cos(\theta_{water})} \tag{5.1}$$

In the formula above,

- $\theta_{water}$ and $\theta_{ice}$ are the incident and transmission angle, which are related to the sound speed $v$ in the media by the Snell law:

$$\frac{\sin(\theta_{water})}{v_{water}} = \frac{\sin(\theta_{ice})}{v_{ice}} \tag{5.2}$$

  $\theta_{water}$ has values from 0 to 21.3 degrees, the angle at which the phenomenon of *Total Internal Reflection* (*TIR*) happens.

- $Z_{ice}$ and $Z_{water}$ are the acoustic impedances of the media, which are defined as the product of the density $\rho$ and the sound speed $v$ in the medium:

$$Z = \rho \cdot v \tag{5.3}$$

The sound speed in water and ice are known:

$$\begin{aligned} v_{water} &= 1.48 \cdot 10^3 \text{ m/s}; \\ v_{ice} &= 3.85 \cdot 10^3 \text{ m/s}; \end{aligned} \tag{5.4}$$

as well as their densities at about 0 °C:

$$\begin{aligned} \rho_{water} &= 998 \text{ kg/m}^3; \\ \rho_{ice} &= 917 \text{ kg/m}^3; \end{aligned} \tag{5.5}$$

therefore the acoustic impedances can be calculated:

$$\begin{aligned} Z_{water} &= 1.48 \cdot 10^6 \text{ kg s}^{-1} \text{ m}^{-2} \\ Z_{ice} &= 3.53 \cdot 10^6 \text{ kg s}^{-1} \text{ m}^{-2} \end{aligned} \tag{5.6}$$

The transmission angle is in our case the angle at which the sensor is seen by the pinger with respect to the pinger equatorial plane. If the horizontal distance between sensor-string and pinger-hole is $d_{hor}$ and $r$ is the distance between pinger and sensor, the angle between pinger and sensor plane is:

$$\theta_{ice} = \cos^{-1}\left(\frac{d_{hor}}{r}\right) \tag{5.7}$$

from which the incident angle in water $\theta_{water}$ can be calculated by using equation 5.2. Once the media are defined, the coefficient $R$ is determined completely by the relative position of pinger, sensor, described by $d_{hor}$ and $r$.

The transmission coefficient is calculated from $R$ as:

$$T(d_{hor}, r) \;=\; 1 - R(d_{hor}, r) \tag{5.8}$$

The amplitude of the transmitted waveform will be described at the interface by the equation:

$$A_T \;\propto\; T(d_{hor}, r) \cdot A_I \tag{5.9}$$

where $A_I$ is the amplitude of the incident wave. In the approximation of spherical emission, the pressure wave amplitude will geometrically scale with the source-sensor distance $r$, and will decay exponentially depending on the acoustic attenuation length $\lambda$ in the medium. The acoustic pulse amplitude at $r$ will therefore be, in the far field:

$$A_T(r) \;\propto\; T(d_{hor}, r) \cdot \frac{A_I}{r} e^{-r/\lambda}. \tag{5.10}$$

If $\lambda \gg r$ the exponential factor can be neglected and the equation above is completely defined given a particular combination of $d_{hor}$ and $r$: the only unknown parameter, $A_I$, is a constant (in the case of an isotropic source). If we want to study the variation of the signal as a function of the pinger depth $z_{pinger}$, we can express $r$ as:

$$r = \sqrt{d_{hor}^2 + (z_{pinger} - z_{sensor})^2} \tag{5.11}$$

where $z_{sensor}$ is the depth of the sensor. In Figure 5.2(a) the curve represented by equation 5.10 is calculated (besides the normalization depending on $A_I$) for an example combination sensor-hole, with a distance of about 250 m and a sensor depth of 320 m, in a range of depths for the pinger between 80 and 500 m.

The equations above have been obtained making several approximations: we have assumed a two-dimensional geometry, an homogeneous interface and a simple propagation model, and we have not considered any contribution of shear waves. These aspects, initially believed to be secondary, resulted in being dominant as will be described in the following sections.

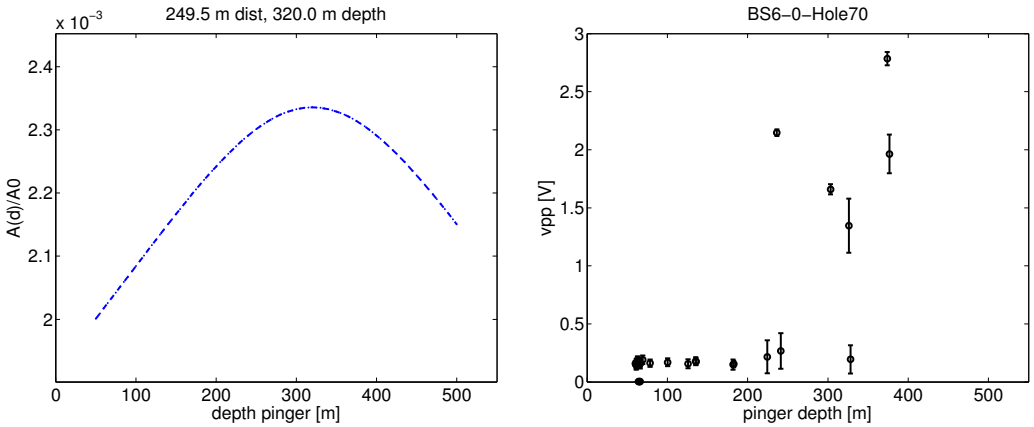


(a) (b)

Figure 5.2: Data taken in 2007-2008. (a): expected pinger signal at 250 m distance taking into account the transmission coefficient between water and ice and assuming negligible attenuation length. (b): peak-to-peak amplitude recorded by a sensor deployed at 320 m while the pinger was running in hole 70; all the waveforms recorded have been considered.

### 5.1.4 Systematic effects

The data collected during the pinger runs in 2007-2008 were quite different from expectation. Some examples of the acoustic pulses as recorded by two sensor channels are shown in Figure 5.3-5.4. Each waveform is the result of the folding of the sensor response and the pinger emission spectrum. Each sensor channel has a different sensitivity spectrum, therefore it is expected that waveforms recorded by different channels appear different; waveforms recorded by one channel should be similar in shape with each other. Every waveform shown in the Figure is obtained by averaging all the recorded pinger-pulses to improve the signal-to-noise ratio. The average is computed after correcting for the clock-drift, as it will be explained in detail in section 5.3.2. From the comparison between waveforms recorded by one channel it is possible to observe the following:

- The peak-to-peak amplitude versus pinger depth was far from the prediction and exhibited a strong irregularity of the maximum values of the signal. An example is shown in Figure 5.2(b).
- Waveforms recorded by the same channel when the pinger was at the same depth in two holes at the same distance were very different. An example is provided in Figure 5.3(a)-(c) where data recorded by the sensor channel AS6-1 with the pinger in Hole 71 and 77 are shown.
- Waveforms recorded by the same sensor when the pinger was in aligned holes showed a different shape. This can be seen for example in data recorded by

| Systematic effect | Effect on $\lambda$ | I | II | Related to |
|---|---|---|---|---|
| Channel-to-channel sensitivity variation | varying | v | v | data set selection |
| Azimuthal sensitivity variation | decreases | x | - | geometry |
| Polar sensitivity variation | decreases | x | - | |
| Interference with reflections from hole back wall | varying | x | - | position emitter in the hole |
| Water-ice transmission coefficient variation and shear waves production | decreases | x | - | |
| Hole ice, cracks, inhomogeneities | varying | x | - | |
| Saturation | increases | x | - | data processing and analysis |
| Noise, if not subtracted | increases | v | v | |
| Residual clock drift | varying | v | v | |

| x | strongly present | - | minimized | v | solved |
|---|---|---|---|---|---|

Table 5.2: Systematic effects present in various attenuation analyses and their influence on the estimated attenuation length [72]. I and II refer to season 2007-2008 and 2008-2009, respectively.

the sensor channel BS7-0 when the pinger was in Hole 69 and 70 (see Figure 5.4) and in data recorded by AS6-1 when the pinger was in Hole 70 and 71 (see Figure 5.3(b)-(c)).

The instability of the waveforms had various causes difficult to decouple. A detailed study of the pinger configuration and of the waveform features has brought to the definition of a list of systematic effects which influenced the quality of the data. These are summarized in Table 5.2: in the first column the reasons for data instability are listed; in the second, the effect of each one of them on the estimate of the attenuation length is given. The third and the fourth column show the importance of the effect on the data collected in the first and in the second pinger season respectively. In the last column it is shown how the effect can be minimized. In the following paragraphs, an explanation regarding each of these effects is given.

### Variation of sensor sensitivity from channel to channel

As explained in section 4.1.1, every SPATS sensor is made of three piezoelectric ceramics which act as independent channels. In our case, the sensitivity of each of them depends on the $d_{33}$ constant of the material, but also on how each piezoelectric ceramic is pressed against the housing in the final mounting of the SPATS sensor [65]. To combine data recorded by different channels is difficult due to the unknown difference in sensitivity. In the pinger campaign, a unique source was moved to various distances. It is therefore possible to select and analyze at one time all the data recorded by a single channel and perform an attenuation length measurement independent of the sensitivity of the single channel.

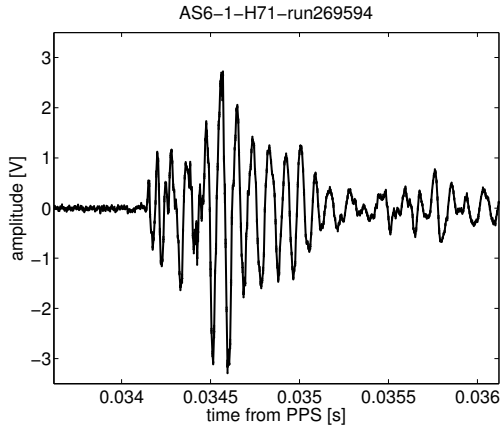


(a)

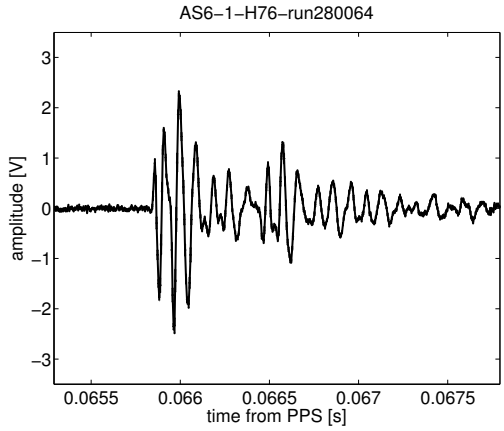


(b)

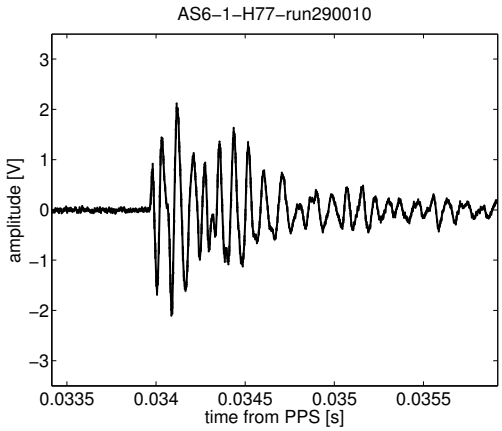


(c)

Figure 5.3: Data taken in 2007-2008: waveforms recorded by the same channel when the pinger was in aligned holes (see (b) and (c)) and in holes at the same distance (see (a) and (c)).

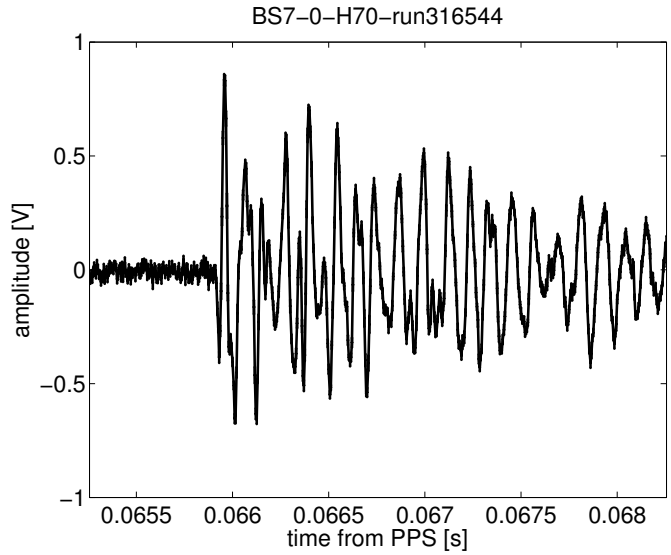


(a)

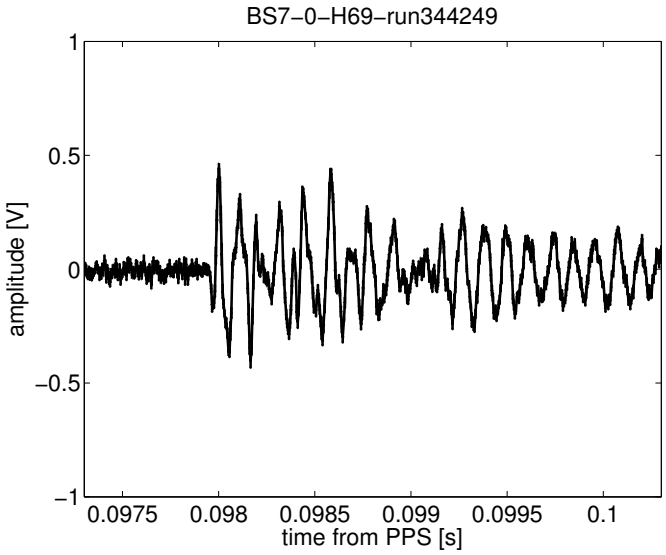


(b)

Figure 5.4: Data taken in 2007-2008: waveforms recorded by the same channel when the pinger was at the same depth, in aligned holes (69 and 70).

### Variation of sensor sensitivity on azimuth

The angular dependence of the sensitivity is a known issue: a variation on the order of 40% was measured in water for one SPATS sensor module along the full range of azimuthal angles [73]. Measurements in South Pole ice indicate that the actual sensitivity varies up to 300%. If data from a wide angular range are combined for an attenuation analysis, the estimated attenuation length can be considerably affected by this variation, resulting in values larger or smaller than the true one depending on the combination of the particular sensor response and on the angles at which it is probed. This problem can be overcome if data are selected within a small azimuthal range. In the runs taken in 2007-2008 only the three Holes 71, 70 and 69 are aligned in the direction of String B and were therefore suited to minimize this effect; any other combination of three or more pinger holes implies an angle wider than 60 degrees as seen by the sensors of a SPATS string.

### Variation of sensor sensitivity on polar angle

The sensitivity of the sensor modules exhibits a strong variation dependent not only on the azimuthal but also on the polar angle. As for the azimuthal angle, the effect on an attenuation length measurement done using data distributed over a wide polar range is unpredictable. The uncertainty due to the polar variation of the sensitivity can be minimized selecting data from the same channel when the pinger was at the same depth as the sensor in many holes, so that the variation of the polar angle between pinger and sensor plane is minimized. In the season 2007-2008, the depth of the pinger was up to 20 m different from that of the sensor, due to a mistake in the pinger depth calculation from the cable payout. This means that from hole to hole the polar angle pinger-sensor changed by a few degrees. The angle can be calculated making use of simple trigonometry and referring to the scheme illustrated in Figure 5.5.

$$\begin{aligned} &\sqrt{dh_{1S}^2 + dv_{1S}^2} \cdot \cos(a) = dv_{1S} \\ &\sqrt{dh_{2S}^2 + dv_{2S}^2} \cdot \cos(b) = dv_{2S} \\ &c = b - a = \cos^{-1}\left(\frac{dv_{2S}}{\sqrt{dh_{2S}^2 + dv_{2S}^2}}\right) - \cos^{-1}\left(\frac{dv_{1S}}{\sqrt{dh_{1S}^2 + dv_{1S}^2}}\right) \end{aligned} \tag{5.12}$$

where $dh_{xS}$ is the horizontal distance between Hole $x$ and sensor, and $dv_{xS}$ is the difference in depth between pinger in Hole $x$ and sensor. If $dv_{1S} = dv_{2S} = 20$ m, and taking into account the horizontal distances from Table 5.1, one obtains a variation in the polar angle of 6 degrees for Holes 69-71 as seen from String B. If one assumes that the difference in depth between sensor and pinger was $-10$ m and 20 m for two adjacent holes, the angle increases to about 12 degrees.

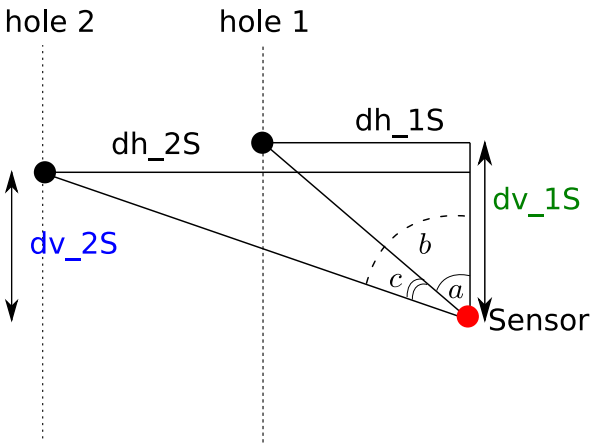


Figure 5.5: Variation of the polar angle between sensor and pinger due to a different stopping depth of the pinger in two holes: $dh_{xS}$ is the horizontal distance between Hole $x$ and the sensor, and $dv_{xS}$ is the difference in depth between pinger and sensor.

### Interference with reflections from the back wall of the hole

As mentioned before, a sound wave going from water to ice is partially transmitted and partially reflected. In the case of the pinger, transmission and reflection happen at the interface hole-wall, in all the directions. The pressure wave which is directly transmitted from water to ice in direction of the sensor interferes with the pressure wave which is first reflected by the back wall of the hole, and then transmitted in ice in the sensor direction, with a certain time delay compared to the one directly transmitted. The concept is illustrated in Figure 5.6. The time of appearance of the interference $T_{int}$ from the beginning of the waveform can be calculated from the size of the hole $d_h$, measured along the direction defined by the pinger and the sensor, and from the distance of the pinger from the hole-wall (in the direction of the sensor) $d_{hw-p}$:

$$T_{int} = T_R - T_D = 2\frac{d_h - d_{hw-p}}{v_{water}} \tag{5.13}$$

where $v_{water}$ is the speed of sound in water. The appearance time of the interference can be easily calculated in the case of co-linearity of pinger, hole-center and sensor. In this case $d_h$ is the hole diameter, which is on the order of 70 cm; the emitter sphere has a diameter of about 10 cm. Assuming that the sound is emitted at the surface of the piezoelectric ceramic, $T_{int}$ is found to range from 100 to more than 900 $\mu$s. The minimum and the maximum values are obtained when the pinger

touches the farthest and the nearest wall in the sensor direction respectively. If the pinger is in the center then the interference pattern happens at $T_{int} \approx 500\ \mu$s.

In 2007-2008 the pinger emitter was free to move and swing in the hole. This had consequences both statically, since the average distance from the hole center changed from hole to hole and from stop level to stop level within the same hole, and dynamically, since nothing prevented the pinger from swinging, or bouncing or rotating freely in the hole as soon as it was stopped. Because of this, the time of appearance of the interference pattern changed continuously, resulting in the waveforms recorded by the same sensor being very inconsistent from one another (see Figure 5.3 and 5.4).

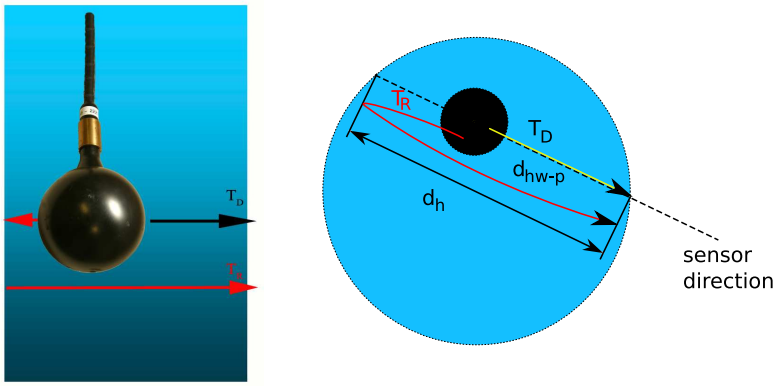


(a) (b)

Figure 5.6: Interference of the transmitted waveform with the one reflected by the backside hole wall, as seen from the side (left) and from the top (right). $T_D$ indicates the time of the direct transmission of the wave, $T_R$ is the time of transmission of the reflected wave.

### Water-ice transmission coefficient variation and shear waves production

In a liquid, sound can only propagate as a longitudinal wave ($P$-wave); in a solid, the propagation can happen also through transverse (shear) waves ($S$-waves). In our case, a pure $P$-wave (emitted in water), crosses the interface water-ice: part of the energy is converted from longitudinal to transverse modes.

The amount of energy which is released in the ice in the form of $P$-waves and $S$-waves depends on the incident angle and on the properties of the two media (densities and speed of sound for $P$-waves and $S$-waves), and can be numerically calculated using the Zoeppritz equations [74]. The solution of these equations in terms of energy in the case of the interface water-ice is illustrated in Figure 5.7. For an incident angle of 0 degrees, the energy of the incoming waveform is completely distributed between $P$ modes: 80% of the energy is transmitted, while 20% is reflected back; no energy is released to $S$-modes. For angles wider than

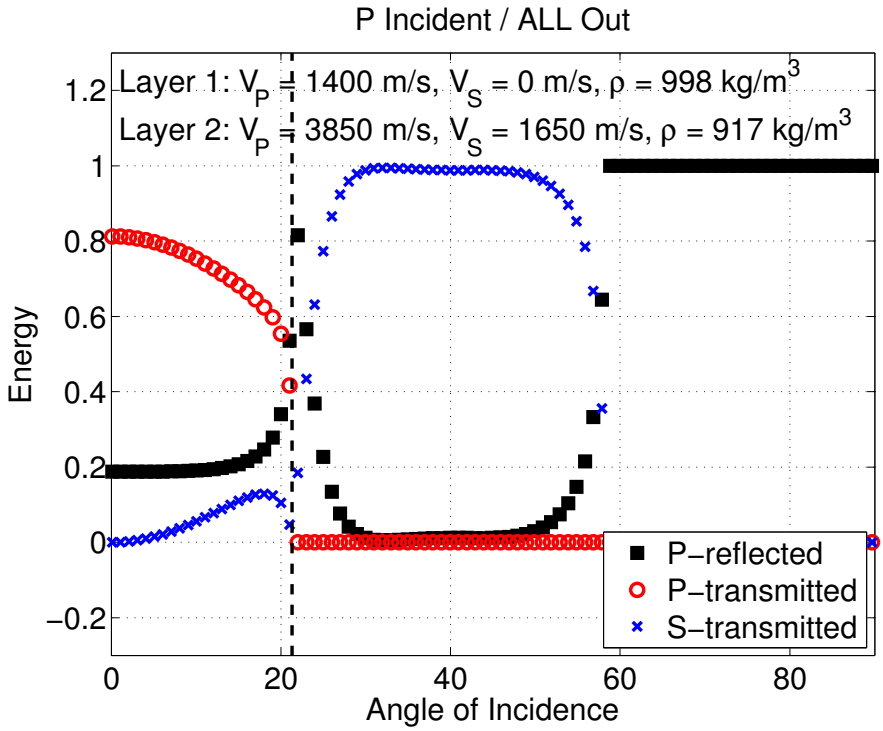


Figure 5.7: Energy transmission coefficient in the case of $P$-wave incident at an interface water-ice, from the Zoeppritz questions. The dashed line indicates the critical angle for *Total Internal Reflection* of $P$-waves.

0 degrees, energy is transferred both to $P$-waves (reflected and transmitted) and to $S$-waves (only transmitted). This happens up to the *Total Internal Reflection* angle, given by:

$$\alpha_{crit} = \sin^{-1}\left(\frac{v_p^{water}}{v_p^{ice}}\right) = 21.3^\circ \tag{5.14}$$

For an incident angle equal or larger than this angle, no energy is transmitted in the ice as $P$-waves: most is transmitted into $S$ modes, while a small fraction is reflected back as $P$-waves. This is valid up to the critical angle for the transmission of $P$-waves to $S$-waves, which is given by:

$$\beta_{crit} = \sin^{-1}\left(\frac{v_p^{water}}{v_s^{ice}}\right) = 58.0^\circ \tag{5.15}$$

For angles wider than $\beta_{crit}$ all of the energy is reflected back into $P$-waves and no energy is transmitted into the ice.

In the 2007-2008 season, the position of the pinger in the hole was random and most likely de-centered compared to the hole axis. Nothing prevented the incident angle of the $P$-wave at the water-ice interface in direction of the sensor from being non-zero. The concept is illustrated in the drawing in Figure 5.8. The result was

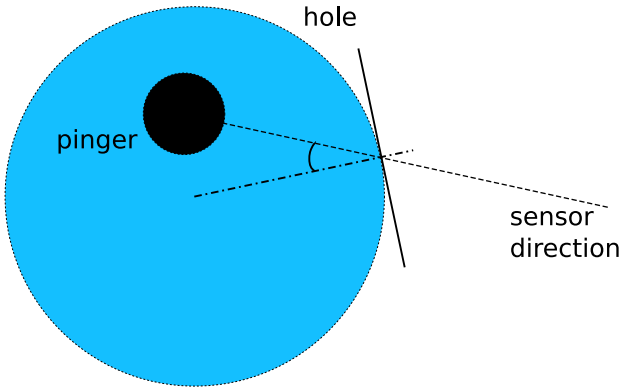


Figure 5.8: Decentralization of the pinger, favorable for shear waves production.

the appearance of shear waves in the recorded waveforms, visible as a second pulse, sometimes even larger than the first one ($P$-wave). A clear example can be seen in Figure 5.9.

Since $P$ and $S$ transmitted waves are somehow anti-correlated, they must be considered separately in an attenuation analysis. Shear waves are predicted to travel with a speed lower than the one for longitudinal waves, but no measurements had ever been done in ice before: the first direct measurement of their speed in South Pole ice was possible using this data [13]. Once the speed of propagation had been measured, all the data collected from the pinger runs were examined in order to get a map of the appearance of the shear waves. This was done by evaluating the excess of energy with respect to noise in the expected $S$-wave time window. An example map for the data taken with String A when the pinger was in Hole 77 is shown in Figure 5.10. Every point marks a waveform recorded by the sensor installed at the depth indicated on the $x$-axis when the pinger was at the depth indicated on the $y$-axis, and it has a different marker whether a $S$-wave is detected or not or if the presence is uncertain. The appearance of shear waves is evident up to a quite large angle between pinger and sensor, as expected from Figure 5.7.

In addition to the production of shear waves, the varying incident angle from one configuration to another caused the variation of the transmission coefficient, which has been defined for 2-dimensional approximation in equations 5.8 and 5.1.

### Hole ice

An IceCube hole is drilled by melting the column of ice with high-pressure hot water. As soon as the drilling is completed, the water filling the hole starts to cool, eventually refreezing to ice. The process lasts several days. The quality of

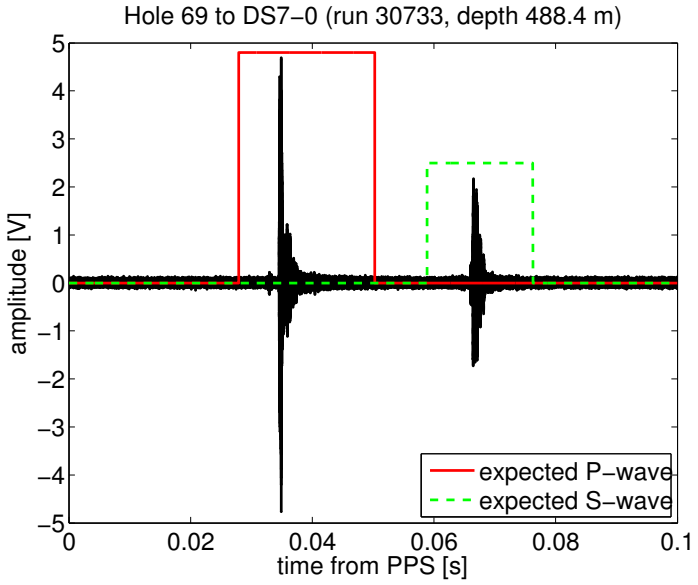


Figure 5.9: Clear example of a waveform showing a $P$-wave and an $S$-wave, recorded by one channel of the sensor of String D installed at 500 m depth when the pinger was in Hole 69 at about 488 m depth.

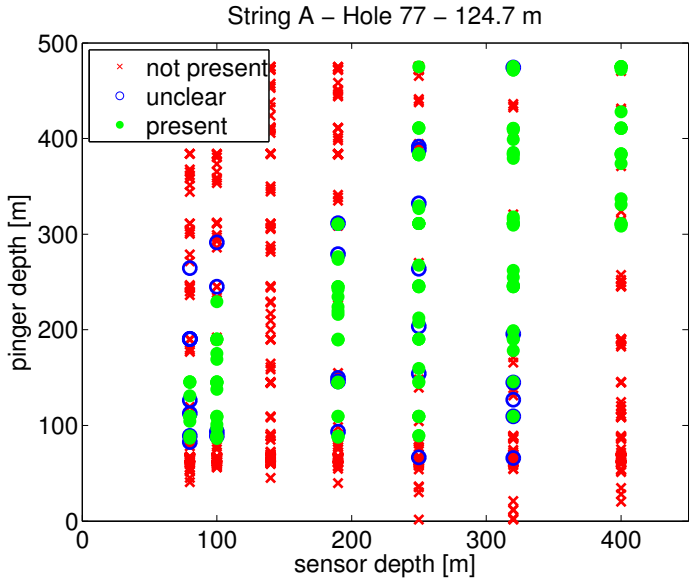


Figure 5.10: Shear waves appearance map for a distance of about 125 m: the shear wave contribution is measured from the waveforms recorded by each sensor in String A for all the stops of the pinger in Hole 77 (in season 2007-2008.

the so called "hole-ice", which surrounds the deployed instrumentation, is not well known. It is assumed that bubbles eventually convert to air hydrate crystals if the static pressure is sufficiently high. However, the presence of inhomogeneities as well as of micro-cracks at the hole-bulk interface cannot be excluded. These could lead to unknown and inhomogeneous absorption or scattering near the sensors and to transmission inhomogeneities for the pinger signal.

An additional unknown element is the position of the IceCube cable in the hole, which could shadow the receivers in the case of a specific location of the source.

The consequences of these issues for an attenuation analysis can be estimated considering the following. Any kind of static inhomogeneities around the sensor would likely result in an offset of the absolute amplitude of the signal recorded for the single channel, and therefore would affect the sensitivity measured *in situ* for that channel. If the data used for the attenuation measurement are selected from one single channel and the source is located at varying distances in the same direction, then any local effect should be negligible. To apply this selection criterion to the data collected in season 2007-2008 was not possible due to the geometry and the inexact pinger stopping depths.

### Dynamic range

The sensors have limited dynamic range due to the maximum and minimum output voltage from the differential amplifier. This means that the amplitude of the source signal must be chosen carefully: indeed if the signal is too strong, the sensor output signal will saturate, and only limited information will be available in the waveform; on the other side, of course, if the source signal is too weak, the signal-to-noise ratio will be too poor at large distances. It is very difficult to predict which would be the signal power necessary for the pinger in order to have most of the sensors out of saturation but still capable to receive the signal. In some cases saturation appeared at the nearest distance (125 m) making a part of the data collected at near distances in 2007-2008 useless. The inclusion of saturated signals in an attenuation analysis would lead to an overestimation of the attenuation length, since the amplitude flattens at the nearest distance (where saturation happens).

### Noise

The waveforms recorded when the pinger was operating contain a contribution of both signal and noise. Noise must be correctly subtracted in order to get the real signal; if this is not done, the attenuation length is overestimated since it flattens to noise at the larger distances.

### Clock drift

Each String PC uses a single clock to drive its analog-to-digital converters (ADCs), which are used to sample and record the sensor waveforms (see also section 4.1.2

for a description of the system). The clocks drift at a rate that is typically on the order of about 10 parts per million and varies with time. Over 10 s, this cumulative amount of drift is on the order of one signal oscillation period and therefore can cause strong de-coherence in the pulse averaging if the nominal rather than true sampling frequency is used.

This clock drift effect can be corrected on the sensor side thanks to the IRIG-B signal. To do this, the algorithm described in [69] and summarized in section 5.3.2 has been adopted in the following analyses.

On the side of the pinger, the pulse emission is driven by the frequency multiplier and by the GPS receiver by the company *Garmin*. The delay of the PPS pulse provided by the latter, compared to the one provided by GPS receiver which drives the string ADCs, has been measured to be 1 $\mu$s. The accuracy in time of the pulses in the train was measured in the laboratory to be approximately 10 $\mu$s over the recording time for a single channel (see section 4.2.5). The drift on the pinger side cannot be corrected, and contributes to the statistical uncertainty described in the data processing section (5.3.2).

If the waveforms are not corrected for the clock drift, their average will be affected by destructive de-coherence, since samples belonging to different true times will be averaged together. The size of the effect can vary and be more or less important for the attenuation analysis; however, it is likely that low signals, and therefore combinations at farther distances, will be more affected by this effect.

## 5.2 Pinger data from 2008-2009

### 5.2.1 Geometry

| Pinger Hole | A | B | C | D |
|---|---|---|---|---|
| 28 | 661.2 m | 544.9 m | 243.3 m | 750.0 m |
| 19 | 743.5 m | 632.1 m | 335.7 m | 807.5 m |
| 5 | 976.0 m | 866.1 m | 569.6 m | 1023.4 m |
| 37 | 567.2 m | 453.4 m | 156.5 m | 653.3 m |

Table 5.3: Distances between the SPATS strings and the pinger holes in 2008-2009.

Four IceCube Holes (28, 19, 5, 37) were available for the pinger in the season 2008-2009 (see the map in Figure 5.11). The distances from the SPATS array ranged from 156 m (String C - Hole 37) to 1023 m (String D - Hole 5), with a maximum azimuthal variation of about 13 degrees (for String D, while the other angles are 7.2 degrees for String A, 6.6 degrees for String B, 8.2 degrees for String C). The complete list of distances is presented in Table 5.3.

The depths of 190, 250, 320, 400, 500 m were chosen as stop levels. The pinger was stopped for 5 minutes once during lowering and once during rising, to check the

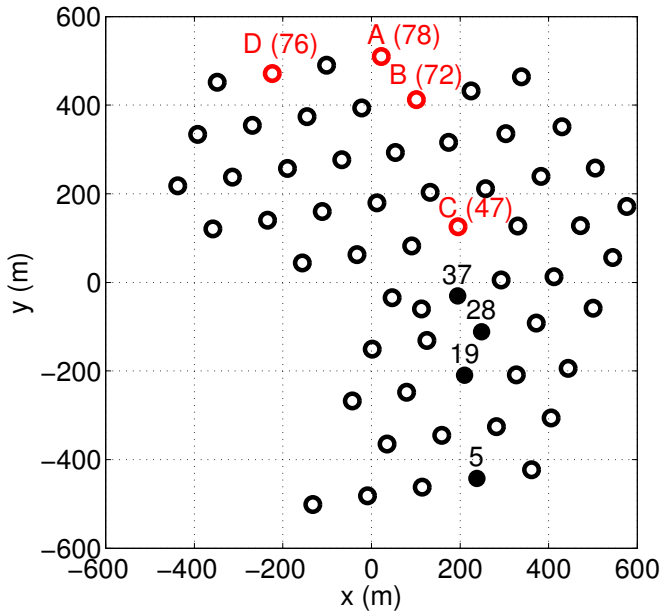


Figure 5.11: Geometry of IceCube-59 with the SPATS strings (in red circles, labeled with letters and numbers) and the holes in which the pinger was run in the season 2008-2009 (black-filled circles labeled with numbers).

reproducibility of the waveform at each of these depths. The depth was monitored both by three pressure sensors attached to the stage and by the cable payout, measured using an automatic turn counter installed on the winch. The data were averaged to determine the stopping depth within a certain error. An example of the estimated actual depths is illustrated for one hole in Table 5.4; the others are very similar. Due to the different calibration of the pressure sensors and the little discrepancy between the depth calculated from pressure and the one calculated from payout, the estimated error is 5 m.

### 5.2.2 Data acquisition

Thanks to a data-taking optimization, in the season 2008-2009 it was possible to record simultaneously the three channels of the same sensor. Data were taken only with sensors which are installed at the pinger stopping depths; since String A, B, C have no instrumentation below 400 m depth, the sensors at 400 m were used simultaneously with the sensor of String D located at 500 m depth. A specific data acquisition program was written in the way that all the selected sensors were used for each stop level of the pinger.

The recording duration and interval between two consecutive recordings were chosen in order to satisfy the constraints given both by the limited size of the RAM disk of the String PC (the local memory) and the time necessary to transfer the data from the String PC to the Master through the DSL connection. The maximum

| nominal depth | depth from payout | depth from pressure |
|---|---|---|
| 190 m | 190.0 m | 187.1 ± 1.9 m |
| 250 m | 249.9 m | 247.3 ± 2.5 m |
| 320 m | 320.2 m | 318.3 ± 3.1 m |
| 400 m | 400.0 m | 399.1 ± 3.0 m |
| 500 m | 499.9 m | 499.9 ± 4.6 m |
| 400 m | 400.2 m | 398.8 ± 3.3 m |
| 320 m | 320.0 m | 318.2 ± 1.7 m |
| 250 m | 249.9 m | 247.1 ± 1.7 m |
| 190 m | 189.9 m | 186.7 ± 1.2 m |

Table 5.4: Nominal and actual stopping depths where the pinger was run in 2008-2009 for Hole 19. Depth from the payout is the one calculated from the turn-counter on the winch. Depth from pressure is obtained by averaging the data from the three pressure sensors installed on the stage; the shown error is the standard deviation calculated from the data of the three sensors.

duration of the recording at 200 kHz on the three channels of one sensor was found to be 18 s. As soon as the data were taken, they were saved in a file which was transferred to the Master PC. Given the file size (between 12 and 13 MB), the local memory size (about 98 MB) and the speed of the data transfer, an overall time of 47 s was found to be necessary to prevent the filling up of the RAM disk. After this time, the local space was enough to start again the acquisition of the data, this time with another (deeper) sensor. The String PCs times are synchronized within a few ms with the *Network Time Protocol* NTP. The pinger data taking script was started in each String PC at an established time, a few hours before the start of pinger run, using a Unix time-based job scheduler (called *cron*). In this way all the sensors at the same depth were recording at the same time; after about 47 s the recording started for all the four sensors at the deeper level. To keep a good synchronization, the *cron* job restarted the script every 4 minutes, corresponding to a few seconds more than the time necessary to loop over the sensors at all the depths (3 minutes and 55 seconds); the time mismatch accumulated over a whole loop time was about 1 s. In this way each acoustic pulse was recorded simultaneously by all the sensors located at equal depth: this would have made it possible to monitor any eventual (and unexpected) time variation of the pinger acoustic emission. A stop time of 5 minutes per level was established in order to guarantee that for every pinger stop all the levels had recorded the signal, with some redundancy, in order to discard eventual bad-quality data recorded with the pinger moving or bouncing at the beginning of the stop.

The repetition rate used to trigger the pinger was 10 Hz in all the holes except for Hole 37, in which by mistake the pinger was operated at 8 Hz repetition rate.

### 5.2.3 Data quality - residual systematics

In 2008-2009 the data turned out to be very stable and consistent from hole to hole. A comparison between waveforms is shown in Figure 5.12. In each frame, the two waveforms recorded when the pinger was at the same depth in the same hole on the way down (black continuous line) and on the way up (red, dashed line) are shown. The three frames show the waveforms recorded by the same channel when the pinger was in three different holes. It is clear that the waveforms all look very similar not only for repeated stops in one hole, but also for stops in different holes.

One of the reasons for the improvement of the data quality is the addition of the centralizers, which prevented the swinging and forced the sound source to stay near the hole center. This had important consequences:

- The interference between transmitted and reflected waveforms was forced to appear always about 500 $\mu$s after the beginning of the waveform. This caused the shape of the waveforms recorded by the same channel to be very stable.

- The appearance of shear waves for data taken in the configuration sensor-pinger at the same level was minimized. Shear waves were still found on diagonal paths but with lower intensity than in the 2007-2008 configuration. It should be noticed that the data in 2008-2009 were taken at larger distances, therefore it is possible that shear waves disappear due to a shorter attenuation length than that of longitudinal waves.

The higher quality of the data collected in the season 2008-2009 must be attributed also to the favorable geometry. All of the four holes in which the pinger was operated are basically aligned as seen by any SPATS string. This minimized the variation of the azimuthal angle in the data recorded by the same channel. In addition, a higher precision (about $\pm 5$ m) was achieved in the pinger depth determination by the cable payout; this pulled down the effect of the sensitivity dependence on the polar angle.

The systematic uncertainties present in the data from 2008-2009 are due to the residual presence of some of the issues explained in Table 5.2. The difference in depth between pinger and sensor has a clear effect which can be seen comparing carefully the waveforms recorded when the pinger was stopped at the same level as the sensor, on the way down and on the way up. The difference in depth mirrors in an offset between the waveforms. One of the most extreme cases is shown in Figure 5.13, where the delay between the two signals is about 40 $\mu$s. The minimum difference in depth can be calculated assuming that in one of the two cases the pinger is at the same depth as the sensor, using simple trigonometry:

$$\Delta z = \sqrt{(c\Delta t + d_{hor})^2 - d_{hor}^2} \tag{5.16}$$

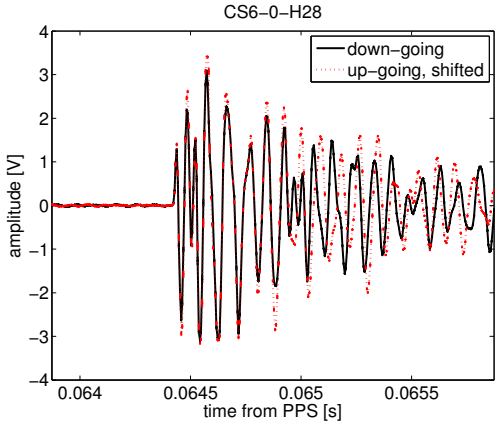


(a) CS6-0, pinger in Hole 28

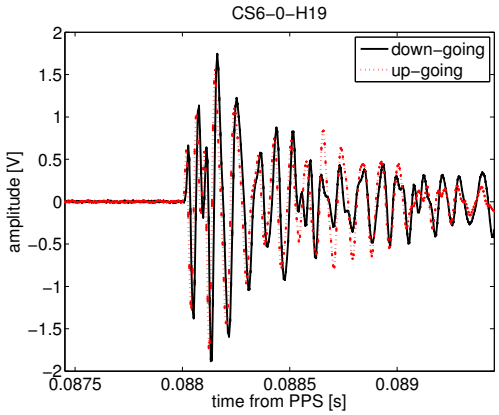


(b) CS6-0, pinger in Hole 19

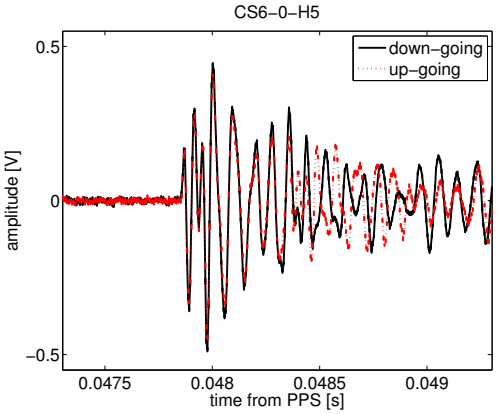


(c) CS6-0, pinger in Hole 5

Figure 5.12: Waveforms recorded by the same channel for three different pinger holes when the pinger was stopped on the way down and on the way up. The up-going red-dashed waveform shown in (a) has been artificially shifted to correct for the offset resulting from an unequal stopping depth.

Introducing in the formula the measured offset in time $\Delta t \approx 40$ $\mu$s and the horizontal distance from pinger hole to sensor $d_{hor} \approx 243$ m, the minimum difference in depth is found to be $\Delta z \approx 8.6$ m, which is within the estimated error $\pm 5$ m for each of the two points.

From the point of view of shear production, the effect of the difference in depth between sensor and pinger is still negligible. In the worst possible case of $\Delta_z \approx 10$ m and $d_{hor} \approx 156$ m (the nearest distance in the season 2008-2009), assuming the pinger at the hole center, the angle between pinger and sensor is calculated using equation 5.7:

$$\theta_{ice} = \cos^{-1}\left(\frac{d_{hor}}{\sqrt{d_{hor}^2 + \Delta_z^2}}\right) \approx 3.7^\circ \tag{5.17}$$

from which the incident angle in water can be calculated using equation 5.2:

$$\theta_{water} = \sin^{-1}\left(\sin\theta_{ice} \cdot \frac{v_{water}}{v_{ice}}\right) \approx 1.3^\circ \tag{5.18}$$

which is small but not zero. The varying difference between pinger and sensor depth from one to another stop is therefore indirectly also the source of other systematic uncertainties. The small variation of the polar angle between pinger and sensor plane induces a variation of the transmission coefficient and implies that the sensitivity of the sensor is not always perfectly the same. Moreover, the path-length between the directly transmitted waveform and the reflected one is slightly different from run to run, and this reflects in the little variation of the interference pattern, starting at about 500 $\mu$s after the beginning of the waveform (refer to equation 5.13 and corresponding discussion), which is visible in the Figure 5.12.

In addition to these issues, the variation of the azimuthal angle from hole to hole is small but not zero; this also implies a different sensor sensitivity. All these effects combine with the eventual presence of inhomogeneities in the hole-ice, which could be distributed unevenly in the space surrounding the module. Some attempts to estimate the residual systematic uncertainties from the data will be described later in this Chapter in the sections regarding each analysis.

## 5.3 Attenuation analysis

### 5.3.1 Data set selected

To perform an attenuation analysis with the smallest influence of systematic effects it is necessary to:

- Use data recorded by one single channel for several pinger distances, so that data recorded by sensors with different absolute sensitivities are not combined.

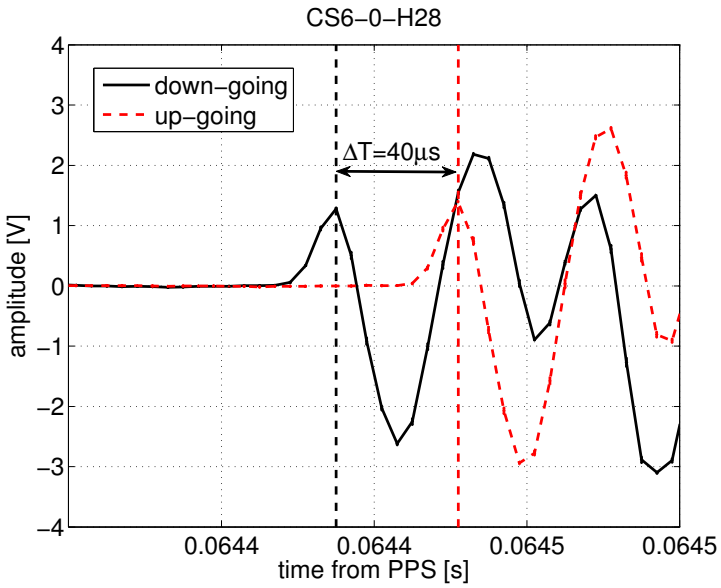


Figure 5.13: Zoomed-in view of the waveform in Figure 5.12(a) without time-offset correction. The offset corresponds to the difference in depth where the pinger stopped on the way down and on the way up from equation 5.16.

- Have the pinger at multiple distances aligned in the same direction with respect to the sensor location: this minimizes the influence of any azimuthal variation of the sensor sensitivity.

- Have the pinger at the same depth for every distance used: this minimizes the influence of any polar variation of the sensor sensitivity.

For all the analyses which will be described below, we selected all the non-saturated waveforms recorded by a single sensor channel when the pinger was stopped at the sensor depth in the four holes. This data set fulfills all the requirements listed above and preserves a moderately high redundancy: 49 independent combinations are available, since the active sensors are four for String A, B, C and five for String D and all the sensors have three channels except HADES which has one.

A fundamental prerequisite for the analysis is of course that the pinger emission is constant throughout all the measurements. This is a reasonable assumption since the chosen piezoelectric ceramic is specified to work down to 1250 m depth. Moreover, generally only data recorded at a same depth of the pinger are combined, therefore any eventual variation of the pinger spectral emission with depth should not influence the attenuation analysis. An exception in which this effect, if measurable, should be considered, is the diagonal attenuation study, presented in section 5.6.

### 5.3.2 Data processing

We want now to look into the features of the waveforms of the chosen data set. The total sampling time for one channel was 18 s: this time will be called $T_{rec}$. The sampling frequency was $f_s = 200$ kHz, sufficiently high given the bandwidth of our sensors and the main frequency content of the source emission (see below). The raw-data sampled during this time are called "run". For each stop of the pinger there is at least one run recorded by every channel. One run contains a number of transmitted pulses equal to:

$$N_p = f_{rep} \cdot T_{rec} \tag{5.19}$$

which means 180 pulses for Holes 5, 19 and 28, where the repetition rate used was $f_{rep} = 10$ Hz, and 144 pulses in the case of Hole 37, where the repetition rate was $f_{rep} = 8$ Hz.

Prior to the analysis, the waveforms are processed to achieve high quality with the following steps:

1. **Clock drift correction**
   As explained in the section 5.1.4, the clock which drives the analog-to-digital converter in the String PC drifts. This means that the sampling frequency slightly varies with time in a non-linear way. The drift can be properly corrected using the GPS IRIG-B signal, which is sampled synchronously with the data. From the IRIG-B signal, the true sampling time of each sample can be reconstructed and then applied in order to "stretch" the data from the nominal to the true time. The algorithm used is described in [69]. The time $t_i$ of the sample $i$, having amplitude $V_i$, is shifted by the time (positive or negative) $\Delta T_i$:

$$V_i(t_i) \mapsto V_i(t_i^{corr} = t_i + \Delta t_i). \tag{5.20}$$

2. **Wrap in time**
   Since the absolute time of the recorded data is not relevant in the analysis, the time-stamp $t_0$, which provides the absolute time corresponding to the beginning of the recording for that channel, is subtracted from the real sampling times:

$$t_i^* = t_i^{corr} - t_0 \tag{5.21}$$

   Next the 18 s long pulse trains are wrapped in time in the following way:

$$t_i' = t_i^* \bmod 1/f_{rep} \tag{5.22}$$

   where the *mod* symbol indicates the modulo operation which returns the remainder of the division. In this way all the samples from the $N_p$ pulses, originally having time between $t_0$ (indicating the particular start time of the data acquisition for that channel) and $t_0$+18 s, are folded in one unique pulse

with a high density of points in time, with the starting time corresponding to 0 to the beginning of the GPS second:

$$V_i(t_i), t_i \in [t_0 \rightarrow t_0 + 18\ s + \sum_i \Delta t_i] \mapsto V_i(t'_i), t'_i \in [0 \rightarrow 1/f_{rep}[s]]. \quad (5.23)$$

3. **Average**
   At this point the average can be computed to reduce the noise by $\sqrt{N_p}$ and improve the signal-to-noise ratio by the same factor. The samples are sorted in times and re-binned in bunches of $N_{bin}$, a number which is chosen differently for each analysis (see details in the corresponding sections). For all the $N_{bin}$ samples in the same bin $k$ the mean value of the amplitude $A_k$ and the corresponding standard error of the mean $\sigma_{A_k}$ are computed:

$$A_k = \frac{\sum_{i=(k-1)N_{bin}+1}^{kN_{bin}} V_i}{N_{bin}} \quad (5.24)$$

$$\sigma_{A_k} = \frac{1}{\sqrt{N_{bin}}} \cdot \sqrt{\frac{\sum_{i=(k-1)N_{bin}+1}^{kN_{bin}} (V_i - A_k)^2}{N_{bin} - 1}}. \quad (5.25)$$

   The same procedure is applied to the time values of the samples:

$$t_k = \frac{\sum_{i=(k-1)N_{bin}+1}^{kN_{bin}} t'_i}{N_{bin}} \quad (5.26)$$

$$\sigma_{t_k} = \frac{1}{\sqrt{N_{bin}}} \cdot \sqrt{\frac{\sum_{i=(k-1)N_{bin}+1}^{kN_{bin}} (t'_i - t_k)^2}{N_{bin} - 1}}. \quad (5.27)$$

   The amplitudes $A(k)$ and the times $t_k$ (with the corresponding errors $\sigma_{A_k}$ and $\sigma_{t_k}$) define what we use as "waveform" for each of the analyses presented in the following sections. The waveform contains one single pulse and is made of a number of samples equal to:

$$N_w = \frac{1}{f_{rep}} \cdot f_s \cdot \frac{N_p}{N_{bin}}. \quad (5.28)$$

   Therefore the index $k$ in the expressions above goes from 1 to $N_w$. Given the repetition rate of the pinger and the sampling frequency used, $N_w = 25000$ for Hole 37 and $N_w = 20000$ for Holes 5, 19 and 28.

This procedure is applied to all the files in the data set illustrated in section 5.3.1; in this way a high quality pulse is available for each channel-hole combination.

### 5.3.3 Fitting procedure

In this section, some basic concepts and equations, which concern all the analyses presented below, are explained.

The signal amplitude is proportional to the acoustic pressure. For a point source with a spherical emission, in the far field approximation, the pressure amplitude scales due to a geometrical factor and to medium attenuation:

$$A(d) = \frac{A_0}{d} e^{-\alpha d} = \frac{A_0}{d} e^{-d/\lambda}. \tag{5.29}$$

This equation can be turned into the linear equation:

$$y = \ln(Ad) = \ln(A_0) - \alpha d = b_0 - \alpha d \tag{5.30}$$

where

- $A$ is the amplitude, for example in [V]: the value of this variable is proportional to the pressure amplitude, folded with the sensitivity of the sensor; the way it is defined will become clear in the context of each of the analyses presented.
- $d$ is the source-sensor distance (*e.g.* in [m]).
- $\alpha$ is the acoustic attenuation coefficient and $\lambda$, the attenuation coefficient, is its inverse (in units respectively *e.g.* [$m^{-1}$] and [m]).
- $A_0$ is some characteristic constant which defines the sound at the source (sometimes it is taken to be the amplitude of the acoustic pressure at 1 m from the source); $b_0$ is a free normalization parameter related to the sensitivity of the particular sensor piezoelectric ceramic: $A_0 = \exp(b_0)$.

Inserting in the equation the values of $y_i$ (calculated from the data) for multiple distances $d_i$ a simple linear regression can be performed minimizing the least-squares sum for the two parameters $b_0$ and $\alpha$ [75].

To improve the quality of the fit and to minimize the correlation between the two parameters, the parametrization is chosen such that the fit is centered in the middle of the range of distances for which data exist for a particular channel:

$$y = -\alpha(d - d_0) + b' \tag{5.31}$$

and the normalization parameter $b_0$ can be obtained as:

$$b_0 = \alpha d_0 + b' \tag{5.32}$$

The error on the variable $y$ is:

$$\sigma_y = \sqrt{\left(\frac{\sigma_A}{A}\right)^2 + \left(\frac{\sigma_d}{d}\right)^2 + \sigma_{sys}^2} \tag{5.33}$$

The first term in the equation 5.33 represents the statistical uncertainty of the amplitude. This is calculated by error propagation of the statistical uncertainty of each sample of the mean waveform and will be made explicit later for each analysis performed.

The second term on the right is given by the uncertainty of the pinger depth and by the uncertainty on the string location and can be expressed as:

$$d = \sqrt{d_H^2 + \Delta_z^2} \tag{5.34}$$

$$\sigma_d = \frac{1}{d}\sqrt{(d_H \sigma_{dH})^2 + (\Delta_z \sigma_{\Delta z})^2} \tag{5.35}$$

where:

- $d_H$ is the horizontal distance between the string and the IceCube hole where the pinger was deployed;
- $\sigma_{dH}$ is the error on the horizontal distance, which has been estimated in [13] to be on the order of $\sqrt{2} \cdot 0.5$ m;
- $\Delta_z = |z_{pinger} - z_{sensor}|$ is the (unwanted) difference in depth between pinger and sensor (less than 5 m);
- $\sigma_{\Delta z}$ is the error on the real pinger depth (assumed 5 m).

The whole contribution can be estimated numerically. The result obtained assuming the worst case is illustrated in Figure 5.14 as a function of the horizontal distance $d_H$ and it is completely negligible in the analysis when compared to the other uncertainties.

The last contribution in equation 5.33 is the systematic uncertainty, and it is the most difficult to estimate. The residual systematics have been explained in detail in section 5.2.3; different methods have been implemented in the different analyses to estimate this error and will be illustrated below.

### 5.3.4 Overview of the different analyses

For the attenuation coefficient determination, different variables have been considered: the amplitude of the first peaks, the energy of the waveform, and the integral of the spectrum in selected bandwidths. In the following sections, a detailed discussion about each analysis will be presented: the definition of the studied variable, the procedure and the results will be given.

### 5.3.5 First peaks analysis

As previously said, the data from the improved pinger show great stability: given a certain channel, the waveforms recorded when the pinger was at the same depth

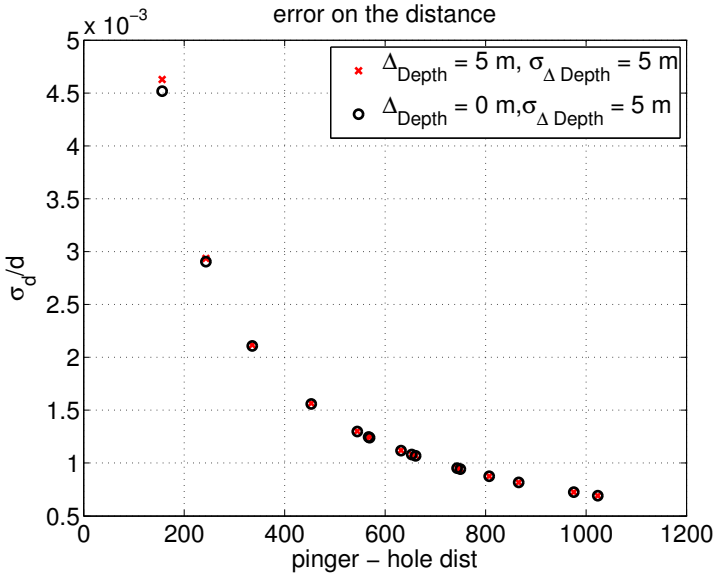


Figure 5.14: Estimation of the error on the distance between pinger and receiving sensor in the worst case (assuming a $\Delta_z = 5$ m and $\sigma_z = 5$ m).

as the sensor in different holes look alike once they have been corrected for the clock drift and averaged. This similarity in shape is very strong at the beginning of the waveform, before the appearance of any interference; for this reason the first analysis of the pinger data has been conducted using the amplitude of the first positive and first negative peak of the waveform.

The procedure adopted to pre-process the waveform is explained in the section 5.3.2. The samples, corrected for the drift, are wrapped by the modulus of the repetition rate and ordered in time. In order to achieve a virtually higher sampling frequency and keep the computational time sufficiently low, the number of points for re-binning (to get the mean waveform, see equation 5.24) has been chosen to be $N_{bin} = N_p/2$. In this way the mean waveform has a sample every 2.5 $\mu$s; the value of each sample is the mean of the $N_p/2$ points, while the error is the standard error of the mean of these points (as specified in equation 5.25).

All the mean waveforms recorded by the same channel (at any available distance) are compared to verify the consistency of their shapes; this aims to select the first two peaks of different polarity which are visible in the whole range of distances. For the nearest strings, the peaks chosen are always the first in time; in other cases, in order to recover missing data points at far distances where the signal to noise ratio is poor, a higher, later peak is selected rather than the first. The requirement on the choice is that the selected peaks should be the first appearing in time which are visible and recognizable in the waveforms for the same channel at all the distances. An example of selection of peaks is shown in Figure 5.15(a). The technique requires that the waveforms recorded by a channel for each

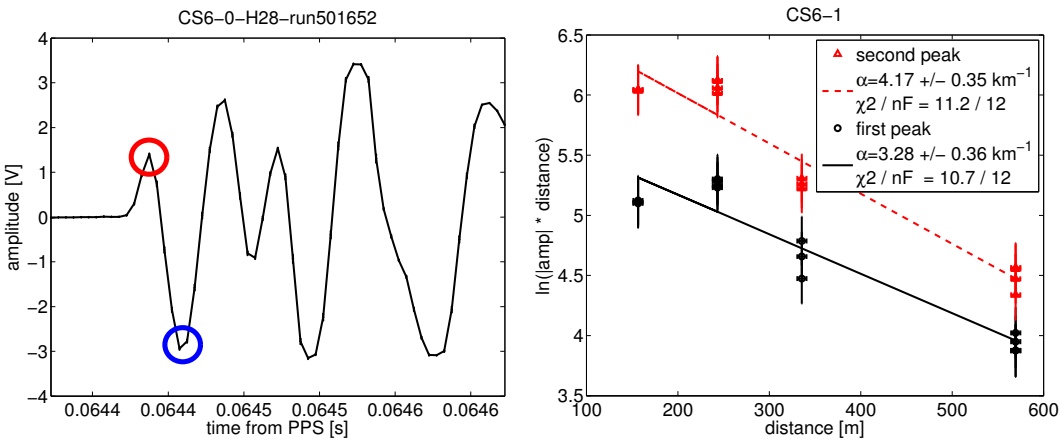


(a) First peaks technique

(b) First peaks example fit

Figure 5.15: Illustration of the first peaks method (a) and example fit of the two peaks for one channel (b).

pinger distance have a good signal-to-noise ratio. Globally the procedure was applied successfully on the three channels of CS6, BS6 and DS4 (all located at 320 m depth), on the three channels of CS7 and on AS7-2 (all located at 400 m depth).

Once the chosen peaks are isolated in each waveform, a very simple, manual algorithm is used to get the maximum of the positive peak and the minimum of the negative peak. To re-bin the points by $N_p/2$ helps since no interpolation is done on the peak to find the maximum, but the maximum value is chosen directly.

This procedure is applied to all the data from different configurations for the same channel, providing a list of values for the amplitude of the same peak as a function of the distance. Often more than one point is obtained for a single distance value since more than one run was taken when the pinger was stopped at that level.

Each of the values has an error which is made of a statistical component and a systematic one. The "statistical error" on the peak value is the error on the mean calculated using 5.25 with $N_{bin} = N_p/2$.

To estimate the systematic error, a study is performed on the multiple runs taken in the same configuration, *i.e.* during the stops done in the lowering and in the raising of the pinger in the same hole. Theoretically the value of the first peak for a single channel should be the same in all these runs; quantifying the difference between the values gives a hint of the global uncertainty related to that particular configuration. To determine it, the mean value of the amplitude of the same peak for a given combination hole-channel $\left\langle A_{peak}^{hole-channel} \right\rangle$ is calculated from all the mean values of the available runs $\left\langle A_{peak,run}^{hole-channel} \right\rangle$; then the difference of each

value to the mean, normalized to the mean, is computed:

$$\frac{\left\langle A_{peak,run}^{hole-channel} \right\rangle - \left\langle A_{peak}^{hole-channel} \right\rangle}{\left\langle A_{peak}^{hole-channel} \right\rangle}. \tag{5.36}$$

This is repeated for all the configurations and for all the sensors and channels; the histogram of these values is shown in Figure 5.16. The standard deviation of the first moment distribution of the peak amplitude, as defined by equation 5.36, is 13%. This value is used as the value for the systematic error on the amplitude.

Once the statistical and the systematic error are defined, the linear fit of the variable $y$ is performed for the data from each channel as described by the equation 5.31: the attenuation coefficient $\alpha$ and the normalization constant $b_0$ are calculated with the corresponding confidence levels. An example fit on the two peaks of the same channel is shown in 5.15(b).

The normalization constants are next used to rescale the data from different channels and perform a global fit, assuming a depth independent attenuation coefficient:

$$\begin{aligned} x' &= d \\ y' &= y - b_0 \\ \sigma'_y &= \sqrt{\sigma_y^2 + \sigma_{b0}^2} \end{aligned} \tag{5.37}$$

At this point the values of $y'$ obtained by each channel are channel-independent and can be combined to perform a global fit. Since for a given distance more than a single point is available, an average is performed, using the standard deviation of the points as additional error. The plot of the combined fit for all the data available is shown in Figure 5.17. The result of the fit is:

$$\begin{aligned} b_0 &= 0.06 \pm 0.15 \\ \alpha &= 3.48 \pm 0.31 \text{ km}^{-1} \end{aligned} \tag{5.38}$$

which translates into an attenuation length equal to:

$$\lambda = 287^{+28}_{-23} \text{ m}. \tag{5.39}$$

It can be noticed that the parameter $b_0$ has a value consistent with 0, which means that the normalization from the single channel data has been done properly (see equations 5.37). From the reduced $\chi^2$ it appears that the errors are overestimated.

This analysis is the most direct and obvious, but suffers from several problems: first of all, it is based on the amplitude at only one point of the waveform. This means that only a minimal part of the information is used. The possible presence of $S$-waves is not taken into account and there is no chance to discern any frequency dependence. Moreover, only a few combinations could be analyzed successfully, since the method is time consuming and requires to discriminate the peaks by eye.

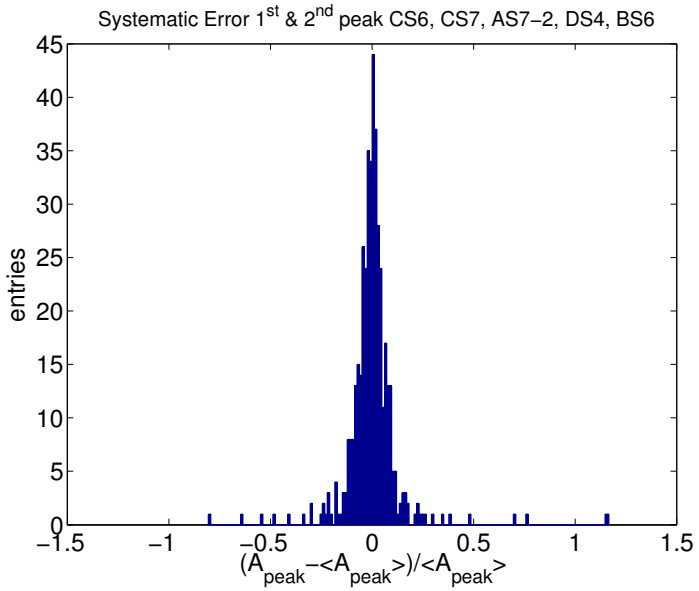


Figure 5.16: Systematic error estimation for the first peaks method. The histogram shows the first moment distribution of the peak amplitudes, for the peaks from all the sensors which could be successfully analyzed using the first peaks method: BS6, CS6, DS4, CS7, AS7-2.

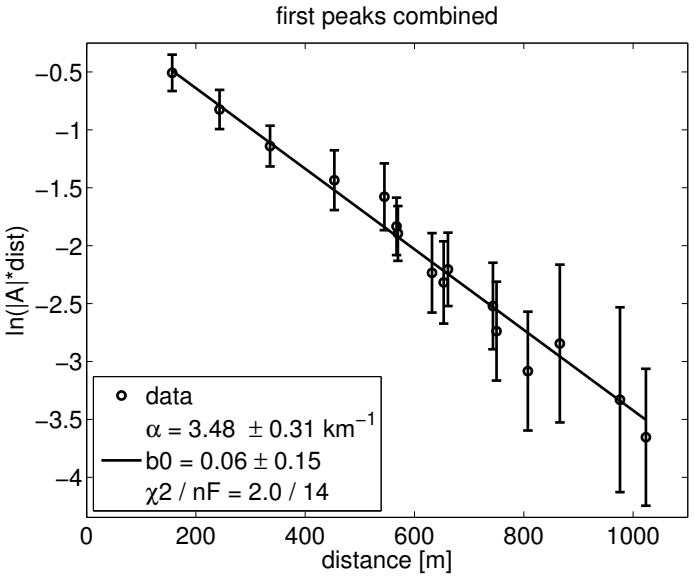


Figure 5.17: Combined fit for all the data analyzed with the first peaks method. This includes the values from 5 sensors, corresponding to 9 channels at 320 m depth and 4 channels at 400 m depth. Data at the same distance have been averaged.

### 5.3.6 Energy analysis in the time domain

**Full waveform**

Another variable which can be considered in order to estimate the attenuation is the energy of the waveform, which has on the one hand the advantage to give an "integral" information. On the other hand, any contribution to the energy coming from $S$-waves is included in the analysis. However, as discussed in section 5.2.3, shear waves are not evident in the data set chosen, and any residual contribution will be taken into account as systematic error. The waveforms are processed as explained in 5.3.2. The number of points $N_{bin}$ in each bin for the computation of the mean waveform (see equation 5.24) is chosen to be equal to the number of pulses $N_p$. The energy of a waveform $E_{S+N}$ is calculated in the time domain, summing the squared amplitudes of the samples. This includes both the signal and a noise contribution which needs to be later subtracted. The error on the energy $\sigma_{E_{S+N}}$ is obtained by propagation of the standard error over the samples of the mean waveform:

$$E_{S+N} = \sum_{k=1}^{N_w} A_k^2 \tag{5.40}$$

$$\sigma_{E_{S+N}} = \sqrt{\sum_{k=1}^{N_w} (2\, A_k\, \sigma_{A_k})^2} \tag{5.41}$$

where $N_w$ is the number of samples in the mean waveform, $A_k$ is the amplitude of the sample $k$ of the mean waveform, and $\sigma_{A_k}$ is the error on $A_k$.

Given a combination hole-channel (meaning: given the waveforms recorded from one channel when the pinger was at the same depth as the sensor in one hole), the high quality one-pulse obtained from the full waveform is used to calculate the energy $E_{S+N}$ and the relative error applying the equation 5.40. An example of waveform including signal and noise is shown in Figure 5.18(a).

The noise energy $E_N$ and its error are calculated using the data recorded immediately before and after the pinger operation: the energies of 10 noise-waveforms equally distributed in the time are averaged. This data has been verified to be very stable over the time and independent of the hole. An example of noise waveform is shown in Figure 5.18(b). The noise energy is therefore subtracted to estimate the signal energy:

$$E_S = E_{S+N} - E_N \tag{5.42}$$

A particular treatment has been applied to all the energy values for Hole 37, for which the number of acoustic pulses $N_p$ in the 18-s raw data (as defined in equation 5.19) is lower due to the lower repetition rate at which the pinger was operated. The calculated energy values have been rescaled to take into account that [76]:

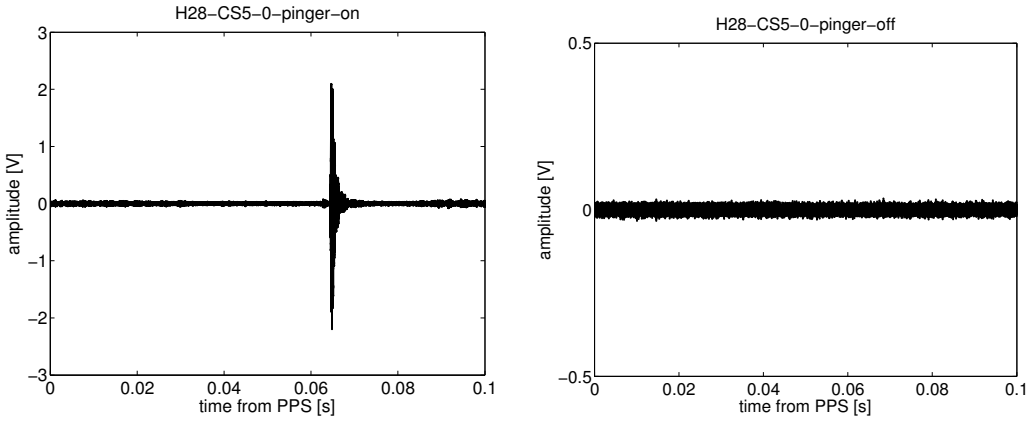


(a) (b)

Figure 5.18: Example of waveforms recorded by one channel before and during pinger operation. Notice the difference in the amplitude scale.

- In an 18 s raw data recording for Hole 37, there are fewer pinger pulses than in other holes ($N_p|_{37} < N_p|_{5,19,28}$). When the 18 seconds are averaged, the rms-noise scales in amplitude as $1/\sqrt{N_p}$, in energy as $1/N_p$.
- After the average is performed, the mean waveform of Hole 37 will be longer than those for Hole 5, 19, 38, therefore the energy calculated by integration over the $N_w$ samples (of the averaged waveform) will be different. Since $N_w$ is proportional to $1/f_{rep}$ (see equation 5.28), the energy integrated scales as $1/f_{rep}$.

Combining the two factors:

$$\begin{aligned} E_{37} &= \frac{1/N_p|_{37}}{1/N_p|_{5,19,28}} \cdot \frac{1/f_{rep}|_{37}}{1/f_{rep}|_{5,19,28}} \cdot E_{5,19,28} = \\ &= \frac{180}{144}\frac{0.125}{0.1} \cdot E_{5,19,28} = \\ &= \left(\frac{10}{8}\right)^2 \cdot E_{5,19,28}. \end{aligned} \tag{5.43}$$

A simple cut is applied to select values with positive energy $E > 0$. Next, from the energy, we need to define a variable which can be treated as an amplitude, in order to fit directly the *amplitude* attenuation coefficient in equation 5.30 rather than the *energy* attenuation coefficient. We therefore define the "effective amplitude" as:

$$A = \sqrt{E}. \tag{5.44}$$

At this point, since the distances between sensor and pinger are known and the effective amplitudes are defined, the values of the $y$ variable of equation 5.30 can

be calculated. The overall uncertainty on the $y$ variable is the same as in equation 5.33 and needs to be estimated before fitting the data. The statistical uncertainty of the effective amplitude is determined with standard error propagation:

$$\sigma_A = \frac{\sigma_E}{2\sqrt{E}} \;\rightarrow\; \frac{\sigma_A}{A} = \frac{1}{2}\frac{\sigma_E}{E}. \tag{5.45}$$

To estimate the systematic error, different methods have been tried. A first attempt was to use the difference in energy between data recorded by one single channel while the pinger was stopped at the same depth on the way down and on the way up in the same hole. Usually, between two and four runs are available for each channel. If there were no systematic effects, the energy of these waveforms should be the same. The first moment distribution of the effective amplitude normalized to the mean value has been calculated for each hole-channel combination, in a similar way to what has been done in equation 5.36:

$$\frac{\sqrt{E_{run}^{hole-channel}} - \left\langle \sqrt{E^{hole-channel}} \right\rangle}{\left\langle \sqrt{E^{hole-channel}} \right\rangle}. \tag{5.46}$$

The histogram of the values so calculated for all the points is shown in Figure 5.19, together with the corresponding Gaussian fit, which gives $\sigma \approx 6\%$, while $rms \approx 10\%$. It must be noticed that due to the normalization applied to each entry in the histogram, the width of the distribution defined by equation 5.46 takes into account only the uncertainties related to a difference in the pinger depth in stops at the same level of the pinger. Such a normalization is chosen to combine the information from multiple holes and channels, but implies that:

- Systematic uncertainties between two holes (for example: systematic variation of the pinger stopping depth from one hole to another, or residual azimuthal variation of the sensor sensitivity) are not taken into account. To include hole-to-hole variations in this kind of estimation for the systematic uncertainty is very difficult since the signal energy from hole to hole depends on the attenuation coefficient, which is an unknown parameter.
- Any possible contribution of shear waves is not taken into account, since we normalize to the energy recorded (which includes itself shear wave contribution, if present).

To estimate the systematic uncertainty, an alternative method, which consists in the analysis of the distribution of the "pulls", has been considered. The pulls are in the present case the difference between the data and the fitted value, normalized to the statistical uncertainty:

$$\frac{y - y_{fit}}{\sigma_y|_{\sigma_{sys}=0}} \tag{5.47}$$

where $\sigma_y$ includes the statistical variation of the mean waveform samples and the (negligible) error on the distance (as specified in equation 5.33 assuming $\sigma_{sys} = 0$).

However, if the *amplitude* is assumed to follow Gaussian statistics, then $y$, which is the logarithm of the amplitude, is not a Gaussian variable. Moreover, $\sigma_A/A$ decreases with distance (since naturally the amplitude of the signal $A$ decreases at larger distances), so this distribution has not a straightforward interpretation.

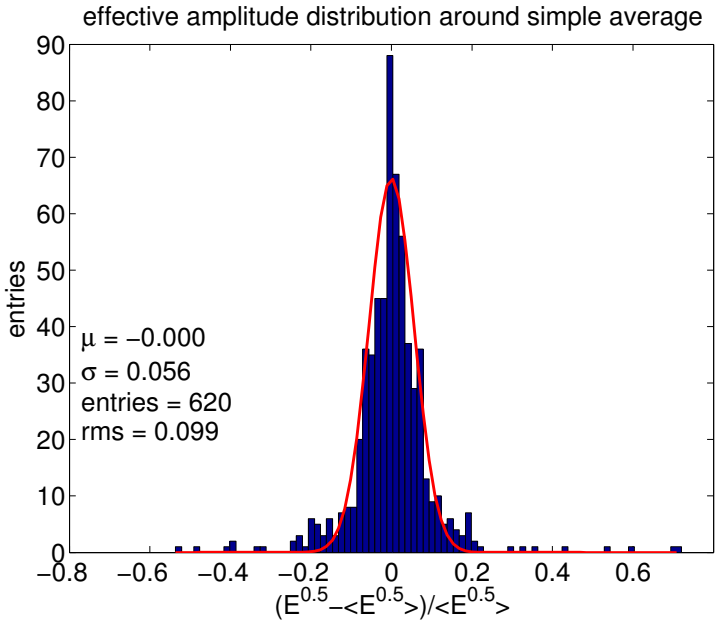


Figure 5.19: Distribution of the differences between effective amplitudes as calculated in the energy attenuation analysis from full waveform (see equation 5.46). The histogram shows the fluctuations between the values obtained for each channel when the pinger stopped in each hole.

Since no better way to estimate the systematic uncertainties has been found, we can still make some additional considerations by looking at the quality of the fit. For each channel, the effective amplitude values calculated in multiple runs taken at the same distance are kept separated (and not averaged to one value) to keep visible any eventual systematic difference for measurements in the same hole. Statistical and systematic errors are added as shown in equation 5.33 to each data-point. As systematic error, we first assume a value of 6%, independent of the distance, as estimated in Figure 5.19. The data from each channel are fitted performing the linear regression of equation 5.30 (following [75], see also [69]). Prior to performing the fit, it is required that there are at least three values of energy which pass the cut $E > 0$ (so that the number of degrees of freedom of the fit $n_F$ is at least 1). This requirement is fulfilled by all channels except DS4-2 (HADES). The reduced chi-square values $\chi^2/n_F$ for the 48 available channels are displayed in Figure 5.20 and show that generally the assumed error is underestimated ($\chi^2/n_F$ too large), as expected from the previous considerations.

If the systematic error used in the fitting procedure is enlarged, the $\chi^2/n_F$

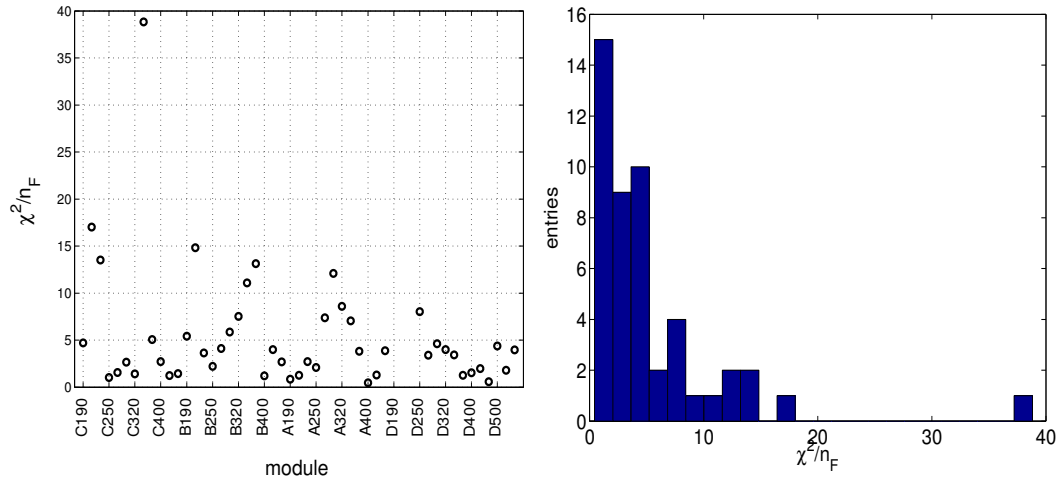


(a) (b)

Figure 5.20: Reduced chi-square distribution $\chi^2/n_F$ for the full waveform energy analysis method: the data of each channel have been fitted assuming a systematic error of 6%. In (a) the values are listed measurement by measurement; in (b) the corresponding distribution is shown.

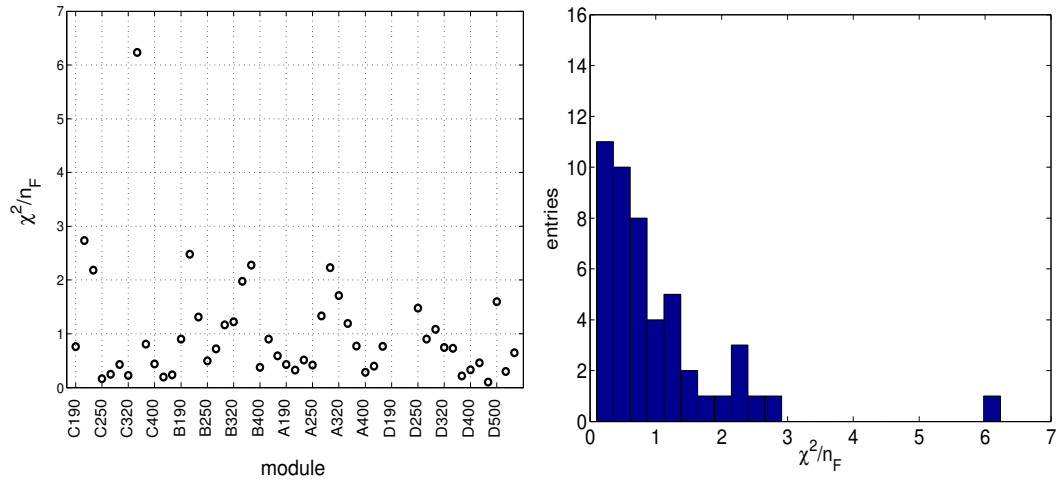


(a) (b)

Figure 5.21: Reduced chi-square distribution $\chi^2/n_F$ for the full waveform energy analysis method: the data of each channel have been fitted assuming a systematic error of 15%. In (a) the values are listed measurement by measurement; in (b) the corresponding distribution is shown.

decreases. Of course, if a too large error is used (for example 20%), the $\chi^2/n_F$ drops strongly below 1 showing that the error becomes overestimated. This behavior suggests that an intermediate value should be assigned to the error: we choose a value of 15%, which gives a mean value of the $\chi^2/n_F \approx 1$. It must be said that any reasonable value assumed for the systematic uncertainty does not affect significantly the final result. The reduced chi-square $\chi^2/n_F$ obtained using 15% as systematic uncertainty is shown for each of the available channels in Figure 5.21.

An example fit obtained including both statistical and a 15% systematic error is illustrated in Figure 5.22. All the fits for all the channels are presented in Appendix A.

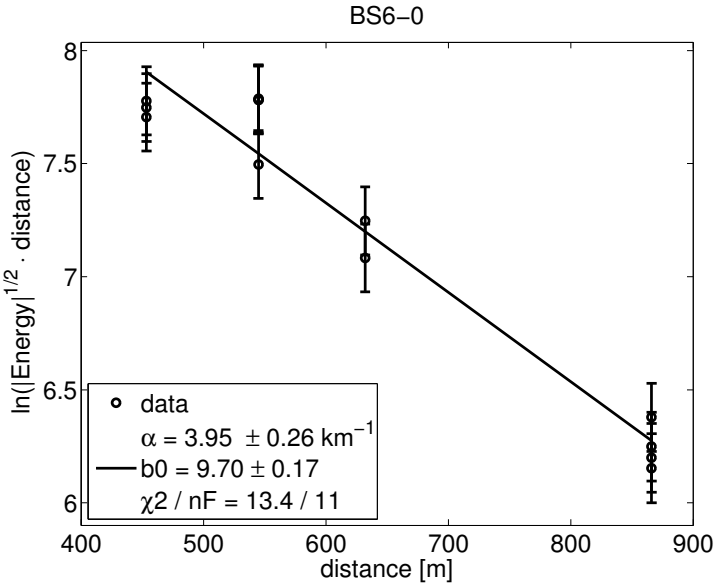


Figure 5.22: Example fit of effective amplitude vs. distance for one channel.

The values obtained for the attenuation coefficient for each channel are plotted in Figure 5.23. The strings have been sorted by average distance from the pinger holes and, within each string, the modules have been sorted from the shallower to the deeper level. Some points need to be made: on the one hand the measurements and the corresponding errors are not compatible with a model where the attenuation coefficient is described by a constant. The result could be interpreted in multiple ways:

- The attenuation could be different depending on the local properties of the ice at the measurement location.

- There could be other systematic uncertainties which we are not able to identify.

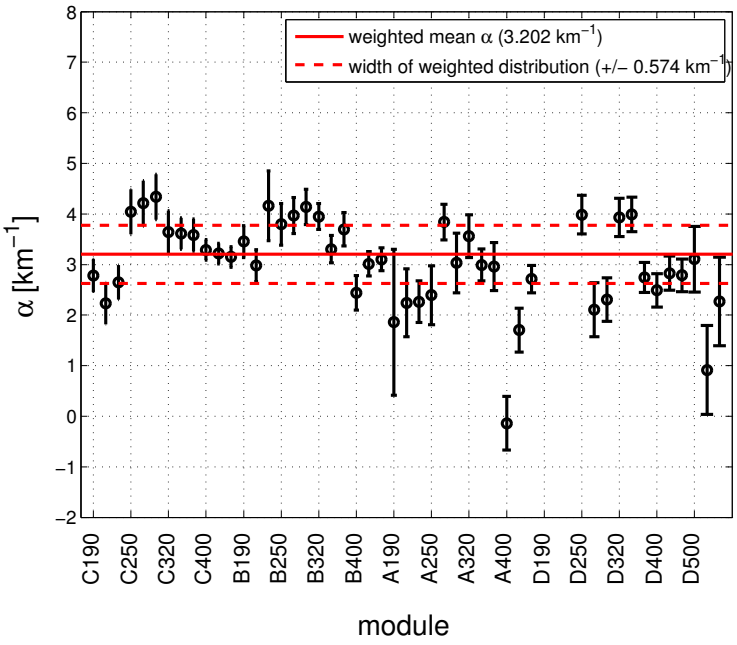


Figure 5.23: Attenuation coefficient and corresponding error obtained in the time-domain energy analysis of the full waveform for each measurement.

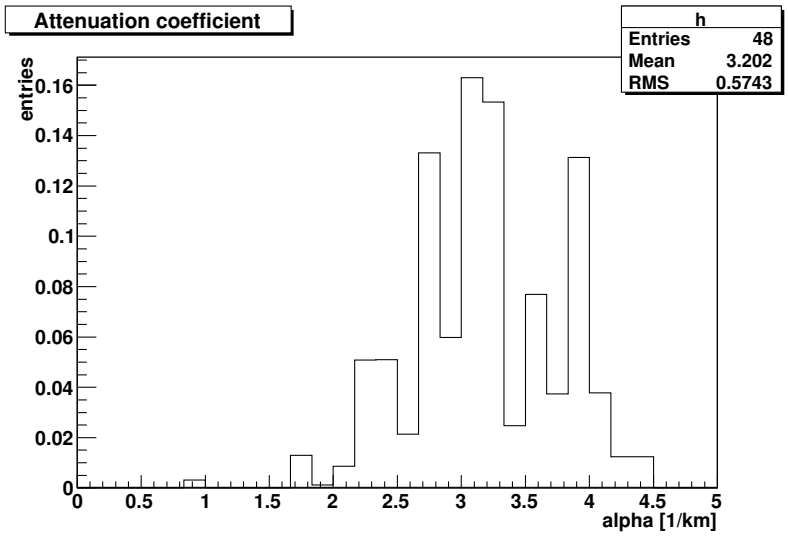


Figure 5.24: Weighted histogram of the values for the attenuation coefficient obtained in the time-domain energy analysis using the full waveform recorded.

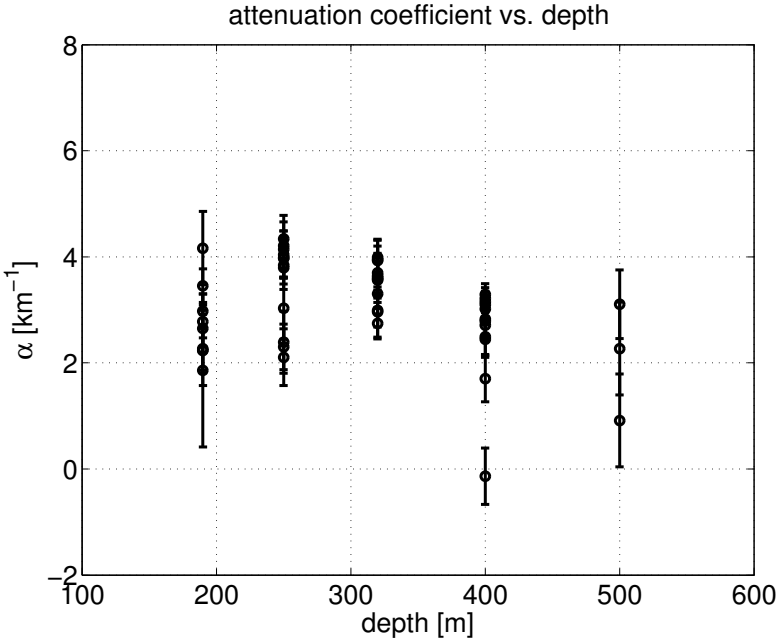


Figure 5.25: Attenuation coefficients and corresponding errors vs. depth, obtained in the time-domain energy analysis using the full waveform.

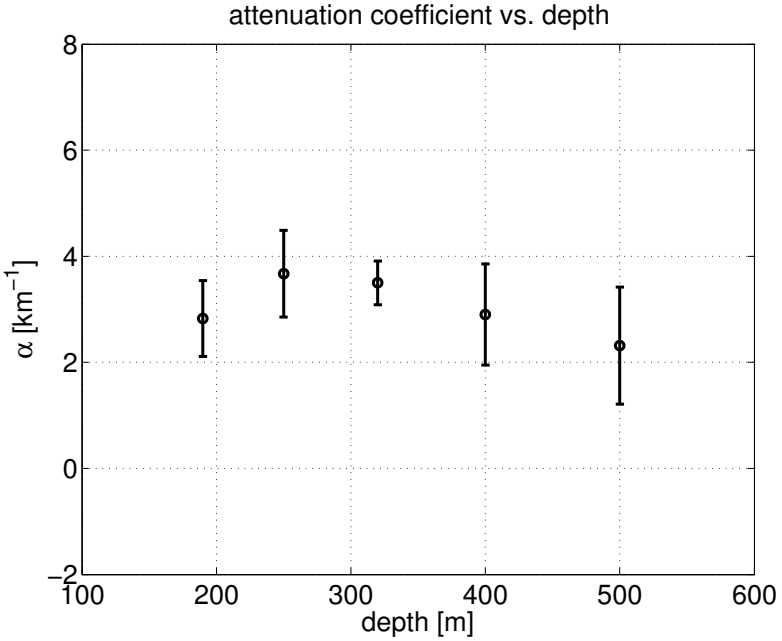


Figure 5.26: Weighted mean and corresponding error of the attenuation coefficients of Figure 5.25 as a function of the depth.

On the other hand, it is clear that the attenuation coefficient is well-constrained by the measurements, and a certain range for this parameter can be specified. To do this, we make the weighted histogram of the values, using for each entry the following weight:

$$w_i = \frac{\frac{1}{\sigma^2_{\alpha,i}}}{\sum_i \frac{1}{\sigma^2_{\alpha,i}}} \tag{5.48}$$

where $\sigma_{\alpha,i}$ is the 1-$\sigma$ error on the value of $\alpha$ in the measurement $i$ obtained from the fit. Such a histogram is shown in Figure 5.24. As final result we quote the mean of the histogram as central value and the width of the distribution as error, *i.e.*:

$$\langle \alpha \rangle = 3.20 \pm 0.57 \text{ km}^{-1} \tag{5.49}$$

which translates into:

$$\langle \lambda \rangle = 312^{+68}_{-47} \text{ m}. \tag{5.50}$$

A depth dependence has been hypothesized and investigated but no clear result has been found: the distribution of the values found versus depth is shown in Figure 5.25; their mean values with the corresponding errors, obtained by weighted mean (using the same weights as in equation 5.48), are shown in Figure 5.26. If a constant is fitted for $\alpha$ vs. depth, the reduced chi-square is found to be $\chi^2/n_F = 172/47$. If a linear fit is performed, the reduced chi-square is found to be $\chi^2/n_F = 165/46$.

### Time windows

Another algorithm was applied to the same data, based on a different definition of noise and signal energy by time windows.

The preparation of the waveforms is performed in the usual way (drift, wrap, average) as described in section 5.3.2. Two time windows, where $P$ and $S$ waves are expected, are calculated from the well known speed of sound. Using the equation 5.40, the energy of the signal is calculated in each window separately (over a number of samples $n_P$ for $P$-waves and $n_S$ for $S$-waves; the remaining samples $n_N$ are used to determine the energy of the noise. This procedure provides $E_P$, $E_S$, $E_N$ and the corresponding errors $\sigma_{E_P}$, $\sigma_{E_S}$, $\sigma_{E_N}$. An illustration of the time-windowing algorithm has been shown in Figure 5.9.

Next, only the energy of $P$-waves is considered. The noise is subtracted rescaling by the window length to calculate a "filtered" energy $E_f$ with the corresponding error $\sigma_{E_f}$:

$$E_f = E_P - E_N \cdot \frac{n_P}{n_N} \tag{5.51}$$

$$\sigma_{E_f} = \sqrt{\sigma^2_{E_P} + \sigma^2_{E_N} \cdot \left(\frac{n_P}{n_N}\right)^2}. \tag{5.52}$$

The procedure has been applied to all runs from one sensor, for all the sensors and all holes from pinger season 2008-2009. Then, the "effective amplitude" is calculated in the same way as described in equations 5.44-5.45.

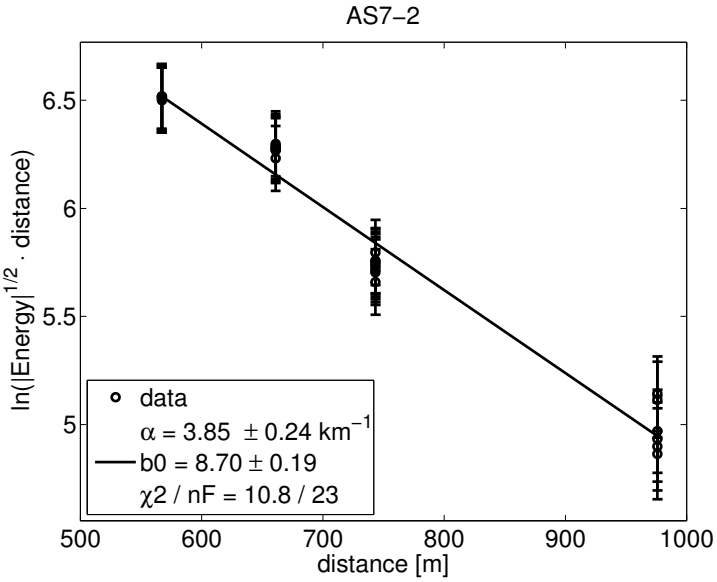


Figure 5.27: Example fit of effective amplitude vs distance for one channel. The calculation of the energy has been done applying the time-windows algorithm, selecting only the contribution of $P$-waves.

From the effective amplitude the variable $y$ is calculated and the linear fit as in equation 5.30 is performed. An example relative to the fit of Channel 2 of the sensor deployed at 400 m depth in String A is shown in Figure 5.27.

The systematic error on the effective amplitude used was 15%. The number of channels which fulfill the requirement of having three or more values of energy $E > 0$ is 48 (only HADES, as before, is excluded). The results from this analysis are consistent with the previous one, as is shown in Figure 5.28; also the $\chi^2/n_F$ values obtained for all the measurements, shown in Figure 5.29, are very similar to the ones obtained applying the analysis on the full waveform. This is expected since both the analyses differ in principle only for the contribution of $S$-waves, which is known to be very small and probably included in the value chosen for the systematic error. The value for the attenuation coefficient obtained by weighted average of the 48 measurements in the same way as before:

$$\langle \alpha \rangle = 3.73 \pm 0.56 \text{ km}^{-1} \tag{5.53}$$

which translates into:

$$\langle \lambda \rangle = 268^{+47}_{-35} \text{ m}. \tag{5.54}$$

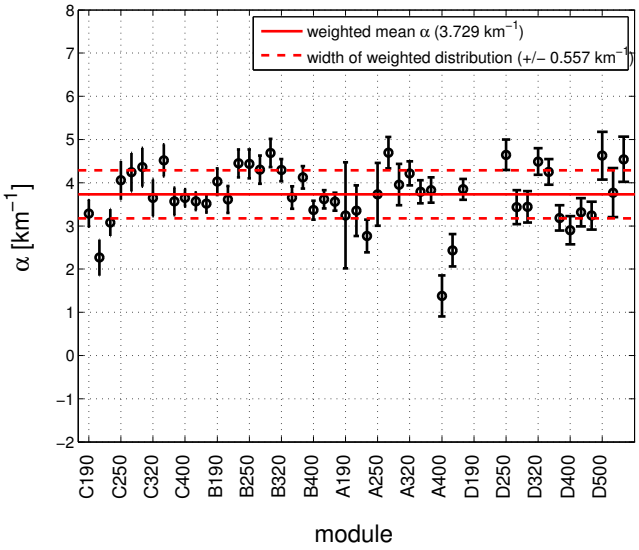


Figure 5.28: Attenuation coefficient obtained by the energy analysis in the time domain with the time-windows algorithm for each measurement, selecting only the contribution of $P$-waves.

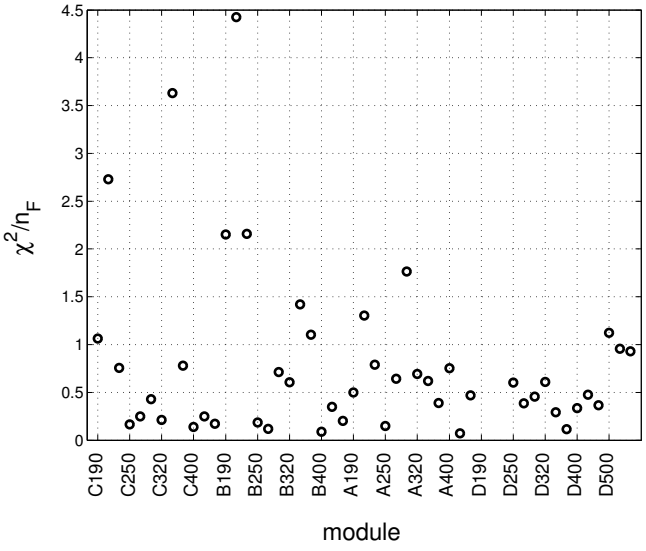


Figure 5.29: Reduced chi-square $\chi^2/n_F$ obtained by the energy analysis in the time domain with the time-windows algorithm for each measurement, selecting only the contribution of $P$-waves.

## 5.4 Attenuation frequency dependence

Another kind of analysis has been performed in order to investigate the possible frequency dependence of the attenuation coefficient.

The same data as in the previous analysis have been selected. All the waveforms recorded by a sensor when the pinger was stopped at the same level of the sensor have been processed as explained in section 5.3.2. Once the averaged waveforms have been obtained, the power spectra, containing signal and noise, have been calculated; an example of a few spectra is shown in 5.30(a).

The noise power spectrum has been calculated from 10 waveforms recorded before and after the pinger operations. These 10 spectra, shown in Figure 5.30(b), have been averaged.

Both the spectra containing noise and signal, and those containing only noise, have been re-binned in bins of 1 kHz or 500 Hz. The mean noise spectrum has been subtracted from the spectrum of each waveform in order to get the pure signal spectrum. The spectra of the signal recorded by CS6-0 for all pinger holes are shown in Figure 5.31.

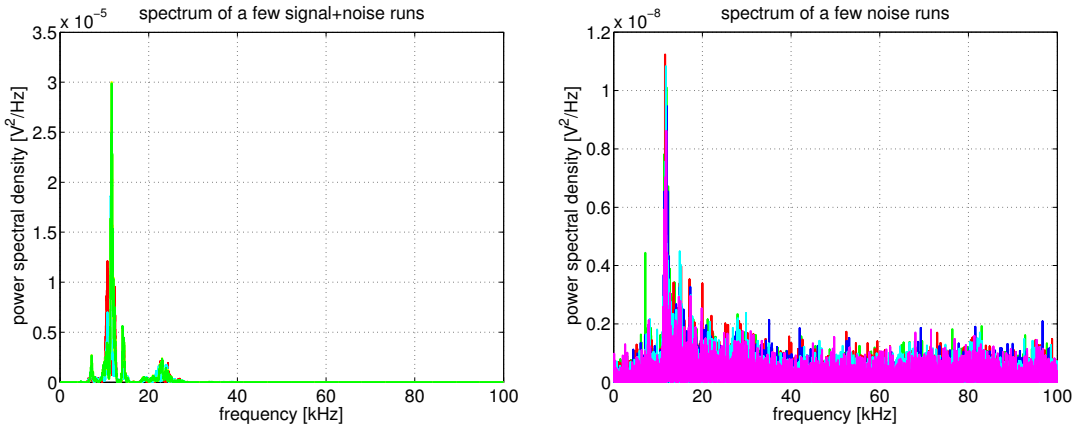


(a) (b)

Figure 5.30: Spectrum of pinger signal plus noise in (a) and noise only in (b). Note the different scale on the $y$-axis.

The spectral content of the pinger signal as recorded by the sensor concentrates in the region between 3 kHz and 30 kHz with a main peak around 12 kHz, as can be seen from Figure 5.31. This spectrum is the result of the folding of:

- Emission spectrum of the pinger: this can be obtained from the convolution of the *Transmitting Voltage Response* (TVR) of the pinger (specified in the data-sheet and shown in Figure 5.32(a)) and the high-voltage pulse (the one shown in Figure 4.12). The result of the mathematical convolution is shown in Figure 5.32(b) [77].

- Sensitivity response of the sensor: this is partially unknown, since it has been proved that the sensitivity spectrum of SPATS sensors has changed after the installation in the ice. Some more details regarding this issue will be discussed in section 5.7.

Two different measurements of the spectrum emitted by the pinger have been recently done in water at Wuppertal University and in water covered by ice at Aachen University. The measurements were done using sensors different from SPATS, and have confirmed that the measured spectrum is the spectrum of the signal emitted from the pinger, more than the spectral sensitivity of the sensor itself. This makes it possible to attempt a study of the frequency dependence of the attenuation. To do so, two regions of interest have been defined: the first between 3 kHz and 17 kHz and the second between 17 kHz and 35 kHz.

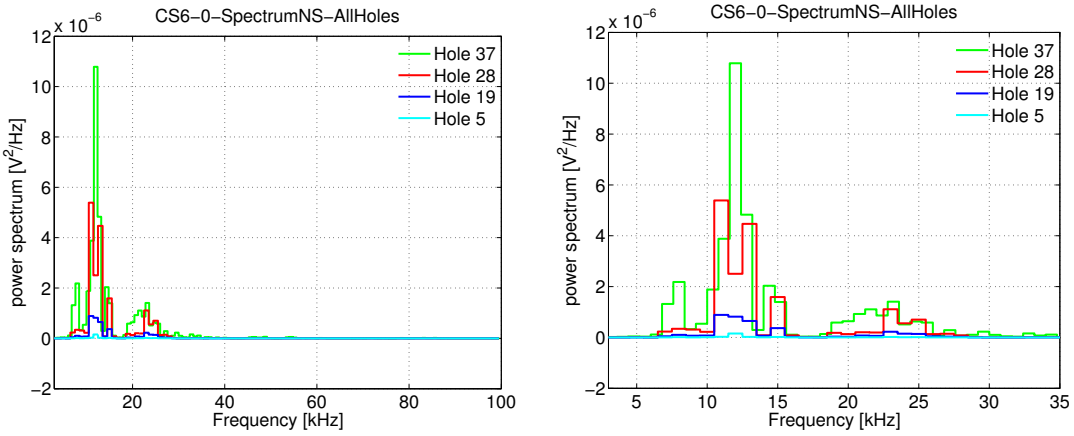


Figure 5.31: Spectrum of the pinger signal after noise subtraction for one example channel and each hole. (b) is a zoom-in view of (a).

The integral of the power spectrum in the two selected frequency bandwidths provides two energy values which are treated separately; the integral of the whole spectrum is also computed to make a comparison with the time domain attenuation analysis. From the energy an effective amplitude is calculated and an attenuation analysis is performed on each set of values, using a systematic uncertainty of 15% on the effective amplitude as in the previous analysis. An example of the three values for one channel is illustrated in Figure 5.33. It can be seen that for this particular sensor channel the fit over the whole spectrum and the one over the low range of frequency ($3 - 17$ kHz) are consistent; the one over the higher frequency range ($17 - 35$ kHz) gives a slightly lower value for the attenuation coefficient but this is not significant.

The analysis has been carried out for the 12 sensor channels of level 6. The resulting attenuation coefficients for the 12 sensor channels in the three frequency

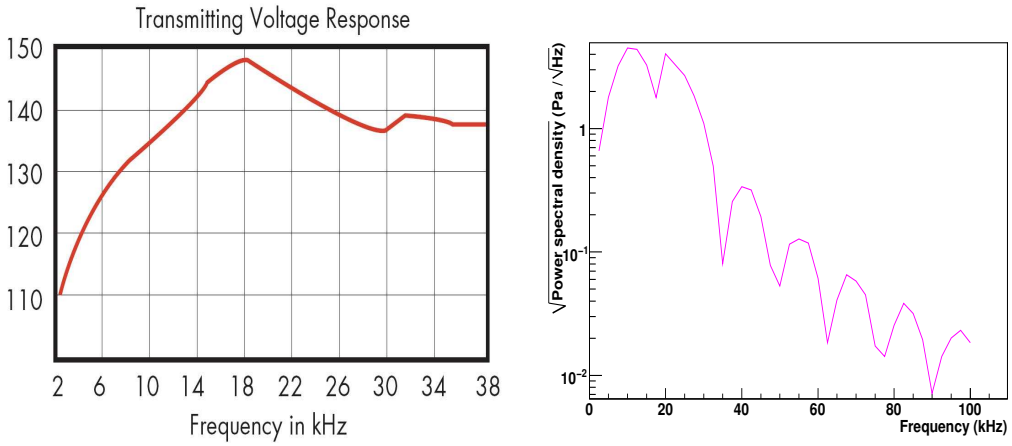


(a) (b)

Figure 5.32: *Transmitting Voltage Response* of the pinger in (a), from the datasheet on www.itc-transducers.com. In (b) convolution of the TVR with the high-voltage pulse applied to the piezoelectric ceramic, shown in 4.12.

ranges are shown in Table 5.5 and in Figure 5.34. In some cases, a lower value for $\alpha$ is obtained for the frequency range between 17 and 35 kHz; however, due to the low signal power in this band, it cannot be excluded that the only remaining contribution is noise, which is of course distance independent (and therefore would result in a flattening of the curve at far distances).

The mean and width of the weighted histogram for the values obtained in the three frequency ranges are:

$$\left\langle \alpha_{[\ 3-17\ \mathrm{kHz}]} \right\rangle = 3.80 \pm 0.44\ \mathrm{km}^{-1} \tag{5.55}$$

$$\left\langle \alpha_{[17-35\ \mathrm{kHz}]} \right\rangle = 3.32 \pm 0.61\ \mathrm{km}^{-1} \tag{5.56}$$

$$\left\langle \alpha_{[\ 3-35\ \mathrm{kHz}]} \right\rangle = 3.76 \pm 0.45\ \mathrm{km}^{-1}. \tag{5.57}$$

In conclusion, no strong frequency dependence of the attenuation is observed in the present data.

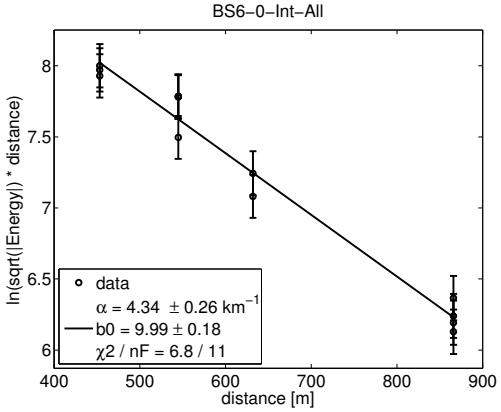


(a) Whole frequency range

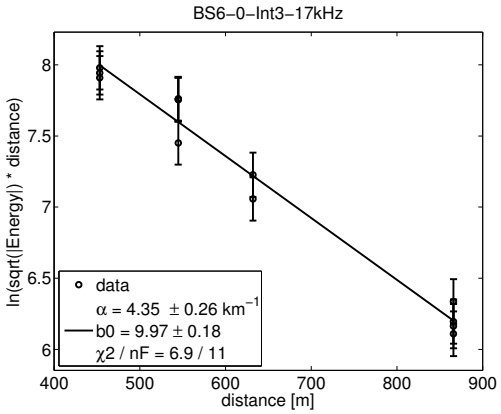


(b) 3-17 kHz

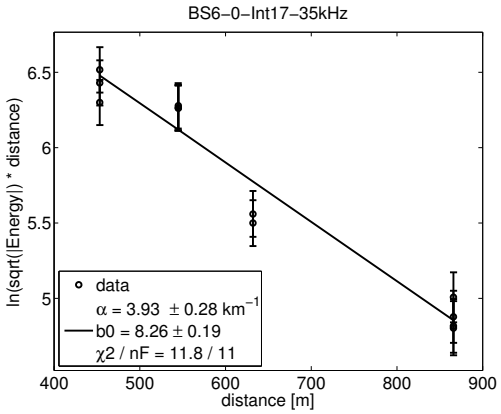


(c) 17-35 kHz

Figure 5.33: Fit of the energy calculated over the whole frequency range in (a), and on the two bandwidths selected: $3 - 17$ kHz in (b), $17 - 35$ kHz in (c).

| sensor channel | $\alpha \pm \sigma_\alpha$[3-17 kHz] | $\alpha \pm \sigma_\alpha$[17-35 kHz] | $\alpha \pm \sigma_\alpha$[whole] |
|---|---|---|---|
| AS6-0 | 3.88 ± 0.31 | 4.84 ± 0.75 | 4.09 ± 0.33 |
| AS6-1 | 3.64 ± 0.28 | 3.57 ± 0.34 | 3.58 ± 0.28 |
| AS6-2 | 3.63 ± 0.34 | 4.23 ± 0.63 | 3.79 ± 0.35 |
| BS6-0 | 4.35 ± 0.26 | 3.93 ± 0.28 | 4.34 ± 0.26 |
| BS6-1 | 3.69 ± 0.27 | 4.15 ± 0.38 | 3.78 ± 0.27 |
| BS6-2 | 4.12 ± 0.28 | 3.97 ± 0.29 | 4.02 ± 0.27 |
| CS6-0 | 3.28 ± 0.26 | 3.13 ± 0.25 | 3.27 ± 0.26 |
| CS6-1 | 3.54 ± 0.26 | 3.41 ± 0.25 | 3.57 ± 0.26 |
| CS6-2 | 3.24 ± 0.26 | 2.70 ± 0.25 | 3.21 ± 0.26 |
| DS4-0 | 4.66 ± 0.33 | 3.07 ± 0.41 | 4.61 ± 0.35 |
| DS4-1 | 4.63 ± 0.36 | 3.00 ± 0.35 | 4.41 ± 0.34 |
| DS4-2 | 3.62 ± 0.30 | 2.23 ± 0.29 | 3.17 ± 0.30 |

Table 5.5: Summary of the results obtained by the energy analysis in the frequency domains on the two selected bandwidths and over the whole spectrum. All the numbers are in [km$^{-1}$].

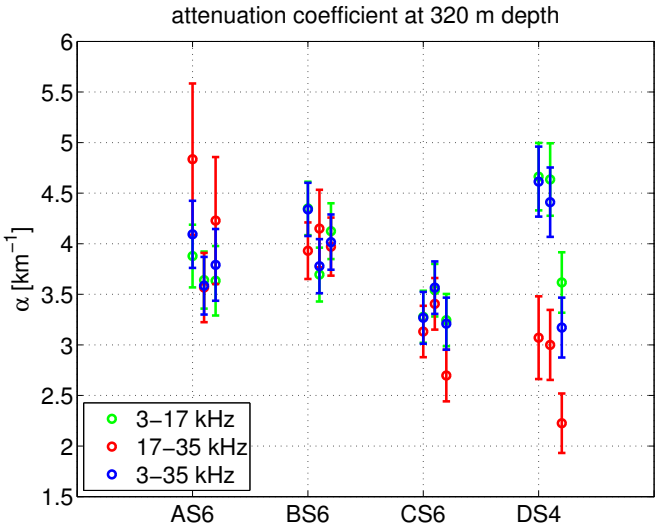


Figure 5.34: Attenuation coefficients obtained from the analysis of the energy in selected bandwidths for all the sensor channels indicated in Table 5.5.

## 5.5 Reliability of the fitting procedure

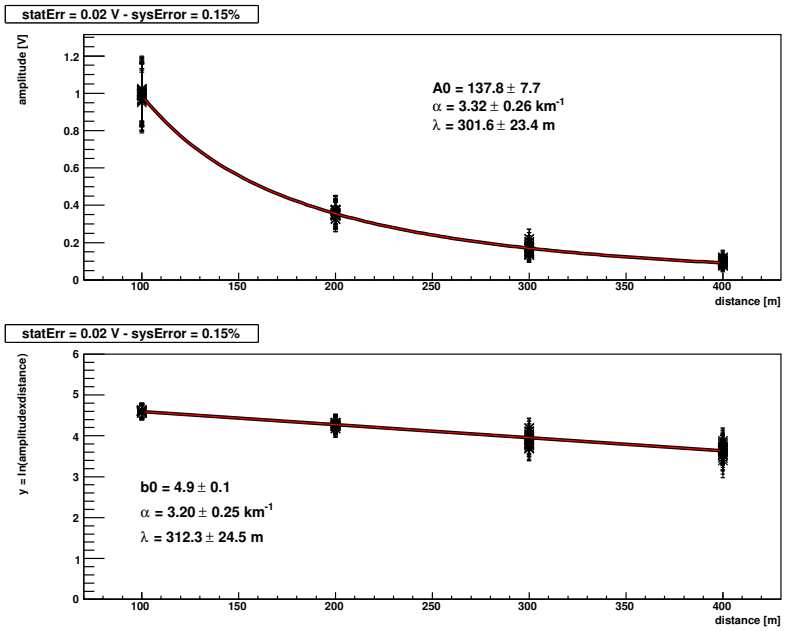


Figure 5.35: Simulation of 40 points and comparison between fit performed using equation 5.29 and 5.30. Above: simulated points and fit performed using the equation 5.30. Below: simulated points and fit performed using the equation 5.29.

The use of the equation 5.30 raises several questions: if the amplitudes are Gaussian distributed, the same cannot be said about the variable $y$. To verify a possible bias of an analysis performed using the linear fitting equation 5.30 instead of the non-linear equation 5.29, a Monte Carlo has been performed. For each of the distances 100, 200, 300 and 400 m, 10 points have been simulated as sampled from a Gaussian distribution with amplitude $A_d$ and $\sigma = 20$ mV (compatible with the actual one), where $A_d$ is defined as:

$$\begin{aligned} A_d &= \frac{A_0}{d} e^{-\frac{d-d0}{\lambda}} \\ A_0 &= 100; \lambda = 300 \text{ m}; \end{aligned} \tag{5.58}$$

which is a variation of the law expressed from equation 5.29. The data has been fitted both directly (by non-linear fit) and transforming the data-points in $y = \ln(A_d d)$ and performing a linear fit, following therefore the procedure used for the attenuation analysis presented above. The result is consistent between the two methods and with the assumed value of $\lambda = 300$ m within the error (see Figure 5.35).

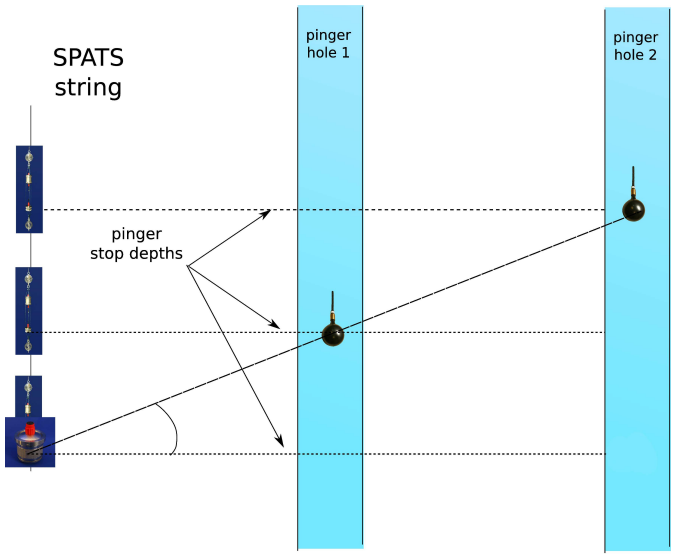


Figure 5.36: Angle between pinger and sensor measured from the equatorial plane of the sensor.

## 5.6 Attenuation coefficient on diagonal paths

In the previous sections, the attenuation coefficient has been measured along an horizontal path between the sensor and the pinger. An attempt has been made to evaluate if the result is different when the analysis is performed over a diagonal path. For each stop of the pinger all the selected sensor were recording. From all the data available, for each sensor we selected the data which were recorded when the pinger was stopped at a depth such that the angle measured between the pinger and the horizontal plane defined by the sensor equator was fixed. A sketch of the definition of this angle, sometimes called elevation angle, is shown in Figure 5.36. The value of this angle is 0 degrees when the pinger is located at the same depth as the sensor.

The selection of data at similar angle was possible for BS7 and BS6 in direction upward, with an angle of $10 \pm 3$ degrees, and for BS5 in direction downward with an angle of $10 \pm 4$ degrees; for BS4 the only possible angle was $7 \pm 2$ degrees. The list of selected stops for each hole for these two sensors is shown in Table 5.6.

| sensor | stop level | H37 | H28 | H19 | H5 | sensor | stop level | H37 | H28 | H19 | H5 |
|---|---|---|---|---|---|---|---|---|---|---|---|
| **BS4** | 250 | 7.5 | 6.3 | 5.4 | x | **BS6** | 190 | x | x | 11.6 | 8.5 |
| **190 m** | 320 | x | x | x | 8.5 | **320 m** | 250 | 8.8 | 7.3 | x | x |
| **BS5** | 320 | 8.8 | 7.3 | 6.3 | x | **BS7** | 190 | x | x | 13.3 | 9.8 |
| **250 m** | 400 | x | x | 13.3 | 9.8 | **400 m** | 250 | x | 8.3 | 7.3 | x |
| | | | | | | | 320 | 10.0 | x | x | x |

Table 5.6: Angles (in degrees) selected for the diagonal attenuation coefficient measurement carried out for the sensors BS5 and BS6 in direction "upward" and for the sensor BS7 in direction "downward".

| **BS4** | BS4-0 | BS4-1 | BS4-2 |
|---|---|---|---|
| horizontal | 3.45±0.31 | 2.98±0.32 | 4.16±0.69 |
| diagonal (down) | 3.80±0.32 | 3.67±0.33 | 2.99±0.78 |
| **BS5** | BS5-0 | BS5-1 | BS5-2 |
| horizontal | 3.80±0.41 | 3.97±0.36 | 4.14±0.35 |
| diagonal (down) | 2.86±0.40 | 3.17±0.34 | 3.07±0.33 |
| **BS6** | BS6-0 | BS6-1 | BS6-2 |
| horizontal | 3.95±0.26 | 3.30±0.27 | 3.70±0.33 |
| diagonal (up) | 3.43±0.34 | 4.18±0.39 | 3.92±0.41 |
| **BS7** | BS7-0 | BS7-1 | BS7-2 |
| horizontal | 2.44±0.34 | 3.01 ± 0.24 | 3.10±0.22 |
| diagonal (up) | 2.57±0.35 | 3.49±0.24 | 3.34±0.26 |

Table 5.7: Comparison between diagonal and horizontal attenuation coefficient measurements for the sensor BS5 and BS6 "upward" and for BS7 "downward". All the values are given in [$km^{-1}$].

The procedure applied is very similar to the one explained in section 5.3.6: the energy of signal and noise has been calculated from the full waveform recorded when the pinger was running, then the noise energy, calculated from the waveforms recorded before and after the pinger runs, has been subtracted.

This has been repeated for each channel for all the distances selected and a linear regression on the variable $y$ defined as in equation 5.30 has been performed. A systematic uncertainty of 15% in effective amplitude has been taken into account as for the previous analyses. The results obtained for each sensor channel are compared to the ones obtained for the horizontal path in Table 5.7 and in Figure 5.37.

Comparing the values, it appears that there is not a unique trend and it is not possible to identify a clear dependence of the attenuation coefficient on the direction. If there are variations, these are very near to a 1-sigma effect, therefore they are not significant. In the near future new measurements of this type, with a choice of stop levels aiming to perform such analysis, will be taken. In the analysis of such data, if a trend is found, a possible variation of the sound emitted by the

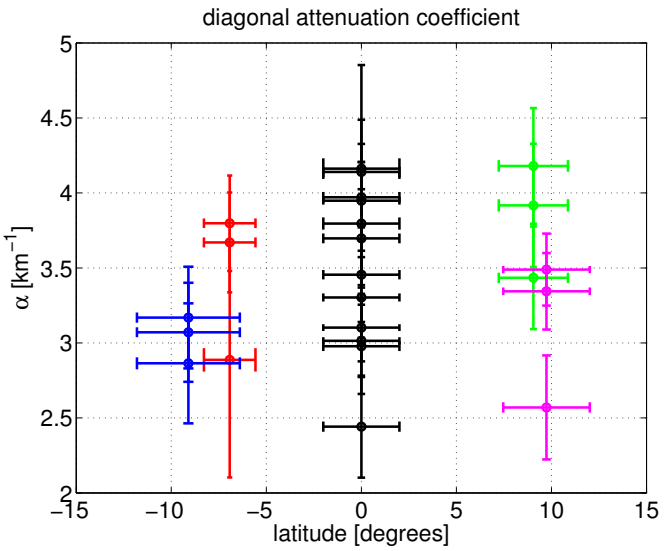


Figure 5.37: Attenuation coefficients for diagonal and horizontal path for the sensor channels indicated in Table 5.7.

pinger as a function of depth must be taken into account.

## 5.7 Calibration

Several attempts have been made to calibrate the SPATS array using the pinger data. From the fit performed for each analysis the value $A_0 = \exp(b_0)$ as illustrated in equation 5.30 has been kept as indicative of the single piezoelectric sensitivity $S_{piezo}$ [V/Pa]. The signal $A_0$ received and recorded (in [V]) depends on the pressure signal $A_0^*$ [Pa] through the sensitivity of the particular ceramic:

$$A_0 = S_{piezo} A_0^*. \tag{5.59}$$

Prior to the deployment, all the sensors of String A, B, C were calibrated in water using a reference hydrophone as described in [73]. The original plan was to correlate the frequency dependent sensitivity in water with the one in ice extracted from the pinger data, to gain information about the change in sensitivity. A first comparison showed that the $b_0$ values extracted from the energy analysis were not compatible with the ones obtained in the water calibration: a clear demonstration is given if a specific sensor, BS6, is considered. This is the sensor from which we have more data, since it was active in transient data taking with two channels (usually one channel per sensor is used) and was never in saturation in pinger data. From the pinger analysis, it is easily found that one of the three channels in the sensor, Channel 0, is between two and three times as sensitive as the other two, as reported in Table 5.8. The three piezoelectric ceramics had instead more

or less the same sensitivity in water, as it can be seen looking at the sensitivity as a function of the frequency illustrated in Figure 5.38.

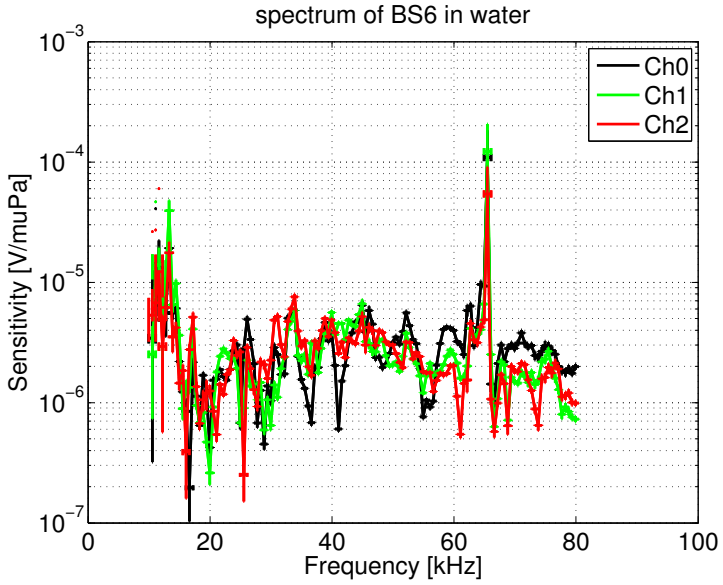


Figure 5.38: Sensitivity vs. frequency measured for one sensor during the calibration in water before deployment.

| Sensor-channel | $b_0$ | $\sigma_B$ | $A_0 = \exp(b_0)$ | $\sigma_{A_0}$ |
|---|---|---|---|---|
| BS6-0 | 9.70 | 0.17 | 16318 | 2774 |
| BS6-1 | 8.67 | 0.18 | 5825 | 1049 |
| BS6-2 | 8.54 | 0.22 | 5115 | 1125 |

Table 5.8: Sensitivity parameters extracted from pinger energy analysis for an example sensor.

It must be clarified that there is a substantial difference between the two data sets: the calibration in water was done rotating the sensor and measuring the signal recorded by the channel in front of the transmitter, while in the case of pinger data the source direction was fixed, and data from the three channels were recorded simultaneously.

It is thus clear that the sensitivity of the piezoelectric ceramics of the same sensor depends on the direction of the signal source. This has been verified crossing the information from different types of data:

- Inter-string runs at the same level have shown that Channel 1 is the most sensitive channel in BS6 [69].

- In the season 2007-2008 the pinger was operating from a direction opposite to the one of 2008-2009; in that angular range, the most sensitive channel was either Channel 1 or Channel 2 [1].
- The energy of the waveform recorded by Channel 0 is about three times as large as the one recorded by Channel 2 if the source of the transient event is located in the region where the pinger was operating in 2008-2009 (for example: transients recorded during the freeze-in process of Hole 37), but it is about the same if the transient source is located in the direction of the array (for example: transients from the Rodriguez well 2007-2008, see [71]).

The conclusion is that a calibration is not possible at present, since the data are not comparable.

## 5.8 Study of polar angle variation of sensitivity

The attenuation length has been measured in this work rather precisely. The value obtained can be thus used in principle as known information in order to gain knowledge about the polar variation of the sensitivity, assuming an attenuation length $\lambda$ isotropic (independent of direction and location). Each sensor took data for each pinger stop, therefore data spanning a wide polar angular range are available. If an attenuation length $\lambda = 300 \pm 50$ m is assumed, it is possible to study, for the same piezoelectric ceramic, the variation of the sensitivity coefficient as a function of the polar angle $\theta$, measured with respect to the horizontal plane defined by the equator of the sensor (plane where the three channels lie).

The relation between amplitude of the recorded waveform and sensitivity coefficient:

$$A_\theta = \frac{A_\theta^0}{d_\theta} e^{-d_\theta/\lambda} \tag{5.60}$$

can be turned into:

$$A_{0,\theta} = A_\theta d_\theta e^{d_\theta/\lambda} = \sqrt{E_\theta} d_\theta e^{d_\theta/\lambda} \tag{5.61}$$

$$\sigma_{A_{0,\theta}} = d_\theta e^{d_\theta/\lambda} \sqrt{E_\theta d_\theta^2 \frac{\sigma_\lambda^2}{\lambda^4} + \frac{{\sigma_{E,\theta}}^2}{4E_\theta} + \sigma_d E_\theta \left( \frac{1}{d_\theta^2} + \frac{1}{\lambda^2} + \frac{2}{d_\theta \lambda} \right)} \tag{5.62}$$

so that the coefficient is expressed in terms of measured (energy) and known variables (distance, attenuation length). The energy of the waveform (with noise subtraction) is calculated for one sensor when the pinger was at the same level as the sensor (in the same way as the previous analysis has been done) and also when the pinger was stopped at another level (*i.e.* at another angle $\theta$). From the

[1] It must be noticed that only the energies of single waveforms have been compared in this case, since due to the instability of the waveforms it is not possible to extract the parameter $b_0$ as it was done using the data from season 2008-2009.

energy values, since we know the distances and we assume a fixed value of $\lambda$, we can calculate the ratios between the sensitivity coefficients in the two configurations $A_{0,\theta}/A_{0,0}$ for each combination hole-sensor and for all the angles available. To use the ratio rather than the absolute value helps to keep small the error which would otherwise depend on the exponential of the distance. The ratio and the corresponding error are calculated as:

$$r = \frac{A_{0,\theta}}{A_{0,0}} = \sqrt{\frac{E_\theta}{E_0}} \cdot \frac{d_\theta}{d_0} \cdot e^{\frac{d_\theta - d_0}{\lambda}}; \tag{5.63}$$

$$\sigma_r = r\sqrt{\frac{{\sigma_{E\theta}}^2}{4E_\theta^2} + \frac{{\sigma_{E0}}^2}{4E_0^2} + \frac{{\sigma_{d\theta}}^2}{d_\theta^2} + \frac{{\sigma_{d0}}^2}{d_0^2} + \frac{{\sigma_{d\theta}}^2 + {\sigma_{d0}}^2}{\lambda^2} + \frac{(d_\theta - d_0)^2 {\sigma_\lambda}^2}{\lambda^4}} \tag{5.64}$$

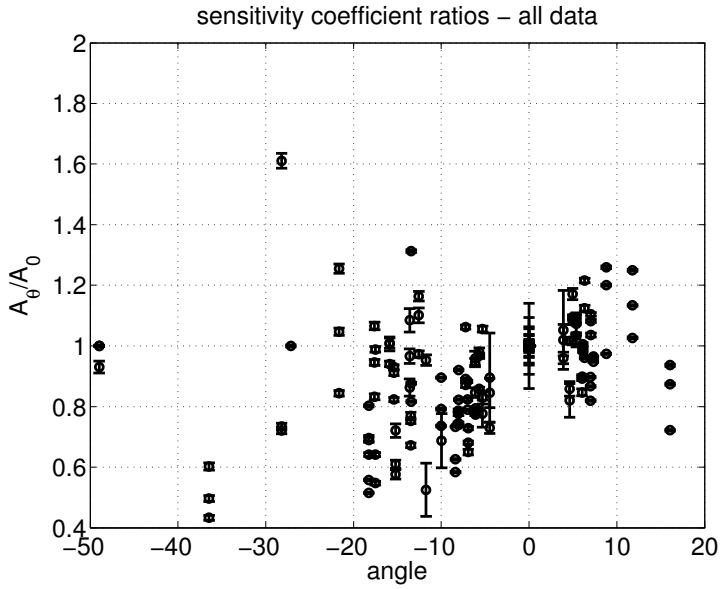


Figure 5.39: Sensitivity variation versuss polar angle for all the sensors installed at 320 m depth obtained by the energy of the waveform when the pinger was in any hole at the depths between 250 and 500 m. The angle, in degrees, is measured from the equatorial plane of the sensor.

The study has been performed on the sensors at level 6, using the data recorded when the pinger was stopped at 250, 400 and 500 m in each of the four holes where the pinger was deployed in the season 2008-2009; the sensitivity coefficient has been normalized, for each hole, to the one obtained from the energy calculation at level 320 m. The plot of the ratio as a function of the angle between source and sensor is shown in Figure 5.39. It can be seen that the variation over an observation angle between $-50$ and $+20$ degrees reaches values of 50%.

| Systematic effect | pinger data | inter-string single level | inter-string ratio | transients |
|---|---|---|---|---|
| Channel-to-channel sensitivity variation | no | yes | no | min |
| Azimuthal sensitivity variation | min | yes | yes | min |
| Polar sensitivity variation | min | no | yes | min |
| Channel-to-channel transmittivity variation | no | no | no | no |
| Azimuthal transmittivity variation | no | yes | yes | no |
| Polar transmittivity variation | no | no | yes | no |
| Interference with reflections from hole back wall | min | no | no | no |
| Water-ice transmission coefficient variation and shear waves production | min | no | no | no |
| Hole ice, cracks, inhomogeneities | min | yes | yes | min |
| Saturation | no | no | no | no |
| Noise, subtracted | no | no | no | no |
| Residual clock drift | no | no | no | no |

Table 5.9: Presence of different systematic effects in various attenuation analysis. "Yes" or "no" means if the effect listed on the left side is present or not in the analysis; "min" means that it is minimally present [71].

## 5.9 Comparison with other attenuation analyses

Independent confirmations of the attenuation coefficient analyses above presented have been obtained using different data sets: transients events and inter-string data. Both these methods suffer from higher systematic uncertainties than the pinger data; a summary is presented in Table 5.9. For a review of each systematic effect see section 5.1.4. These methods are presented in [71]; the inter-string analyses are also presented in more detail in [69] and [78]. Here only a brief summary is shown for comparison with the pinger data analysis.

### 5.9.1 Attenuation from transient events

As it has been mentioned in section 4.1.4, since August 2008 the SPATS array is taking data in triggered-mode. Each of these reconstructed events from natural sound sources is recorded by multiple channels. To use them in an attenuation analysis it is necessary to have some calibration in order to combine and compare data from different channels. An absolute calibration has not been possible yet, as already said; however, a relative calibration has been determined in the pinger energy analysis for one particular direction, in terms of the parameter $b_0$ which is obtained in the linear fit of the variable $y$ (see equation 5.30). The calculated values of sensitivity can be applied as scaling factor for the energy of acoustic pulses coming from the same direction. An interesting set of transient events is comprised of those originating during the freezing process of the holes where the pinger was operated. 13 events reconstructed as coming from the coordinates corresponding to Holes 19, 20 and 28, with a depth around between 230 and 270 m, have been

selected. The waveforms recorded by the sensor channels have been analyzed to get the energy and the corresponding effective amplitude, after a suitable noise subtraction. The calibration factors have been applied and a linear fit has been performed to get the attenuation coefficient. The average value obtained from the 13 events for the attenuation coefficient is [71]:

$$\langle \alpha \rangle = 3.64 \pm 0.29 \text{ km}^{-1}, \tag{5.65}$$

which is compatible with the results obtained from the pinger data analysis.

### 5.9.2 Attenuation from inter-string data

Another completely different analysis has been done in parallel to the one described in detail in this work; instead of the pinger, the frozen-in transmitters have been used as sound sources. The fixed location of sensors and transmitters implies the necessity of combining several sources and/or several receivers in order to perform an attenuation analysis. This adds uncertainty since, as explained before, a calibration *in situ* does not exist.

Two types of analyses have been performed. In the analysis called "single-level direct analysis" (for more details see [69]) the data from one transmitter recorded by all the sensors at the same depth have been used. In this way, there are no systematic uncertainties related to the use of different transmitters. Also, since only sensors at the transmitter depth are used, the polar variation of the transmittivity does not matter. Nevertheless, multiple sensors located at different azimuthal angles with respect to the transmitter are used: therefore the systematic uncertainties related to the use of the unknown sensor sensitivity and to the azimuthal variation of the transmitter transmittivity enter in the analysis of the data. On the side of the sensor sensitivity, an estimate of the variation between all the channels can be obtained analyzing the $b_0$ factor obtained by the energy analysis on a single-channel from pinger data. The histogram of this quantity is represented in Figure 5.40.

The mean values and the standard deviation are found to be:

$$\langle b \rangle = 8.28 \pm 0.98 \tag{5.66}$$

$$\langle A \rangle = e^{\langle b \rangle} \pm \sigma_b e^{\langle b \rangle} = (3.9 \pm 3.9) \cdot 10^3 \tag{5.67}$$

In conclusion, a variation of 100% must be assumed when combining information from more than one channel.

12 transmitters out of 28 were selected applying some quality cuts on the signals recorded. The uncertainty given by the combination of multiple sensors was introduced in the analysis for each of these transmitters and a linear regression on the quantity $y$, the same used in all the previous analysis (see equation 5.30), was performed. The weighted average on the 12 attenuation coefficients gives a value of:

$$\langle \alpha \rangle = 3.16 \ \pm 1.05 \text{ km}^{-1}. \tag{5.68}$$

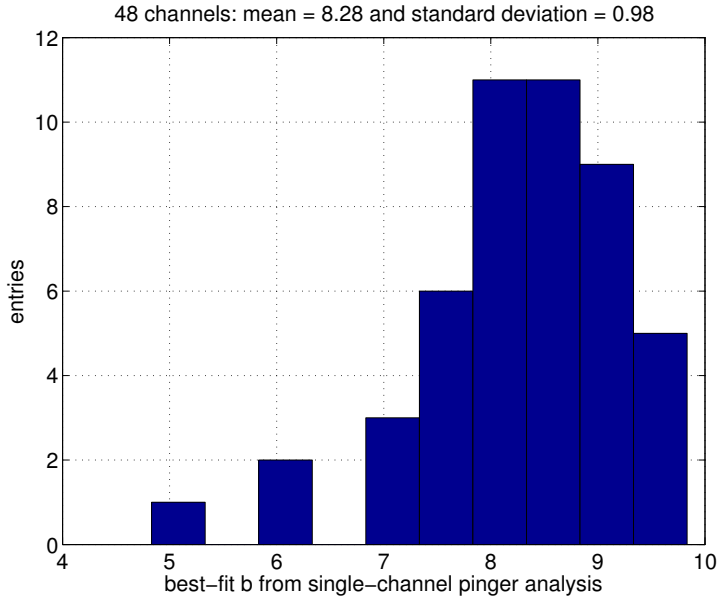


Figure 5.40: Distribution of all the coefficients $b_0$ calculated in single-channel analysis on pinger data.

A different analysis, called "multi-depth ratio analysis" was performed using all the data collected in inter-string run, combining multiple sensors and transmitters at all the distances and angles. This method relies on the idea that if the ratios of signals are used, the different sensitivities and transmittivities cancel out. This would in principle be true if there was no additional dependence of each of them on the angle; since in reality the sensitivities and transmittivities are angle dependent, large systematic uncertainties remain in this analysis. More details regarding the method are presented in [65] and regarding the analysis in [78]. The attenuation coefficient determined using this method is:

$$\alpha = 4.77 \pm 0.67 \text{ km}^{-1}. \tag{5.69}$$

### 5.9.3 Summary of the attenuation analyses

A summary of the results obtained from different analyses is shown in Table 5.10. As far as the pinger data analysis, we decide to quote as final result the one from the analysis of the energy of the full waveform, for the following reasons:

- the number of combinations to which the analysis can be applied is higher than the first peaks analysis;
- compared to the time-windows method, the full waveform analysis technique is fully automatized, which reduces the influence of human choice on the final result.

| Attenuation analysis | number of measurements | $\alpha$ [km$^{-1}$] | uncertainty [km$^{-1}$] | type of uncertainty |
|---|---|---|---|---|
| PINGER energy time domain | 48 | 3.20 | 0.57 | width of weighted distribution |
| INTER-STRING energy single-level | 12 | 3.16 | 1.05 | standard error of weighted mean of the distribution |
| INTER-STRING energy multi-depth ratio | 1 slope | 4.77 | 0.67 | standard deviation of the distribution |
| TRANSIENTS | 13 | 3.64 | 0.29 | standard deviation of the distribution |

Table 5.10: Summary of the results obtained from different methods used to determine the attenuation.

## 5.10 Theoretical models

Several hypotheses are currently under investigation to explain why the attenuation length measured is 20-30 times shorter than the predicted one in [58] [47]. Recently data from an ice core drilled in 2002 at 89 degrees latitude (the *South Pole Remote Earth Science and Seismological Observatory* SPRESSO core [79]) have become available. On the one hand, the grain sizes are significantly larger than those assumed in [58] and [47], and result in an increased value of Rayleigh scattering from grain boundaries. On the other hand, data on dislocation densities in ice sheets have led to a reevaluation of the absorption of energy by dislocations set into vibration by an acoustic wave. The current view is that at depths down to 500 m, dislocation damping is the main contribution to acoustic absorption, and scattering from grain boundaries may become important at the upper end of the frequency interval for which the attenuation has been measured in this work [80].

Another explanation could be the existence of a layering structure in some directions in South Pole ice. This is a known feature with respect to the optical properties, and it has always been believed to be unimportant for the much longer acoustic wavelength. But if the change in "dust concentration" implied a small change in the density and therefore in the medium impedance (see equation 5.7), then one could assume that the integrated effect over all the distance would change significantly the overall refraction coefficient.

A new investigation will be done *in situ* in the next austral summer 2008-2009: a pinger running multiple frequencies will be deployed in three other IceCube holes. This will hopefully provide the data necessary to investigate the variation of the attenuation coefficient in different frequency bandwidths in more detail. In the case of scattering, a strong dependence of $\alpha$ on the frequency of the signal is indeed expected. In addition, the pinger will stop at shallower depths in order to search for a possible depth dependence, and at deeper depths along a fixed polar angle as

measured from a selected sensor (as defined in section 5.6), to test for a possible layering structure. Knowledge about frequency and depth dependence would tell us the relative importance of the physics mechanisms causing the attenuation length to be as short as measured.

# Chapter 6

# Pressure and temperature calibration

## 6.1 Introduction

To study the feasibility of neutrino acoustic detection in South Pole ice other parameters must be studied in addition to the attenuation length, such as for example the sound speed profile, the background noise level and the transient background features.

The sound speed profile determines the refraction, which must be understood in order to reconstruct correctly the emission origin of the pancake [69] [13].

The ambient noise defines the minimum signal which can be discriminated from the noise, and sets therefore a threshold for the energy of the events which can be detected.

The calculation of the noise level in terms of energy is a difficult task, correlated with a major problem concerning glaciophones deployed in South Pole ice: the difficulty to make a calibration before the deployment in conditions similar to those which exist *in situ*.

No method has been developed to date to measure the variation of the sensor response simultaneously at high pressure, at low temperature, and in ice. The only chance is to test it under each condition at a time, assuming that the sensitivity behavior under coupled conditions can be extrapolated from the one under each separate condition.

In this chapter some of the tests which were done to study the behavior of SPATS sensors under high pressure and low temperature are presented and discussed.

## 6.2 Pressure test

During the deployment at the South Pole, the sensors are exposed to the pressure given by the water column in the borehole, which reaches the maximum value of

50 bar for a depth of 500 m. From the data on the temperature recorded by the thermocouples installed in the acoustic stages and from previous measurements taken by AMANDA [63], it is known that the re-freezing process starts from the top and proceeds towards the bottom of the borehole. The pressure is therefore expected to increase due to the confinement of the water volume under the growing ice, until the strain is released and equilibrium is reached between the hole-ice and the bulk ice. There is no knowledge about the time needed for the whole process to happen, and no measurement of the final pressure on the sensors has ever been possible. A study regarding the features of the hole-ice has been carried out in [81].

The goal of the test described in the following sections was to verify an eventual variation of the SPATS sensor sensitivity under high static pressure.

### 6.2.1 Description of the setup

Figure 6.1: External view of the vessel used for the pressure test, with the moveable cap equipped with feed-through cables.

The experiment was done in the Angstrom Labs at the Uppsala University, where a pressure vessel is available. The experiment was repeated twice, in August 2008 and February 2009, with two SPATS sensors, in analogous conditions. The vessel has an inner diameter of 405 mm and outer diameter of 800 mm, and it is made of two hemispherical halves of a steel alloy, each with a weight of about 500 kg. The upper half of the vessel can be removed or placed in position with the help of a pulley. The lower part sits on a stack of three standard 80 $\times$ 120 cm$^2$ pallets.

To close the vessel, the two parts are placed one on top of the other, with the 24 green bolts visible in the Figure 6.1 going through both. Each bolt, which has a diameter of 40 mm, is secured in place by two nuts, above and below the two vessel hemispheres. An hydraulic tensioner system is used to screw each upper nut and to tighten the bolts so that the vessel is locked tightly enough to hold the internal pressure. A tension force corresponding to 400 bar was used to close the vessel in our test, in which a pressure of 100 bar was forced internally and exerted on the sensor located inside. An internal O-ring assures no leakage once the vessel is closed.

The upper half of the vessel is equipped with an extractable cap. The cap has an additional O-ring and two double sets of feed-through cables which allow for

four sensors and/or emitters to be used inside the vessel.

In our experiment, one SPATS sensor was located inside the container, on an aluminum plate which was designed to keep it at the center of the volume and at about a half of the height of it (which is roughly 330 mm). A picture of the internal setup is visible in Figure 6.2. A system of rubber washers and plastic supports on the plate was used to guarantee the decoupling of the housing from the plate and from the vessel walls, both electrically and mechanically. A mixture of water and oils, suited to lubricate the system, was used to fill in the vessel after the installation and was the medium for the test. The power for the sensor preamplifier board was provided by a power supply located outside. The three differential channels were read out by a data acquisition card from National Instruments (*Ni DAQPad-6070E*), the same used for the pinger emitter tests described in Chapter 4.

A general-purpose transducer (the SQ09, described in Chapter 4) was used for all the measurements, pressed against the vessel external wall in a fixed position by two thick rubber bands. In the second round of measurements the transducer was placed inside a special steel adapter having a concave cylindrical surface capable of sticking to the vessel lateral side and assuring a smooth surface contact between emitter and surface. The transmission of the sound was realized purely by the mechanical connection. Ultrasonic gel was found not to be useful since its rapid change of properties caused a fast variation in the coupling during the measurements.

Figure 6.2: View of the internal setup used for the pressure test.

The location of the transmitter outside the vessel was dictated by two considerations: the first was to exclude any possible variation of the recorded signal due to a variation of the emitter transmittivity. Indeed, even if the used transducer is specified to work up to 2500 m depth, no data regarding any possible variation of the spectral response or of the transmittivity are available. The second was to avoid the presence of reflections and resonances, which are likely to appear due to the liquid medium and the small volume. If these phenomena had appeared during the measurements (for example due to an increase of the sensor sensitivity at increased pressure), it would have been necessary to change the pulse rate or the pulse amplitude to bring the signal to an optimal level; the variation of the input parameters would have made the interpretation of the data more difficult.

On the other side, the choice to set the transmitter outside implies that the

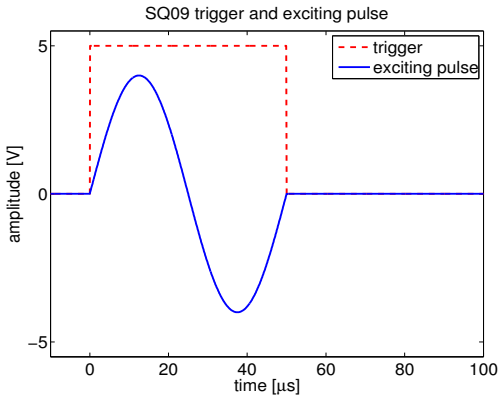


Figure 6.3: Trigger in TTL logic and electrical pulse (amplitude is an example) used to excite the transmitter.

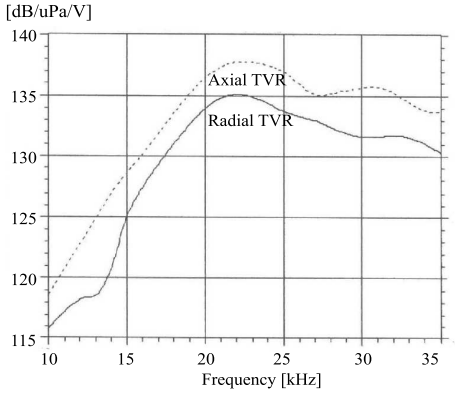


Figure 6.4: *Transmitting Voltage Response* for the transducer SQ09, from the website of the company www.sensortech.ca.

vessel wall is necessarily between source and receiver, modifying the acoustic pulse which is transmitted through the whole vessel to the inner liquid and ultimately to the sensor. This adds some unknown systematic effects when the transmitter is moved to another position or replaced. The vessel has a quite complex structure, with large vertical holes every few centimeters on the perimeter, through which the bolts fit. It is therefore plausible that the efficiency of the transmitter coupling to the internal medium changes from one position to another.

To overcome all these partially unmeasurable effects, many sets of measurements were done keeping the transmitter in a fixed location and observing the variation of the peak-to-peak voltage as a function of the pressure for a fixed input pulse.

### 6.2.2 Data taking and measurements

The electrical pulse used to excite the transmitter was a single-cycle gated sine wave pulse with a central frequency of 20 kHz. The pulse type is shown in Figure 6.3. The pulse was repeated every 50 or 100 ms. Since the pulse is short, the whole band of the transmitter response function is excited. This, as shown in Figure 6.4, has a dominant component between 20 and 25 kHz. The spectrum of the recorded waveform (which is therefore the product of transmitted spectrum, "vessel transfer function" and frequency response of the sensor) is shown in Figure 6.5, together with the signal directly sampled in the time domain for a run taken at 40 bar. The presence of the transmitter signal is visible in the peak at about 25 kHz, as expected from the calibration data provided by the company.

The *Ni-DAQ* has a maximum sampling frequency of 1.25 MHz. Since the three channels of one sensor were sampled simultaneously the real sampling frequency

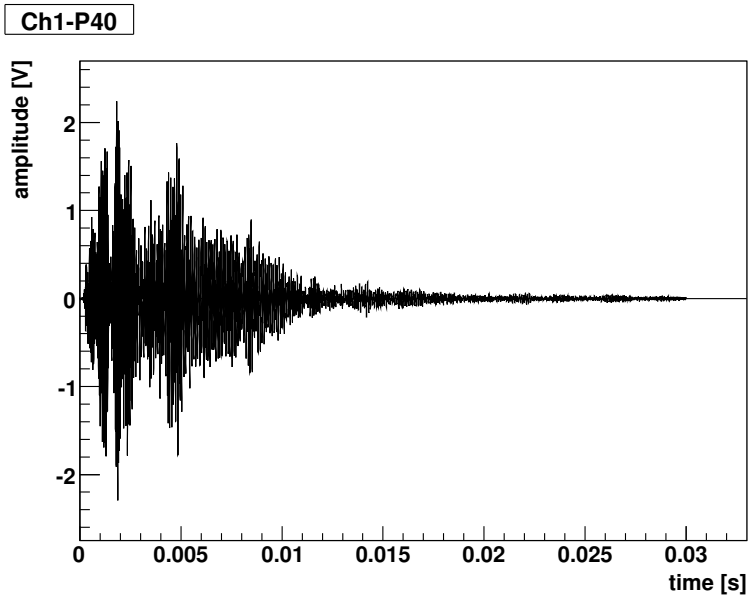


(a)

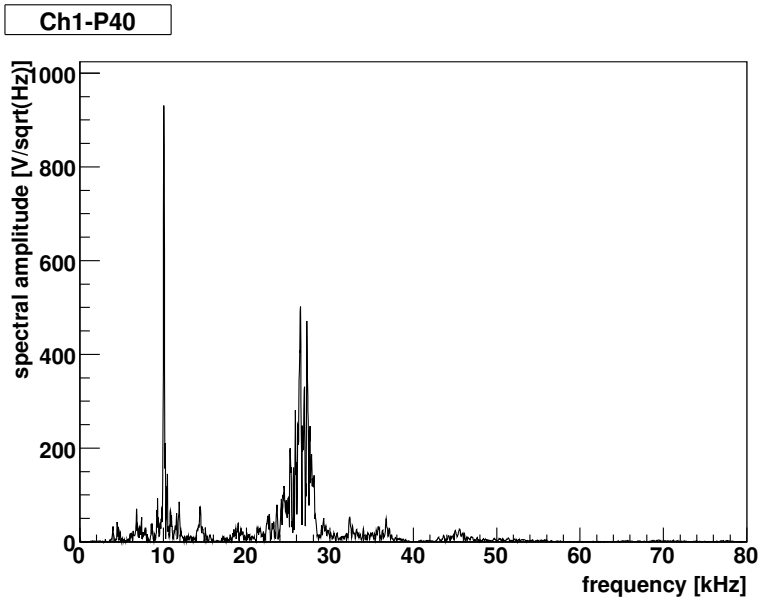


(b)

Figure 6.5: Signal and correposponding spectrum as recorded by one channel at 40 bar pressure.

per channel was 1.25 MHz/3 ≈ 417 kHz, more than enough to guarantee a good reconstruction of the bandwidth up to 200 kHz, larger than the bandwidth of our sensors. The same gated burst used to excite the transmitter was also used to trigger the data-taking with an acquisition time of 20-30 ms, sufficiently long for the signal to drop to the noise level. For each measurement, 100 events were recorded and averaged to improve the signal to noise ratio. The peak-to-peak voltage, $V_{pp,out}$, was computed as difference between the maximum and minimum value of the mean waveform; the statistical error $\sigma_{V_{pp,out}}$ was obtained by standard propagation of the error.

A first series of measurements called *voltage sweep* aimed to evaluate the variation of the dynamic range as a function of the pressure. First, the amplitude of the pulse exciting the transmitter, called $V_{pp,in}$, was changed from the minimum possible value up to the value at which the differential output of the preamplifier sensor was in saturation (above 3.5 V or below -3.5 V). Beyond this point the curve $V_{pp,out}$ vs. $V_{pp,in}$ flattens. Each of the three channels of the sensor has its own piezoelectric ceramic and preamplifier chains, so the saturation can happen at a different amplitude of the pulse exciting the transmitter; of course also the orientation of the sensor compared to the transmitter and the angular sensitivity of the sensor plays an important role.

Once the voltage sweep was completed at the pressure of 1 bar, the pressure was raised and the cycle was repeated. The increase of the pressure was done in variable steps, sometimes by 20 bar and sometimes by 40 bar. The final pressure reached was about 100 bar. A list of the pressure steps at which the measurement cycle was executed is shown in Table 6.1. The results of the experiment for two channels is shown in Figure 6.6.

| Aug. 2008: pressure | label |
|---|---|
| 1 bar | P0b2 |
| 20 bar | P20u |
| 40 bar | P40u |
| 60 bar | P60u |
| 80 bar | P80b |
| 100 bar | P100u |
| 100 bar | P100b |
| 60 bar | P60b |
| 40 bar | P40b |
| 1 bar | P0b |

| Feb. 09: pressure | label |
|---|---|
| 40 bar | P40 |
| 80 bar | P80 |
| 100 bar | P100 |
| 100 bar | P100b |
| 80 bar | P80b |
| 40 bar | P40b |
| 20 bar | P20b |
| 1 bar | P0b |
| 20 bar | P20u |
| 1 bar | P0b2 |

Table 6.1: Sequence of pressure values at which the voltage sweep was done during the campaign of measurements happened in August 2008 and February 2009. The column on the right indicates the label used in Figure 6.6 to mark the relative data.

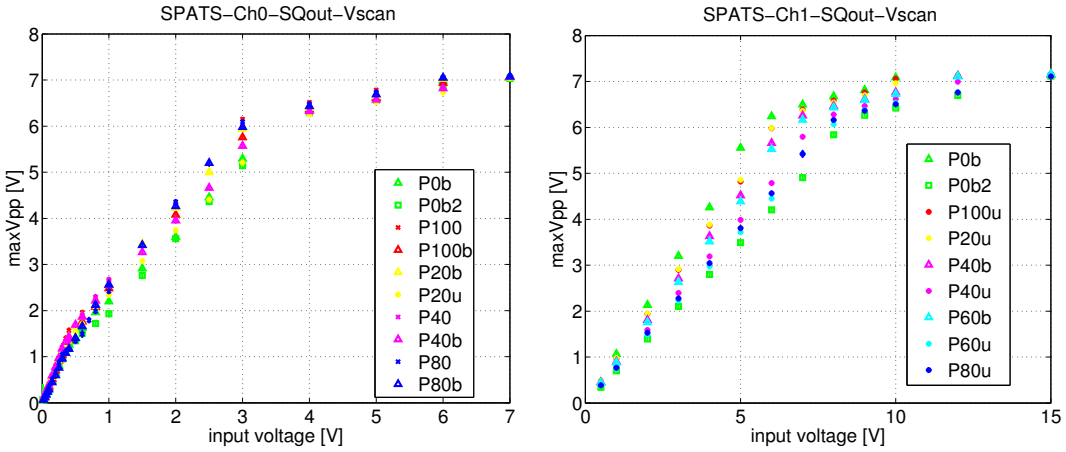


Figure 6.6: Peak-to-peak amplitude vs. input voltage as a function of the pressure for Channel 0 (box (a)) in the SPATS sensor tested in August 2008 and for Channel 1 (box (b)) of the other SPATS sensor tested during the campaign happened in February 2009.

During the second series of measurements, another set was done: data were taken at different pressures, keeping constant the transmitter pulse amplitude and position. After completing one or more cycles in pressure, the relative position of sensor and transmitter was changed. This was done in two ways: at the beginning relocating the transmitter in another place; then also rotating azimuthally the position of the sensor inside the vessel. An example plot of the peak-to-peak voltage as a function of the pressure is illustrated in Figure 6.7. No clear trend is observed.

Analogous data can be extracted from the *voltage-sweep* measurements, selecting all the data-points for a certain value of input voltage, provided that this is chosen within the linear range of the sensor.

In order to investigate a variation of the signal strength correlated with the increase of pressure, a linear regression on the peak-to-peak voltage vs. pressure is performed on the data collected for every channel during each measurement cycle:

$$V_{pp}(P) = a_P P + b_P \tag{6.1}$$

To estimate the systematic error, the distribution of the pulls is observed. The fit is first performed using the statistical error only. The distribution of these errors is shown in Figure 6.8(a); a mean value $\langle \sigma_{stat} \rangle \approx 0.05$ V can be assumed neglecting the tails which make the distribution asymmetric. The pulls are calculated from each measurement as:

$$pull_i = \frac{y_i - y_{fit_i}}{\sigma_{y,stat_i}} = \frac{V_{pp_i} - y_{fit_i}}{\sigma_{V_{pp_i}}} \tag{6.2}$$

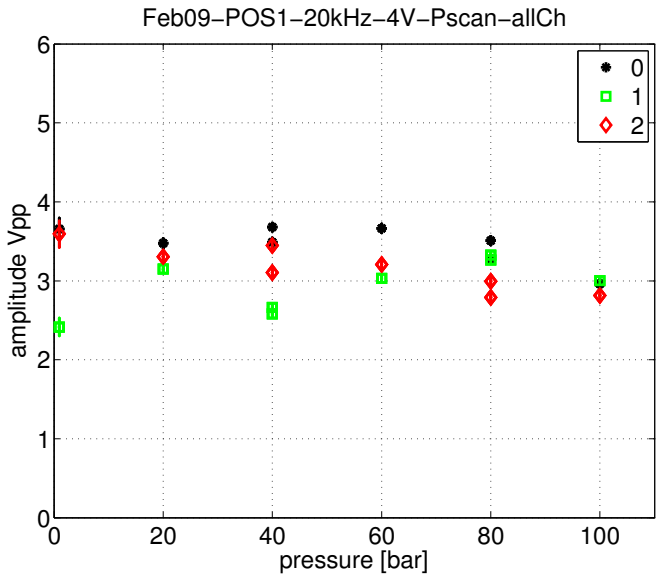


Figure 6.7: Voltage vs. pressure for the three channels of a SPATS sensor in one example measurement.

where $V_{pp_i}$ is the peak-to-peak voltage at a measurement, $y_{fit_i}$ is the value of the fitting function at the same pressure value and $\sigma_{y,stat_i} = \sigma_{V_{pp_i}}$ is the statistical error for the measured value.

The distribution of the pulls is shown in Figure 6.8(b). The sigma of the fitting Gaussian allows for an estimation of the mean total uncertainty as:

$$\sigma_{tot} \approx 5 \cdot \langle \sigma_{stat} \rangle \;=\; 5 \cdot 0.05 \;=\; 0.25 \text{ V} \tag{6.3}$$

$$\sigma_{sys} = \sqrt{\sigma_{tot}^2 - \langle \sigma_{stat} \rangle^2} \approx \; 0.25 \text{ V} \tag{6.4}$$

The calculated systematic uncertainty is included in the fit of the data from 1 to 100 bar. The gain in sensitivity from 1 bar to 50 bar is then calculated as following:

$$S|_{50\text{bar}} = S|_{1\text{bar}} \cdot (1 + x) \tag{6.5}$$

$$G_P = 1 + x = \frac{S|_{50 \text{ bar}}}{S|_{1 \text{ bar}}} \propto \frac{V_{pp}|_{50 \text{ bar}}}{V_{pp}|_{1 \text{ bar}}} = \frac{a_P \cdot P50 + b_P}{a_P \cdot P1 + b_P} \tag{6.6}$$

where $P50 = 50$ bar and $P1 = 1$ bar.

The distribution of these values, calculated measurement by measurement is shown in Figure 6.9.

The mean value and the standard deviation of the histogram are used to estimate the average gain in sensitivity for a pressure increase from 1 to 50 bar, which gives the result:

$$\langle G_P \rangle = 1.11 \pm 0.12 \tag{6.7}$$

consistent with no dependence of the sensitivity on the pressure.

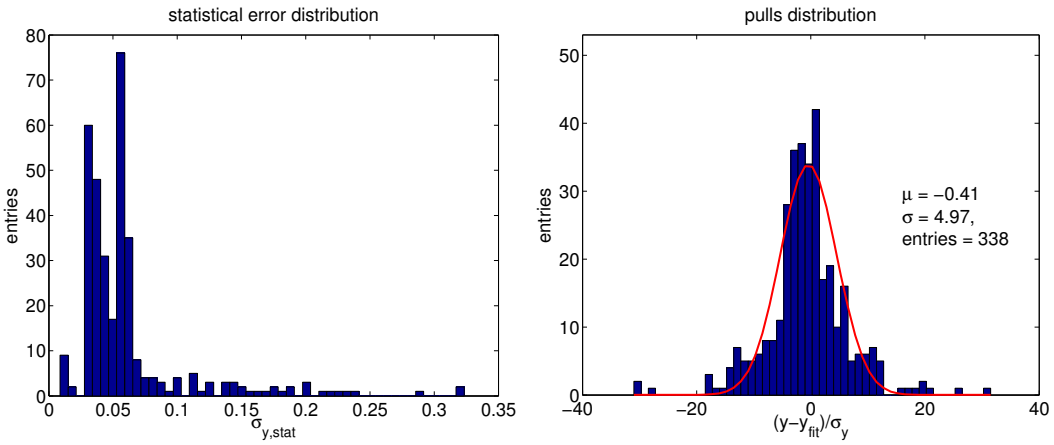


Figure 6.8: Pressure test error distribution. (a): Statistical error distribution for all the data. (b): Pulls distribution for all the measurements done, after fitting the data from each channel taking into account statistical errors only.

An attempt was made to measure the angular variation of the sensor moving the transmitter along the circumference of the vessel under 1 bar and 40 bar pressure. This was not successful, since the variation of the signal as a function of the position of the transmitter changes in a way which is not completely understood and is not reproducible. This was verified with the following simple test: the sensor inside the vessel was rotated by 240 degrees, and the transmitter was also moved so that it kept facing the same channel: in the two configurations, which were in principle analogous, the signal recorded was different. This led to the conclusion that it is not really possible to place the transmitter in two equivalent locations such that the transmission of the acoustic pulse inside the vessel is the same, perhaps due to the presence of the bolts along the whole circumference.

## 6.3 Temperature test

The SPATS sensors are deployed at the South Pole at a temperature which depends on the depth, and is about $-51\,^{\circ}\mathrm{C}$ at depths between 80 m and 500 m. All the equipment was tested before the deployment to verify the functionality at these temperatures. During these tests also the sensitivity change was investigated and resulted in an increase of the sensitivity of about a factor 1.4 from 0 to $-50\,^{\circ}\mathrm{C}$ (see [73]). The result of that measurement has been recently put under discussion, since it is not really clear whether the transmitter was located together with the sensor in the cold or not. A complementary test, hereafter described, has been done recently to verify with a different setup the validity of the quoted number.

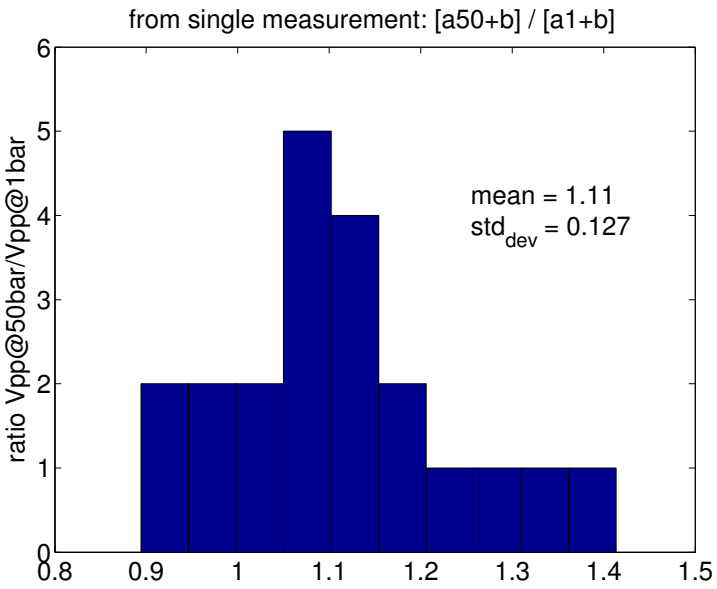


Figure 6.9: Distribution of the values of sensitivity gain obtained in the pressure test.

### 6.3.1 Description of the setup

The measurements were done using a freezer (produced by the company *Thermo Scientific*), available in the acoustic Laboratory of DESY, capable of going down to temperatures as low as $-86\,^{\circ}\mathrm{C}$. The freezer is connected to the power through a thermostat (*CAREL IR32*); the actual temperature is monitored by a thermocouple *PT-1000*. The signal from the thermocouple is used as feedback to the target temperature set on the thermostat, which turns on the freezer if the measured temperature is higher than the target one. The comparison with the values measured by different thermocouples and by a digital thermometer leads to the estimation of an error of $\pm\,2\,^{\circ}\mathrm{C}$. During the measurement the thermocouples were attached to a piece of metal equivalent to the one of which the SPATS housing is made, lying next to it, in order to avoid problems by contacting the virtual ground of the sensor (which is the housing itself, as explained in Chapter 4).

As transmitter the ITC-1001 (see Chapter 4) was used, pulsed with the same high-voltage pulse as used for the pinger. A repetition frequency of 5 Hz was obtained using as a trigger a square wave from a function generator. The strong emitted pulse permitted the emitter to be kept out of the freezer; the temperature of the pinger was that of the room, kept under control by an air-conditioning system set at $25\,^{\circ}\mathrm{C}$.

A SPATS sensor was located in air at the bottom of the freezer (at about 2.5 m distance from the emitter), so that one channel was facing up. Power was provided with a standard laboratory power supply. The three differential channels were read out by the same data acquisition card from *National Instruments* (*NiDAQ-*

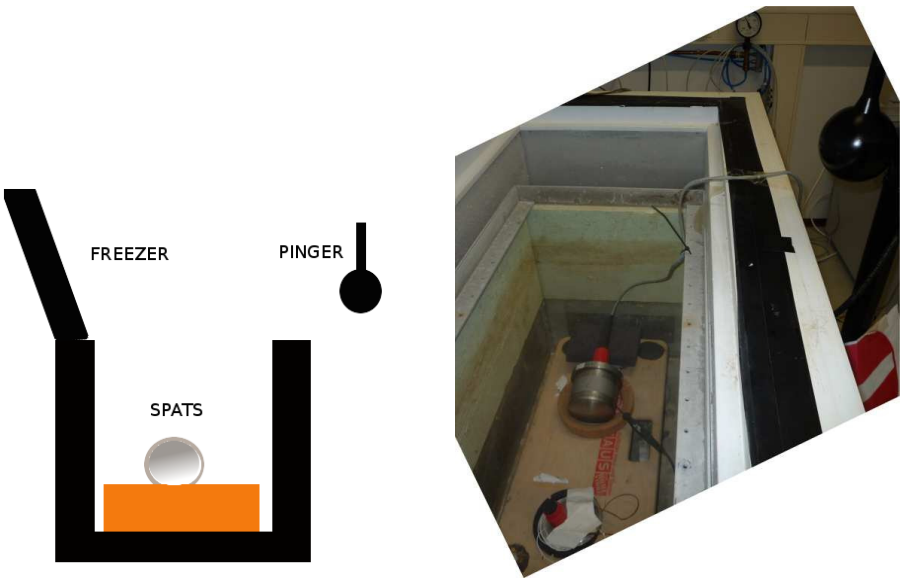


(a) (b)

Figure 6.10: Sketch and picture of the setup for the temperature test.

*PAD 6070E*) as used in the previously described pressure test; they were sampled simultaneously, so that the effective sampling frequency per channel was $f_s = 1.25\ \text{MHz}/3 \approx 417\ \text{kHz}$.

### 6.3.2 Data taking and measurements

The square pulse used to trigger the transmitter was used also to trigger the data recording, which lasted for 60 ms. In each configuration 100 triggered events were recorded for three consecutive times. The 100 waveforms were averaged to get a mean waveform. The peak-to-peak voltage was computed as difference between the maximum voltage and the minimum voltage; the error was calculated as square root of the quadratic sum of the errors on the two values.

The temperature of the freezer was changed in various steps, which are illustrated in Table 6.2. Two sets of measurements were done. In *Set 1* Channel 0 was facing up, in direction of the sound source; in *Set 2* Channel 2 was facing the emitter. During cooling, the freezer was kept closed and opened only to take each measurement. During the warming up, the freezer was partially opened to allow for a non-drastic change of the temperature; at the time of each measurement, the temperature was verified to be stable.

To estimate the systematic error the same technique as applied before was used: the data were fitted with the statistical error only. The distribution of the statistical errors is shown in Figure 6.11(a). The distribution of the pulls, defined as described in equation 6.2 with $i$ referring to a temperature measurement, was

| Set 1 (1) T[°C] | (2) T[°C] | Set 2 [°C] |
|---|---|---|
| -23 | ... | -40 |
| -30 | -20 | -56 |
| -35 | -10 | -55 |
| -40 | 0 | -49 |
| -45 | -10 | -31 |
| -49 | -21 | -20.8 |
| -60 | -30 | -12 |
| -49 | -40 | -7.4 |
| -40 | -50 | -3 |
| -30 | -60 | |
| ... | | |

Table 6.2: Sequence of temperatures values used for a measurement in the temperature test. The first two columns on the left indicate the measurement values for *Set 1* and the column on the right shows the values, in order, for the measurements of *Set 2*.

used to estimate the systematic error. This distribution is shown in Figure 6.11(b). The Gaussian fit of the histogram gives a total uncertainty of:

$$\sigma_{tot} \approx 2 \cdot \langle \sigma_{stat} \rangle \approx 2 \cdot 0.1 \ = \ 0.2 \text{ V} \tag{6.8}$$

therefore the systematic error can be quantified as:

$$\sigma_{sys} = \sqrt{\sigma_{tot}^2 - \langle \sigma_{stat} \rangle^2} \approx \ 0.1 \text{ V} \tag{6.9}$$

This systematic error was introduced as additional error in the analysis and the linear regression was performed. An example of the data-points and the fit obtained for Channel 0 in *Set 1* is shown in Figure 6.12.

A linear regression by least square minimization was performed for each channel, including all the data taken in the same set of measurements, in order to determine the coefficients $a_T$ and $b_T$ for each channel, defined as:

$$V_{pp}(T) = a_T T + b_T. \tag{6.10}$$

The sensitivity gain was computed from the peak-to-peak voltage at 0 °C and at −50 °C as:

$$S|_{-50°C} = S|_{0°C} \cdot (1 + x) \tag{6.11}$$

$$G_T = 1 + x = \frac{S|_{-50°\text{C}}}{S|_{0°\text{C}}} \propto \frac{V_{pp}|_{-50°\text{C}}}{V_{pp}|_{0°\text{C}}} = \frac{a_T \cdot (-50°\text{C}) + b_T}{b_T} \tag{6.12}$$

The distribution of the values of $G_T$ obtained is illustrated in Figure 6.13. The mean and the standard deviation of the values can be used to estimate the average gain of sensitivity as:

$$< G_T >= 1.45 \pm 0.15. \tag{6.13}$$

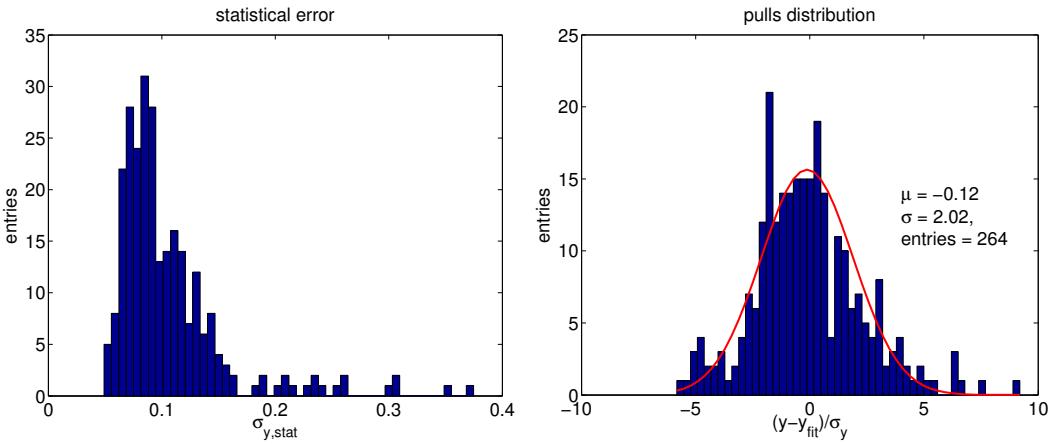


Figure 6.11: Temperature test error distribution. (a): Statistical error distribution for all the data. (b): Pulls distribution for all the measurements done, after fitting the data from each channel taking into account statistical errors only.

With the illustrated setup, one can be confident that the change in the signal can be attributed to temperature dependence of sensor sensitivity. A change in the transmittivity of the emitter can be excluded since the emitter is always at the same temperature. Some residual effect is correlated with the distribution of temperature within the volume of air between source and transmitter. This is difficult to monitor and control, but it is likely to be inhomogeneous and variable as soon as the freezer is open to do the measurement. The change in the air density can be calculated using the relation

$$\rho[\mathrm{kg/m^3}] = \frac{P}{R \cdot T} \tag{6.14}$$

where $P$ is the pressure in [Pa], $R = 287.05$ J/(kg · K) is the gas constant for dry air and $T$ is the temperature in [K]. The density of air increases at low temperature: the values at 0, $-50$ and $-60\,^{\circ}$C were calculated assuming a pressure of 1 atm (101325 Pa). On the other side a decrease of the air temperature from 0 to $-50\,^{\circ}$C causes a decrease of the speed of sound, due to the fact that the molecules move slower in air at low temperature. The acoustic impedance, which is the product of density and speed of sound, increases at lower temperatures (see the numbers in Table 6.3). If the acoustic impedance increases, the sound transmitted through the medium should decrease. This is in opposite direction to what was measured, therefore the measured variation should be not overestimated (but could still be underestimated).

The increase of sensitivity of a SPATS sensor at low temperature was explained in [73] in the following way: the expansion coefficient of a piezoelectric ceramic tablet in the direction of the polarization has a sign opposite to that of the expansion coefficient of the steel; this implies that while the steel shrinks at low temperature, the piezoelectric ceramic expands in the polarization direction, which is

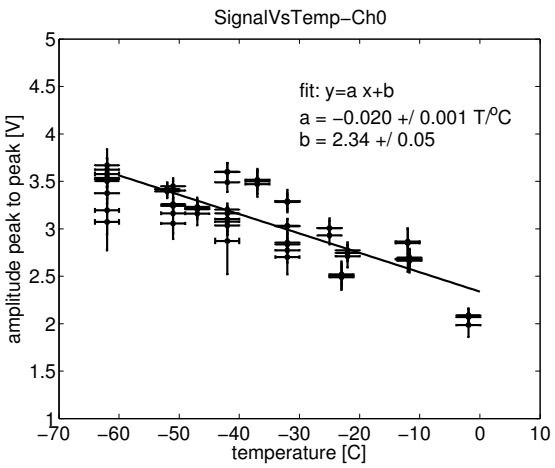


Figure 6.12: Peak-to-peak voltage recorded by one channel during one set of measurement (fixed position) as a function of the temperature.

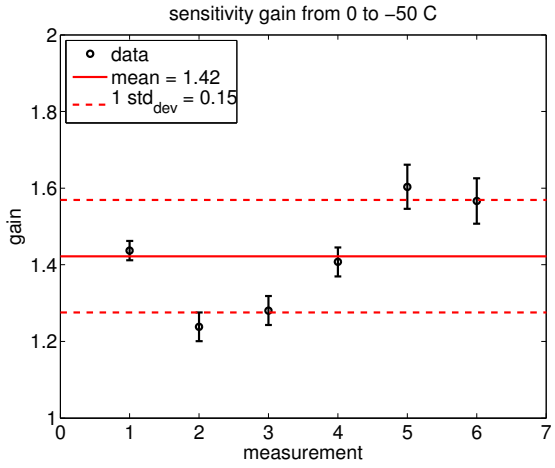


Figure 6.13: Distribution of the ratios calculated according to equation 6.12 for each channel and each set.

| temperature T[°C] | density $\rho$ [kg/m$^3$] | speed of sound $c_s$ [m/s] | acoustic impedance $Z$[kg/(s· m$^2$)] |
|---|---|---|---|
| 0 | 1.292 | 331.45 | 428.23 |
| -50 | 1.534 | 299.58 | 459.56 |
| -60 | 1.657 | 292.79 | 485.15 |

Table 6.3: Density of air, sound speed and acoustic impedance at different temperatures.

perpendicular to the contacts, increasing the static pressure hold by the piezoelectric ceramic itself. This effect has been confirmed at the South Pole, where an increase of the noise level was measured during the freeze-in process (when the temperature of the sensor decrease).

## 6.4 Conclusion

Two different tests were performed to evaluate the variation of the sensitivity at high pressure and at low temperature. A non-significant increase of the signal was found to be correlated with an increase of the pressure up to 50 bar, which is about the one exerted on the glaciophones when they are deployed in water at 500 m depth. Nothing is known about the pressure existing after freezing. The test seems to confirm that the steel housing of SPATS sensors is not deformed under high static pressure.

The test done to measure the temperature dependence confirmed that the

sensitivity increases by a factor of about 1.5 when the temperature drops from 0 to $-50\,^{\circ}\mathrm{C}$. This result was achieved excluding any influence due to temperature dependence of the emitter transmittivity.

To combine the information obtained regarding the sensitivity variation is complicated. The sensitivity could in principle be a function of two variables, $s = f(P, T)$. In the previous experiments we sampled the values of this function along two lines defined by $T = 25\,^{\circ}\mathrm{C}$ (in the pressure test) and $P = 1$ bar (in the temperature test) [76]. What we want to do is to estimate the value of the function at $T = -50\,^{\circ}\mathrm{C}$ and $P = 50$ bar.

To do this, it is reasonable to infer the following:

- The variation in sensitivity due to temperature decrease goes in the same direction as the one due to pressure increase. It is plausible that the combination of the variation of the two parameters would not invert this trend.
- In first approximation, it is possible to neglect $G_P$ in comparison with $G_T$, since the gain in pressure $G_P$ is compatible with no increase.

With the previous arguments we expect that the sensitivity increase from ($T = 0\,^{\circ}\mathrm{C}$, $P = 1$ bar) to ($T = -50\,^{\circ}\mathrm{C}$, $P = 50$ bar) is at least equal to the minimum value estimated for the increase due to temperature decrease:

$$G_{T,P} \geq 1.2 \tag{6.15}$$
$$S_{T=-50\,^{\circ}\mathrm{C},P=50\ \mathrm{bar}} > 1.2 \cdot S_{T=0\,^{\circ}\mathrm{C},P=1\ \mathrm{bar}} \left[\frac{\mathrm{V}}{\mathrm{Pa}}\right]$$

The SPATS sensors installed in strings A, B, C were calibrated in water at $0\,^{\circ}\mathrm{C}$ prior to deployment. The sensitivity in water $S_{water}$ was measured as a function of the frequency in the range between 10 and 80 kHz. An example is shown on page 121. The estimated $G_{T,P}$ can be used to scale $S_{water}$ and get the corresponding value in ice the sensitivity measured from water to ice:

$$S_{ice} > 1.2 \cdot S_{water} \tag{6.16}$$

At this point, the measured power spectral density of the noise in ice in terms of [$\mathrm{V}^2/\mathrm{Hz}$], can be divided by the frequency dependent $S_{water}$ applying the correction factor just found. Next, it can be integrated over the bandwidth [1-50 kHz] to get the corresponding noise value in [Pa]. For more details see [70].

Of course it must be taken into account that here we are assuming that the change in coupling from water to ice does not have major effects; also, the presence of the "hole ice" around the sensor is completely neglected. More experiments in the laboratory and *in situ* will be necessary to investigate the validity of the assumptions made and the effect of the ice-coupling on the sensitivity variation.

# Chapter 7

# Summary and outlook

This thesis was carried out within the feasibility study of acoustic neutrino detection at the South Pole.

A neutrino interacting in a medium produces a lepton and a cascade. Optical detection relies on the measurement of the Cherenkov light emitted by rapidly moving charged particles. A neutrino-induced particle cascade also produces radiation in the radio bandwidth. The radiation is coherent for wavelengths longer than the typical shower size, corresponding to frequencies between 0.1 GHz and 1 GHz: in this range, the signal strength depends on the square of the energy of the incoming neutrino. In addition to the optical and radio signal, an acoustic wave is generated in the interaction due to the thermo-acoustic effect: the heat released in the medium by the cascade creates a pancake-shaped acoustic pressure wave, which expands in the plane orthogonal to the shower axis, with a pressure amplitude linearly proportional to the energy of the incoming neutrino.

While the optical detection method is now well established, the radio and the acoustic methods are under study by several experiments in different media (ice, water, salt).

The use of multiple detection channels seems to be a requirement in order to detect unambiguously UHE neutrinos related to the GZK cut-off of cosmic rays, for at least two reasons. The flux is predicted to be extremely low (about one detected neutrino per $km^2$ per year), so that a sufficiently large volume (on the order of 100 $km^3$) needs to be instrumented to collect a few events per year. The construction of such a big detector is not feasible in terms of cost if only optical sensors are used, but could be built combining radio and acoustic sensors which are cheaper and could be installed in a sparser configuration. In addition, due to the low number of expected events, to detect the interaction through more than one channel would give more credibility to the discovery.

Ice seems to be the best medium possible, because the three signals could be measured simultaneously.

The research carried out here focuses on the evaluation of the acoustic properties of the ice at the South Pole and was motivated by a simulation done in 2005, which showed that the acoustic detection method could be interesting as comple-

mentary to the radio and the optical. A 100 km$^3$ detector combining optical, radio and acoustic sensors promised the detection of about 20 GZK neutrinos per year, 40% of which would be in the form of hybrid events detected by more than one detection channel. The simulation assumed an acoustic attenuation length of a few km, calculated theoretically in [47] and dominated by the frequency independent absorption length, and a threshold of 9 mPa.

The *South Pole Acoustic Test Setup* (SPATS), an array of acoustic sensors and transmitters at different depths, has been designed and installed at the South Pole with the goal to measure *in situ* the sound speed profile, transient rates and features, background noise level and attenuation length.

Significant progress has been achieved on all the set goals. The sound speed profile has been measured with a precision of 1%, the transient events are studied and characterized, and the noise has been shown to be constant, Gaussian and decreasing with depth.

The major focus of the work was the measurement of the attenuation length which is an essential parameter in order to determine the spacing between sensors in a future detector. A retrievable transmitter, named *pinger*, was developed to perform the measurement. The pinger was used in multiple water-filled IceCube holes during two austral summer seasons. A strong improvement of the pinger was achieved in the second season, allowing for a successful measurement. The attenuation coefficient $\alpha$ was determined from the variation of the energy of the waveform recorded by the same sensor-channel for different pinger distances, taking into account the geometrical attenuation factor. The analysis was carried out for all the available 49 channels independently; 48 measurements were possible. These values were averaged together and the width of their distribution was taken as error, taking into account the corresponding errors. Under these conditions, the attenuation length was measured to be $312^{+68}_{-47}$ m, about one order of magnitude lower than the predicted value. The result has been crosschecked with other measurements on different data sets, using the frozen-in transmitters or the transients events from a known location. No significant dependence on the frequency or the depth was found in the data collected.

A minor part of the thesis focused on the study of the sensitivity variation of the sensors deployed at the South Pole. This is important in order to understand the validity of the threshold level used in the simulated model. All the sensors were calibrated in water prior to the deployment. Different tests were later performed on similar sensors at high pressure and low temperature, in order to evaluate the signal strength change under each of these conditions which are combined at the South Pole. An increase of the sensitivity was found in both the tests: for a change in pressure from 1 to 50 bar, a value of $1.11 \pm 0.12$ was found. For a decrease in temperature from 0 to $-50\,^{\circ}$C, an increase in sensitivity equal to $1.45 \pm 0.15$ was measured. The estimation of the sensitivity variation due to the simultaneous combination of these two effects is a difficult task and requires laboratory studies. More work is undergoing to define the pressure equivalent noise level at the South

Pole.

The result of the acoustic attenuation measurement has two implications. From the theoretical point of view, it is necessary to understand the reason of disagreement with the previous theory. This work is at present in progress; other measurements are planned to investigate the frequency and depth dependence of the attenuation length with a multi-frequency pinger. Indeed, if a frequency dependence is found, it is likely that the attenuation is due to scattering, which depends on the frequency to the power of 4. In this case, the acoustic pancake produced by the neutrino interaction would change into a more spherical shape. This would make it theoretically possible to recover part of the energy scattered and would result in a possible larger vertical spacing between sensors in a future detector.

The disagreement of the measured value with the one used for the previous calculations implies that different geometries need to be simulated in order to establish the feasibility of acoustic neutrino detection at the South Pole. Indeed, if the attenuation is scattering-dominated rather than absorption-dominated, the vertical spacing could be made larger, while the horizontal spacing should be shortened due to the measured attenuation length. The change in shape of the acoustic pattern and the different detector configuration need to be simulated to estimate energy threshold and performance.

A 100 $km^3$ hybrid radio-acoustic volume detector as proposed a few years ago can hardly be realized with the acoustic attenuation length measured. However, the possibility to couple acoustic sensors in addition to antennas in a large scale radio detector should still be investigated, since in any case the detection of a signal in the acoustic channel would enrich the information obtainable by an event in the case it was happening near the sensor.

Currently the construction of a 100 $km^3$ radio detector around or aside IceCube has been proposed. The radio background is large, therefore the presence of the optical detector would give in principle the advantage to have some overlap between events detected both by the radio method and by the optical method. This could happen only for events in the effective volume of the radio detector, with a muon going through the optical detector volume. The optical signal which could be used would therefore be the Cherenkov light from the muon track. This kind of signal appears however only in case of charged interaction of a muon neutrino and not in all the other cases (such as charged interaction of all the other neutrino flavors and neutral current from muon neutrino), therefore the expected overlap between radio and optical would be marginal [82]. If instead some acoustic neutrino detectors were added to the radio detectors, it would be possible to recognize the cascade event measuring two different signals from the cascade itself. The acoustic array would not be a self-standing detector but could be used as triggered by a radio signal, permitting the identification of GZK neutrino events. This would enlarge the credibility of the discovery, and would allow for the rejection of fake events.

# Appendix A

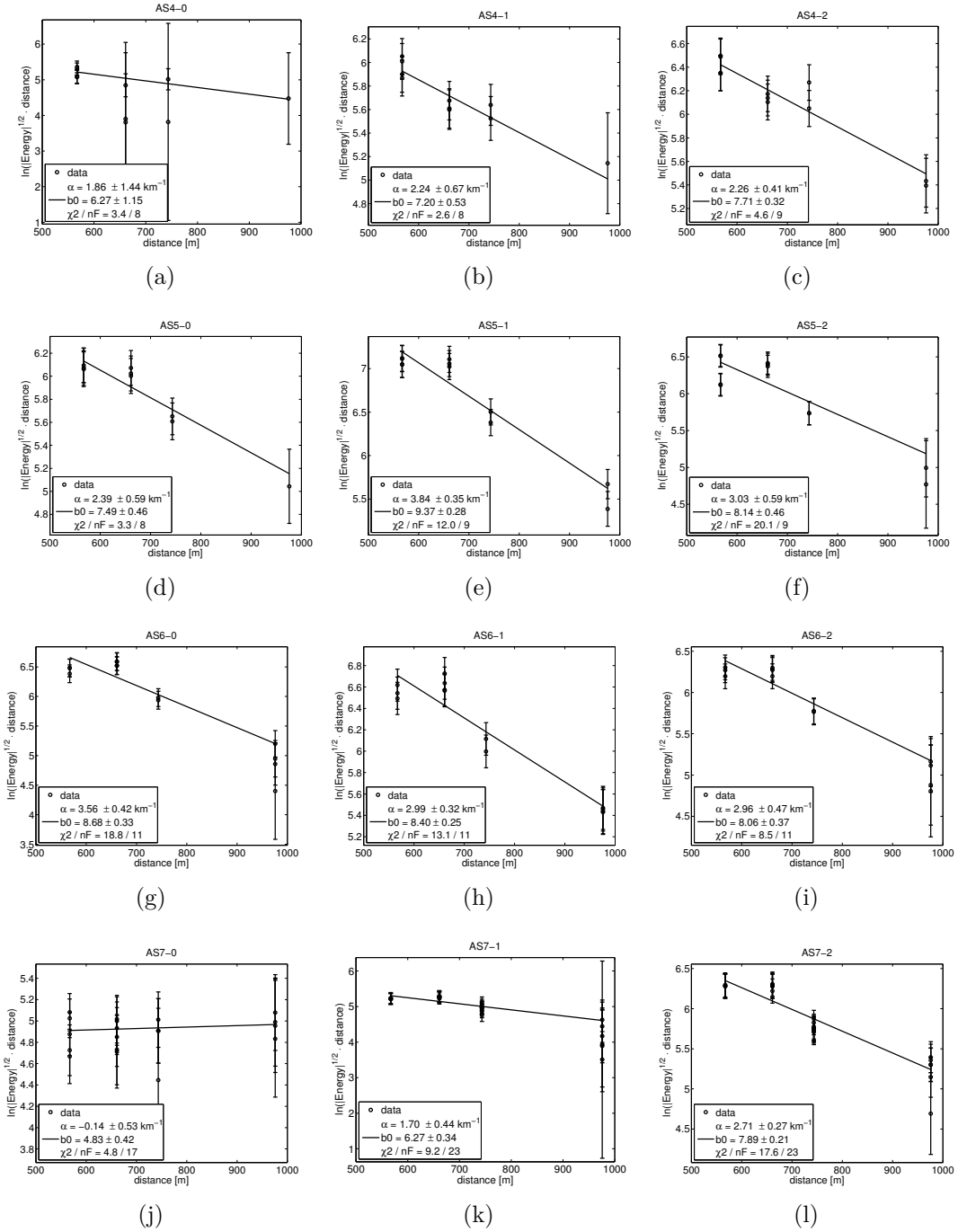


Figure 7.1: Attenuation coefficient fit for each channel of String A.

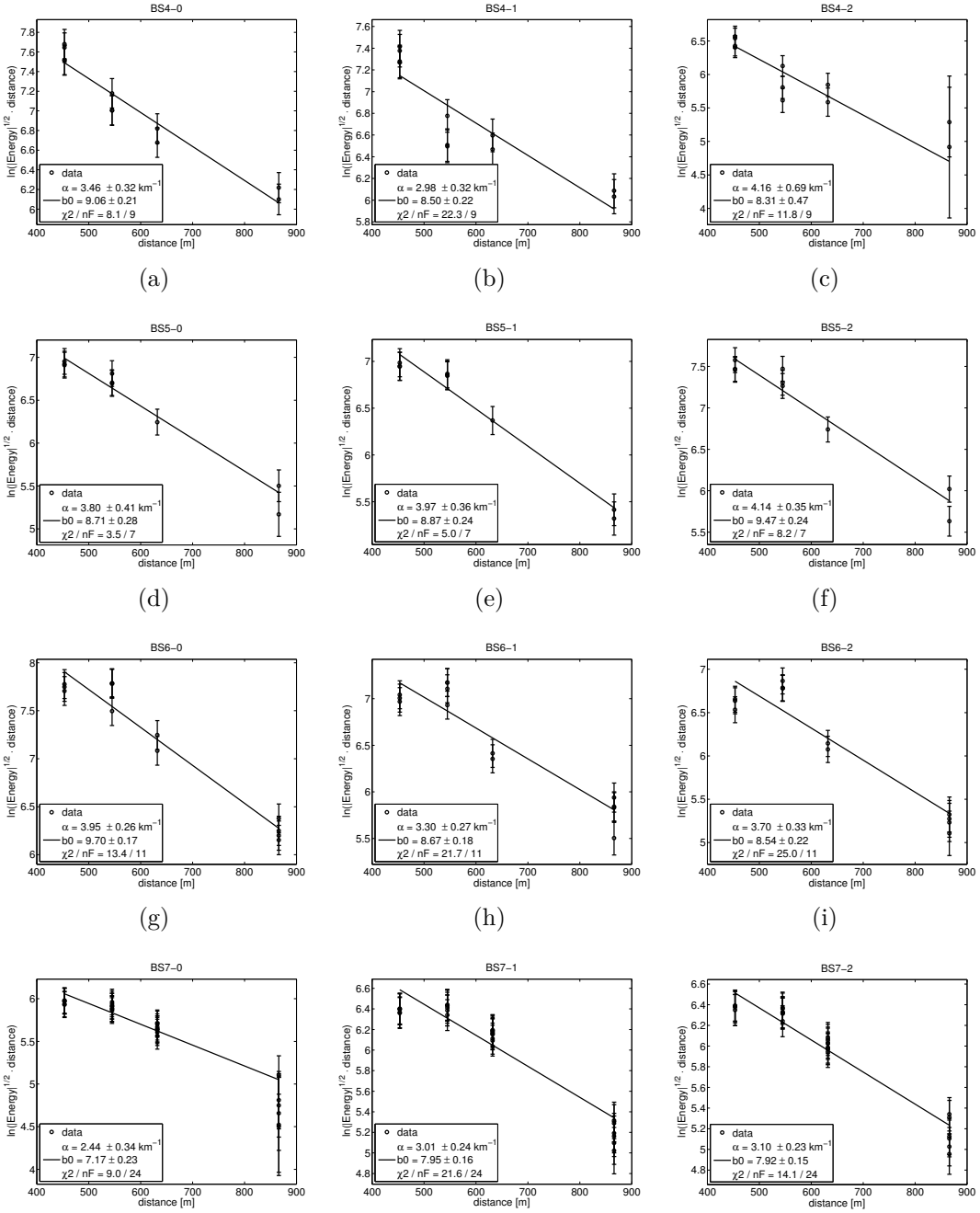


Figure 7.2: Attenuation coefficient fit for each channel of String B.

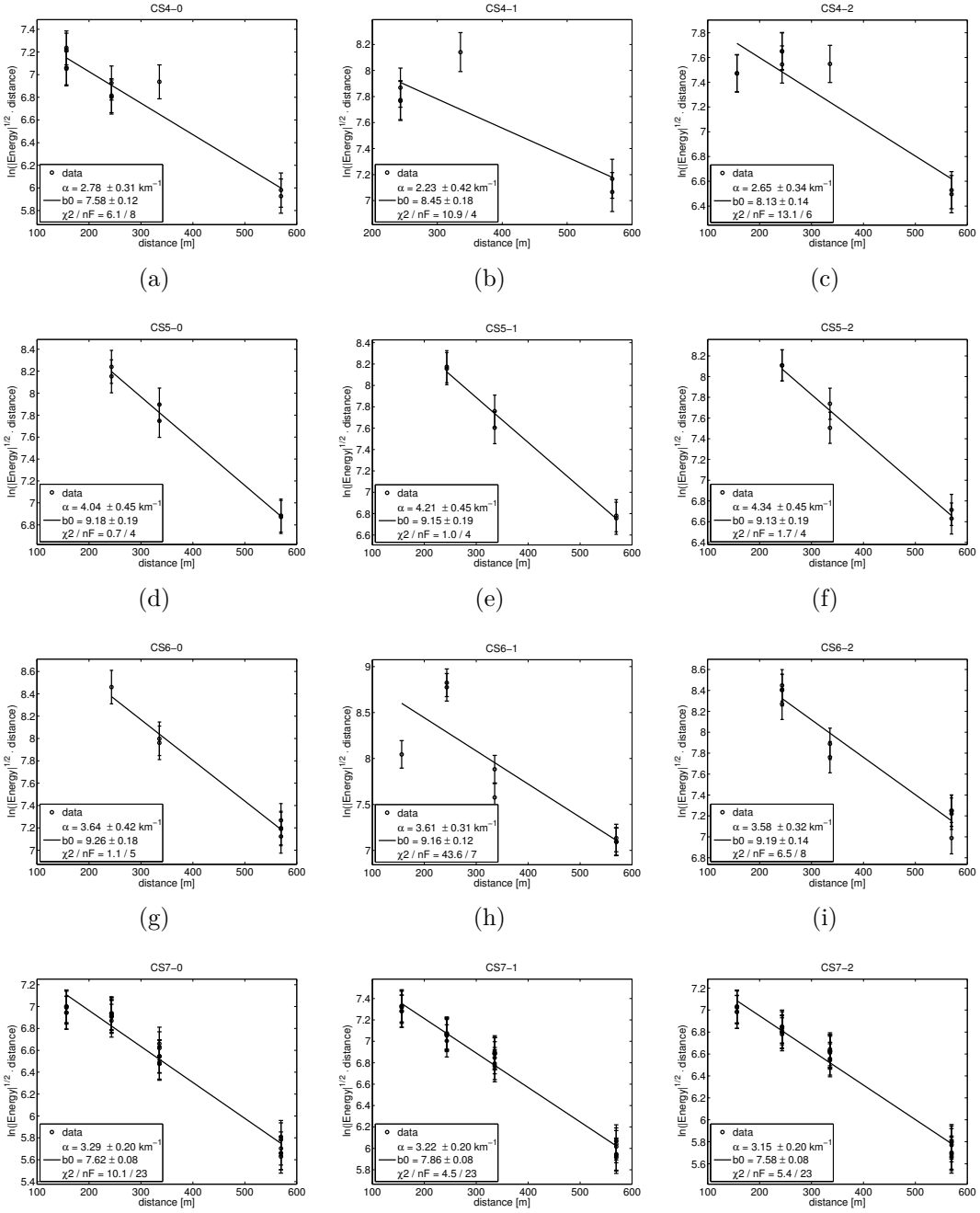


Figure 7.3: Attenuation coefficient fit for each channel of String C.

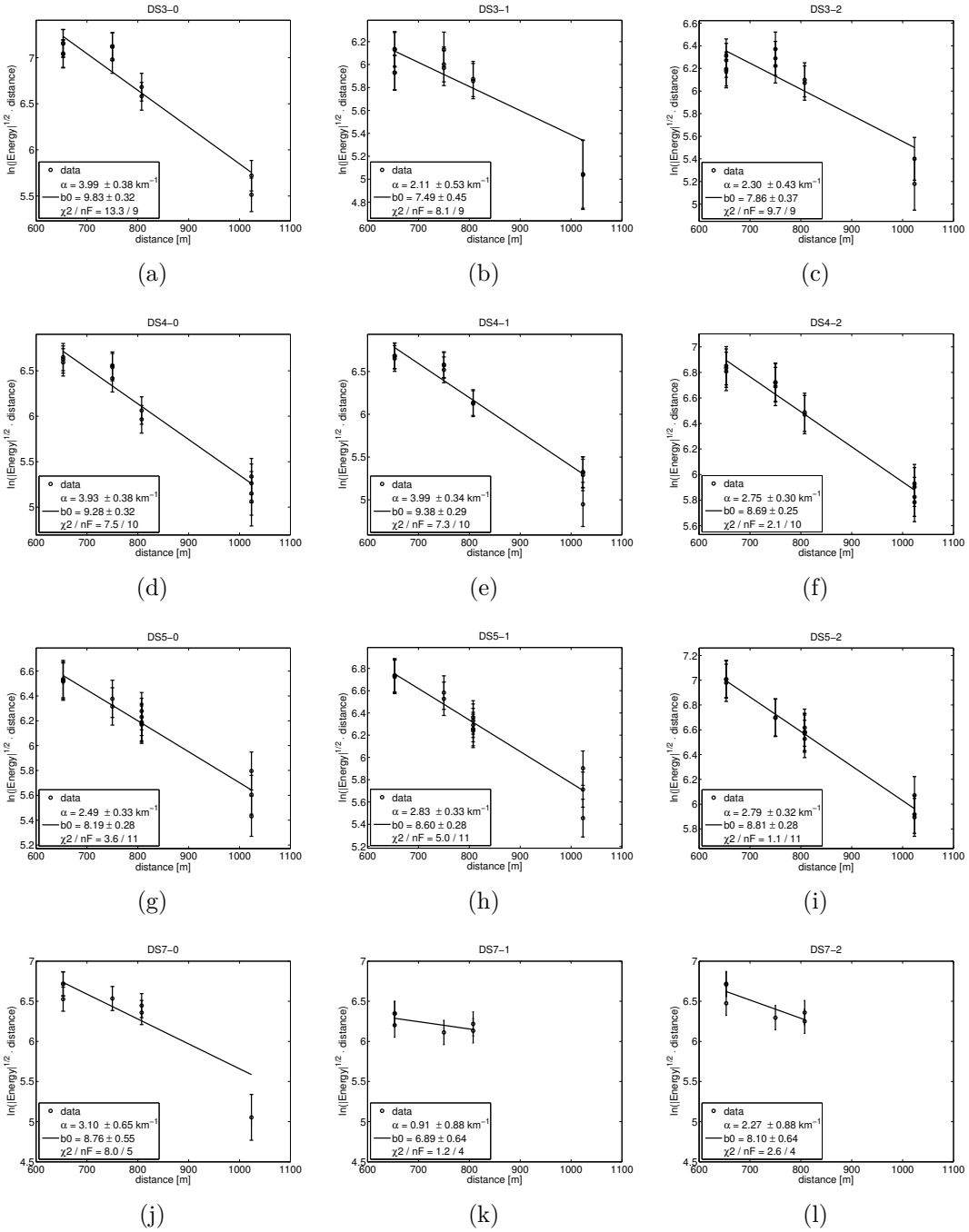


Figure 7.4: Attenuation coefficient fit for each channel of String D.

# Bibliography


[1] P. Bhattacharjee and G. Sigl. Origin and propagation of extremely high energy cosmic rays. *Phys. Rep.*, 327, 2000.

[2] The Pierre Auger Collaboration. Astrophysical sources of cosmic rays and related measurements with the Pierre Auger Observatory. In *Proceedings of the 31st International Cosmic Ray Conference*, 2009.

[3] G. T. Zatsepin and V. A. Kuz'min. Upper limit of the spectrum of cosmic rays. *Sov. JETP Lett.*, 4, 1966.

[4] A. Ringwald. Extremely energetic cosmic neutrinos: opportunities for astrophysics, particle physics and cosmology. *Int. J. Mod. Phys.*, A21S1, 2006.

[5] R. Gandhi, C.Quigg, M. Hall Reno, and I. Sarcevic. Ultra-high energy neutrino interactions. *Astropart. Phys.*, 5, 1996.

[6] J. Ahrens et al. Sensitivity of the IceCube detector to astrophysical sources of high energy muon neutrinos. *Astropart. Phys.*, 20, 2004.

[7] G.A. Askariyan. Excess negative charge of an electron-photon shower and its coherent radio emission. *Sov. JETP*, 14, 1962.

[8] G.A. Askariyan, B. A. Dolgoshein, A.N. Kalinovsky, and N.V. Mokhov. Acoustic detection of high energy particle showers in water. *Nucl. Instrum. Methods*, 164, 1979.

[9] RICE Collaboration. Status of Radio Ice Cherenkov Experiment (RICE), 1997. arXiv:astro-ph/9709223.

[10] I. Kravchenko et al. RICE limits on the diffuse ultra-high energy neutrino flux. *Phys. Rev.*, D73, 2006.

[11] P. W. Gorham et al. New limits on the ultrahigh energy cosmic neutrino flux from the ANITA experiment. *Phys. Rev. Lett*, 103, 2009.

[12] D. Besson, S. Böser, R. Nahnhauer, P.B. Price, and J. A. Vandenbroucke. Simulation of a Hybrid Optical/Radio/Acoustic extension to IceCube for EeV neutrino detection. In *Proc. 29th ICRC*, 2005.

[13] Abbasi et al. Measurement of sound speed in South Pole ice. *Astropart. Phys.*, 2009.

[14] R. Nahnhauer, A. A. Rostovtsev, and D. Tosi. Permafrost - an alternative target material for ultra high energy neutrino detection? *Nucl. Instrum. Meth.*, A587, 2008.

[15] K. G. Jansky. Radio waves from outside the solar system. *Nature*, 132, 1933.

[16] G. Reber and E. H. Conklin. UHF receivers. *Radio*, 225, 1938.

[17] R. Giacconi, H. Gursky, F.R. Paolini, and B.B. Rossi. Evidence for X-rays from sources outside the solar system. *Phys. Rev. Lett.*, 9, 1962.

[18] A.A Moiseev. Gamma-ray Large Area Space Telescope: mission overview. *Nucl. Instrum. Meth.*, A588, 2008.

[19] J. Buckley et al. The status and future of ground-based TeV gamma-ray astronomy, 2008. arxiv.org/abs/0810.0444.

[20] R. C. Henry. Diffuse background radiation. *Astrophys. J. Lett.*, 516, 1999.

[21] S. Yoshida and H. Dai. The extremely high energy cosmic rays. *J. Phys. G: Nucl. Part. Phys.*, 24, 1998.

[22] Nobel lectures, physics 1922-1941, 1965.

[23] A. M. Hillas. Cosmic rays: Recent progress and some current questions. *arXiv:astro-ph/0607109v2*, 2006.

[24] M. Kachelrieß et al. The galactic magnetic field as spectrograph for ultra-high energy cosmic rays. *Astropart.Phys.*, 26, 2006. arXiv:0510.444.

[25] J. Linsley. Evidence for a primary cosmic-ray particle with energy $10^{20}$ eV. *Phys. Rev. Lett.*, 10, 1963.

[26] C.C.H. Jui for the HiRes Collaboration. Results from the HiRes experiment. *J. Phys. Conf.*, 47, 2006.

[27] M. Takeda et al. Energy determination in the Akeno Giant Air Shower Array experiment. *Astropart. Phys.*, 19, 2003.

[28] A. Letessier-Selvon for The Pierre Auger Collaboration. Correlation of the highest energy cosmic rays with nearby extragalactic objects. *Science*, 318, 2007. arXiv:astro-ph/0711.2256.

[29] R. M. Bionta et al. Observation of a neutrino burst in coincidence with supernova 1987A in the Large Magellanic Cloud. *Phys. Rev. Lett.*, 58, 1987.

[30] V.S. Berezinsky and G.T. Zatsepin. Cosmic neutrinos of superhigh energies. *Phys. Lett.*, B28, 1969.

[31] C. Amsler et al. (Particle Data Group). The Review of Particle Physics. *Physics Letters*, B667, 2008.

[32] R. Engel, D. Seckel, and T. Stanev. Neutrinos from propagation of ultra-high-energy protons. *Phys. Rev.*, D64, 2001.

[33] V. Berezinsky. UHE neutrino astronomy and neutrino oscillations. In *Proc. 4th Int. Workshop "Neutrino Oscillations in Venice"*, 2008.

[34] R. Seckel and T. Stanev. GZK fluxes. `ftp://ftp.bartol.udel.edu/seckel/ess-gzk/2008/gzk_fluxes.pdf`, 2008.

[35] N. G. Lehtinen, P. W. Gorham, A. R. Jacobson, and R. A. Roussel-Dupré. FORTE satellite constraints on ultrahigh energy cosmic particle fluxes. *Phys. Rev.*, D69, 2004.

[36] E. Waxman and J. N. Bahcall. High energy neutrinos from astrophysical sources: An upper bound. *Phys. Rev.*, D59, 1999.

[37] K. Mannheim, R. J. Protheroe, and J. P. Rachen. Cosmic ray bound for models of extragalactic neutrino production. *Phys. Rev.*, D63, 2001.

[38] G. Sigl, S. Lee, P. Bhattacharjee, and S. Yoshida. Probing grand unified theories with cosmic-ray, gamma-ray, and neutrino astrophysics. *Phys. Rev.*, D59, 1999.

[39] T. Weiler. Resonant absorption of cosmic-ray neutrinos by the relic-neutrino background. *Phys. Rev. Lett.*, 49, 1982.

[40] R. Gandhi, C.Quigg, M. Hall Reno, and I. Sarcevic. Neutrino interactions at ultrahigh energies. *Phys. Rev.*, D58, 1998.

[41] A. Ringwald. Extremely energetic cosmic neutrinos and their impact on particle physics and cosmology. *Nucl. Phys.*, B136, 2004.

[42] S.L. Glashow. Resonant scattering of anti-neutrinos. *Phys. Rev.*, 118, 1960.

[43] Ackermann et al. Optical properties of deep glacial ice at the South Pole. *J. Geophys. Res.*, III, 2006.

[44] S. Barwick, D. Besson, P. Gorham, and D. Saltzberg. South Polar in situ radio frequency ice attenuation. *J. Glaciol.*, 51, 2004.

[45] L. Sulak et al. Experimental studies of the acoustic signature of proton beams traversing fluid media. *Nucl. Instrum. Methods*, 161, 1979.

[46] Lee F. Thompson. ARENA 2008 acoustic detection conference summary. In *Proc. 3rd ARENA*, 2008.

[47] P. B. Price. Attenuation of acoustic waves in glacial ice and salt domes. *J. Geophys. Res.*, 111, 2006.

[48] L. Fülöp T. and Biró. Cherenkov radiation spectrum. *Int. J. Theor. Phys.*, 31, 1992.

[49] M. Ackermann for The IceCube Collaboration. Search for Ultra High-Energy Neutrinos with AMANDA-II. *Astrophys. J.*, 675, 2007.

[50] The IceCube Collaboration. The first search for extremely-high energy cosmogenic neutrinos with the IceCube Neutrino Observatory. unpublished, 2009.

[51] T. Stanev F. Halzen, E. Zas. Radiodetection of cosmic neutrinos. a numerical, real time analysis. *Phys. Lett.*, B257, 1991.

[52] J. A. Muñiz, C. W. James, J. Protheroe R, and E. Zas. Cherenkov radio emission from showers in dense media at EeV energies. In *Proc. 30th ICRC*, 2007.

[53] D. Besson et al. In situ radioglaciological measurements near Taylor Dome, Antarctica and implications for ultra-high energy (UHE) neutrino astronomy. *Astropart. Phys.*, 29, 2008.

[54] A. Connolly. The radio Cherenkov technique for ultra-high energy neutrino detection. *Nucl. Instrum. Meth.*, A595, 2008.

[55] L. G. Dedenko et al. Prospects for deep sea acoustic detection of neutrinos. *Bull. Russ. Acad. Sci. Phys.*, 61, 1997.

[56] U. Grassano F. Bassani. *Fisica dello stato solido*. Bollati Boringhieri, 2000.

[57] J. Vandenbroucke. Summary: Acoustic detection of EHE neutrinos. *J. Phys.: Conf. Ser.*, 60, 2007.

[58] P. B. Price. Mechanism of attenuation of acoustic waves in antarctic ice. *Nucl. Instrum. Meth.*, A325, 1993.

[59] G. Riccobene et al. Long-term measurements of acoustic background noise in very deep sea. In *Proc. 3rd ARENA*, 2008.

[60] R. Lahmann. Status and first results of the acoustic detection test system AMADEUS. In *Proc. 3rd ARENA*, 2008.

[61] S. Bevan. *An Investigation into the Feasibility of Sea Water or Ice Based Acoustic UHE Neutrino Telescopes*. PhD thesis, University College London, 2008.

[62] N. Kurahashi. Updates from the Study of Acoustic Ultra-high energy Neutrino Detection phase II. In *Proc. 3rd ARENA*, 2008.

[63] Achterberg et al. First year performance of the IceCube neutrino telescope. *Astropart. Phys.*, 26, 2006.

[64] D. Besson, R. Nahnhauer, P. B. Price, D. Tosi, J. A. Vandenbroucke, and B.Voigt. Simulation of a hybrid optical-radio-acoustic neutrino detector at the South Pole. In *Proc. 3rd ARENA*, 2008.

[65] Böeser S. *Acoustic detection of ultra-high energy cascades in ice.* PhD thesis, Humboldt Universität Berlin, Mathematisch-Naturwissenschaftlichen Fakultät I, 2006.

[66] L. E. Kinsler, A. R. Frey, A. B. Coppen, and J. V. Sanders. *Fundamentals of acoustics.* John Wiley and sons, fourth edition edition, 2000.

[67] M. J. Crocker. *Handbook of acoustics.* John Wiley and sons, 1998.

[68] B. Semburg for the IceCube Collaboration. HADES: Hydrophone for Acoustic Detection at the South Pole. In *Proc. 3rd ARENA*, 2008.

[69] J. A. Vandenbroucke. *Acoustic detection of astrophysical neutrinos in South Pole ice.* PhD thesis, University of California, Berkeley, Department of Physics, 2009.

[70] T. Karg for the IceCube Collaboration. Acoustic noise in deep ice and environmental conditions at the South Pole. In *Proc. 3rd ARENA*, 2008.

[71] .. et al. Measurement of acoustic attenuation in South Pole Ice. *Astropart. Phys.*, 2009.

[72] J. A. Vandenbroucke for the IceCube Collaboration. Measurement of acoustic properties of South Pole ice for neutrino astronomy. In *Proc. 3rd ARENA*, 2008.

[73] J. H. Fischer. Acoustic transducers for the South Pole Acoustic Test Setup. Master's thesis, Humboldt Universität zu Berlin, Institut für Physik, 2006.

[74] Aki and Richards. *Quantitative seismology.* University Science Books, 2nd edition, 2002.

[75] W. T. Vetterling W. H. Press, S. A. Teukolsky. *Numerical recipes: the art of scientific computing.* Cambridge University Press, 3rd edition, 2007.

[76] J. A. Vandenbroucke. private communication, 2009.

[77] T. Karg. private communication, 2009.

[78] F. Descamps. *Feasibility of acoustic neutrino detection in ice with the South Pole Acoustic Test Setup.* PhD thesis, Universiteit Ghent, Belgium, 2009.

[79] E. Saltzman, M. Aydin, M. Williams, and C. Tatum. Antarctic ice cores, methyl chloride and methyl bromide. boulder, colorado usa: National snow and ice data center. digital media, 2007. URL `http://nsidc.org/data/nsidc-0313.html`.

[80] P. B. Price, J. A. Vandenbroucke, and D. A. Meese. Mechanisms for attenuation of 10-30 kHz acoustic waves at -51°C in glacial ice near South Pole. *submitted to Geophys. Res. Lett.*, 2009.

[81] M. Bothe. Influence of hole-ice properties on measurements of the South Pole Acoustic Test Setup. Master's thesis, Technische Universität Berlin, 2008.

[82] J. Berdermann, M. Carson, and R. Nahnhauer. Possible acoustic additions to a radio UHE neutrino detector. unpublished, July 2009.

# Danksagung

Usually one writes the acknowledgment at the end... Well, it took me over one year to write this part, but now I can finally have a sigh of relief and say that it is the last.

I would like to gratefully acknowledge Rolf Nahnhauer for accepting me as a student, and for following so closely my research, my progress and my bugs-finding. I thank also Hermann Kolanoski, for his role as my supervisor, and for the attention and help he gave me especially in the last months, and Christian Spiering, for reading my thesis and for supporting me in all my time in DESY. I am really thankful to Allan Hallgren, for hosting the Uppsala tests, and for being the most tireless worker I have ever seen at the South Pole. He has been an excellent mentor, in many questions of my life, and I hope he will keep this role in the future. Of course, a very hearty thank you to Buford Price, for hosting me in his group for several weeks in Berkeley: to change environment and point of view is a precious opportunity which does not happen to everyone. And of course thanks for giving me the chance to continue my research in Berkeley. A special thank you to Kalle Sulanke: there would have not been such a long part of hardware in my thesis if I had not had the pleasure to work with him, the person who taught me all the electronics which I studied in the books at the university. Without him the long weekdays and weekends spent in DESY to prepare the instrumentation would have been useless. I feel very privileged for having met the people I named: all of them have in common the enthusiasm in what they do, even after a long time. And I think this is the best example that beginners like me can ask for, and I will keep it as a reference for the future.

Then, I need to thank really a lot of people, those who filled these three years with so many unforgettable memories. Perry Sandstrom shared with me and the SPATS crew some of the most thrilling hours of the project, and was the outstanding surgeon who saved one of the "babies" at the South Pole. I feel in debt to him for helping me go to the Pole to work on IceCube construction again this year. I owe the whole Ph. D. to Elisa Bernardini, since she was through Google my first contact to the world of physics, and became later my adopted older sister. I hope I will achieve at least a little of what she has done.
From DESY, I am in debt to Reiner Heller for providing the mechanical draw-

ings which appear in my thesis, to Manfred Biastoch and Ralf Partsch for fixing tirelessly all my computer problems, and Jürgen Pieper for the help regarding electronic issues.

In the astro-particle group, I cannot forget guru-Sebastian, Bernhard, Markus and Stefan, the first-generation DESY friends, for helping me so much when I moved here and for keeping in touch even after leaving. And then John, Sean, Henrik, Evan, Florian, fellows of many dinners and drinks all over the world in several occasions. I hope we will visit each other whenever we have the chance. These are certainly the people which I have in highest esteem for the way they manage to be smart and fun, proving wrong the (at least common in Italy) prejudices against physicists. Of course I need to extend the deepest thank you to all the second-generation DESY guys, my personal software-physics support team: Fabian, Robert F., Robert L., Tilo, Pratik, Pepe, Lotfi, Eike, who always had the time to answer my urgent questions. To them I need to add Gareth and Michael, who got to be my human English dictionary in the thesis-writing time.

From the IceCube collaboration, I want also to thank the Berkeley guys: Ignacio, Kurt, Kirill, Michelangelo, and Ryan. I have special memories for each of them from my stay in Berkeley, and for each of the collaboration dinners where we were the most-fun and sometimes noisiest table. We should add many more memories of equal quality in the next year. Then, the IceCube women: Elisa R., Anna M., Rebecca, Konstancja, Oxana, Heike, Sirin, Maria: in some cases they have been forced to share my dramas, and they have been all great in making things look easier when they were not that easy. I owe a thank you to Carlos for the very practical help in the pressure test, but especially for one of the most comic sketch I have seen, with a physicist turning a screw in the wrong direction regardless of the right-hand rule, and a priceless "do not talk to me about physics". Then certainly I want to thank Timo and Giorgio, for the fruitful discussion about data analysis and physics, and Michele and Marco for being there whenever I was in need.

Last but not least: there are not enough words to say how grateful I am to some special people. Each of them has shown to me that life can be challenging in any field but we can always find the resources to smile and play the game. These people are my parents, because even if I know they would like a different life for me, I am sure they will never deny their support, whatever I choose for myself and wherever I go. And I must especially thank my mother, who gave proof that at any age one can be strong enough to make tough decisions. Then, my sister Silvia and my niece, since they have been part of my everyday life through Skype, the blessing of the last decade, and they have made me laugh from 9000 km distance. And the rest of my family, for which I am still the beloved crazy one. And finally Justin, since he has been the best co-worker, friend and travel-mate I could have asked for. After having been together on four continents, I have learned that good

things become better, and bad things become less bad, when you can share them with someone.

# Selbständigkeitserklärung

Hiermit erkäre ich dass ich die vorgelegte Doktorarbeit eigenständig, ohne unerlaubte fremde Hilfe und unter der Zuhilfenahme der angegebenen Quelle verfasst habe.